Strojniški vestnik

Journal of Mechanical Engineering

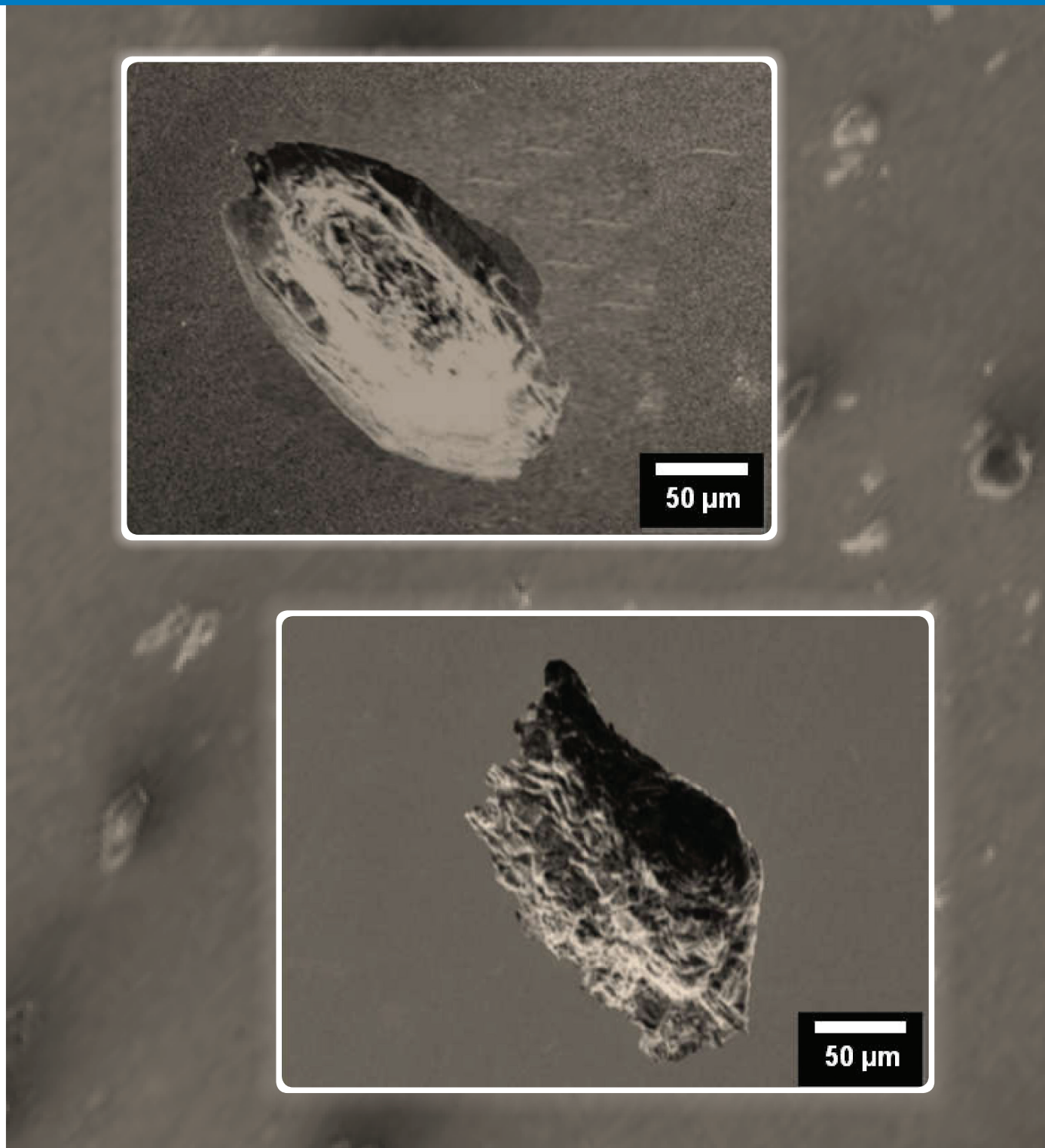

VOL 71 ▪ NO 1-2 ▪ Y 2025

Strojniški vestnik – Journal of Mechanical Engineering (SV-JME)

Aim and Scope
The international journal publishes original and (mini)review articles covering the concepts of materials science, mechanics, kinematics, thermodynamics, energy and environment, mechatronics and robotics, fluid mechanics, tribology, cybernetics, industrial engineering and structural analysis.
The journal follows new trends and progress proven practice in the mechanical engineering and also in the closely related sciences as are electrical, civil and process engineering, medicine, microbiology, ecology, agriculture, transport systems, aviation, and others, thus creating a unique forum for interdisciplinary or multidisciplinary dialogue.
The international conferences selected papers are welcome for publishing as a special issue of SV-JME with invited co-editor(s).

Editorial Office
University of Ljubljana, Faculty of Mechanical Engineering
SV-JME, Aškerčeva 6, 1000 Ljubljana, Slovenia
Phone: +386 (0)1 4771 137
info@sv-jme.eu, http://www.sv-jme.eu

Technical Editor: Pika Škraba

Print: Grafika Gracer d.o.o. printed in 190 copies

President of Publishing Council
Mihael Sekavčnik
University of Ljubljana, Faculty of Mechanical Engineering, Slovenia

Vice-President of Publishing Council
Matej Vesenjak
University of Maribor, Faculty of Mechanical Engineering, Slovenia

Founders and Publishers
University of Ljubljana, Faculty of Mechanical Engineering, Slovenia
University of Maribor, Faculty of Mechanical Engineering, Slovenia
Association of Mechanical Engineers of Slovenia
Chamber of Commerce and Industry of Slovenia,
Metal Processing Industry Association

Founding Editor
Bojan Kraut
University of Ljubljana, Faculty of Mechanical Engineering, Slovenia

ISSN 0039-2480, ISSN 2536-2948 (online)

General information
Strojniški vestnik – Journal of Mechanical Engineering is published in 6 double issues per year.

Institutional prices include print & online access: institutional subscription price and foreign subscription €100,00 (the price of a single issue is €20,00); general public subscription and student subscription €50,00 (the price of a single issue is €10,00). Prices are exclusive of tax. Delivery is included in the price. The recipient is responsible for paying any import duties or taxes. Legal title passes to the customer on dispatch by our distributor. Single issues from current and recent volumes are available at the current single-issue price. To order the journal, please complete the form on our website. For submissions, subscriptions and all other information please visit: *http://www.sv-jme.eu.*

You can advertise on the inner and outer side of the back cover of the journal. The authors of the published papers are invited to send photos or pictures with short explanation for cover content.

Every manuscript submitted to the SV-JME undergoes a peer-review process. We would like to thank the reviewers who have taken part in the peer-review process. SV-JME is indexed / abstracted in: SCI-Expanded, Compendex, Inspec, ProQuest-CSA, SCOPUS, TEMA. The list of the remaining bases, in which SV-JME is indexed, is available on the website.

The journal is subsidized by Slovenian Research and Inovation Agency.

Strojniški vestnik - Journal of Mechanical Engineering is available on *https://www.sv-jme.eu*.

Contents

Strojniški vestnik - Journal of Mechanical Engineering
Volume 71, (2025), Number 1-2
Ljubljana, January-February 2025
ISSN 0039-2480
Published every two months

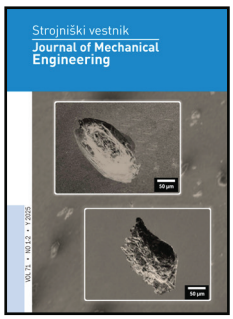

ON THE COVER

The corrosion behavior of dissimilar weldments between AISI 310 and AISI 2205 stainless steels in a 5 % calcium chloride solution at 50 °C was investigated under three conditions: as-welded, lower post-weld heat treatment at 800 °C, and higher post-weld heat treatment at 1000 °C. Microstructural examination revealed severe pitting in the as-welded sample. The lower heat-treated sample had larger pits, while the higher heat-treated sample showed homogeneous corrosion with a protective oxide coating. The as-welded sample had the highest corrosion rate, followed by the lower heat-treated sample, which had a moderate rate, and the higher heat-treated sample had the lowest rate. Electrochemical noise measurements confirmed these findings, with the higher heat-treated sample showing negligible localized corrosion and homogenous corrosion behavior.

Image Courtesy: Anna University, University College of Engineering, India

Corrosion Studies on Post-Weld Heat Treated Dissimilar AISI 2205 and AISI 310 Joints Using Electrochemical Noise Analysis

Mahadevan Govindasamy ✉ – Lloyd Jenner Mangalakaran Joseph Manuel – Senthilkumar Thamilkolunthu
Department of Mechanical Engineering, University College of Engineering, Anna University, India
✉ gmahadevan80@aubit.edu.in

Abstract *The corrosion behavior of dissimilar weldments between AISI310 and AISI2205 stainless steels in a 5 % calcium chloride solution at 50 °C was investigated under three conditions: as-welded, lower post-weld heat treatment at 800 °C, and higher post-weld heat treatment at 1000 °C. Microstructural examination revealed severe pitting in the as-welded sample, with pit widths ranging from 270 µm to 360 µm. The lower heat-treated sample had larger pits (310 µm to 370 µm), while the higher heat-treated sample showed homogeneous corrosion with a protective oxide coating. The as-welded sample had the highest corrosion rate, followed by the lower heat-treated sample, which had a moderate rate, and the higher heat-treated sample had the lowest rate. The corrosion current densities were 5.26×10^{-3} mA/cm², 4.6×10^{-4} mA/cm², and 1.4×10^{-4} mA/cm², respectively. Electrochemical noise measurements confirmed these findings, with the higher heat-treated sample showing negligible localized corrosion and homogenous corrosion behavior.*

Keywords *AISI2205, AISI310, corrosion, electrochemical impedance spectroscopy, $CaCl_2$*

Highlights:
- *Dissimilar AISI2205 and AISI310 joints were subjected to post weld heat treatment (PWHT) for improving its corrosion resistance.*
- *PWHT improved the corrosion characteristics of the dissimilar joints.*
- *Electrochemical noise evaluation revealed that noise intensity was lower in higher temperature PWHT 1000 °C than other joints.*

1 INTRODUCTION

The requirement for advanced engineering applications requires high-performance materials, often requiring welding of incompatible metals. Dissimilar stainless steel welding is particularly notable for its combined benefits of corrosion resistance, mechanical strength, and cost-effectiveness [1] and [2]. AISI 2205 duplex stainless steel and AISI 310 austenitic stainless steel are frequently used in industries such as chemical processing, oil and gas, and marine environments [3] and [4]. This combination leverages the high strength and weldability of duplex stainless steel with the high-temperature resistance of austenitic steel [5]. However, welding different stainless steels poses challenges, particularly regarding corrosion behavior, which affects the durability of welded structures in chloride-rich environments [6]. Welding can alter the microstructure at the weld junction, leading to variations in corrosion resistance [7]. Issues like residual stresses, phase transitions, and microstructural heterogeneities near the weld interface can become sites for localized corrosion, compromising joint integrity [8]. Research on corrosion in stainless steel welds focuses on factors like welding procedures, filler materials, and environmental conditions [9]. Galvanic corrosion, driven by the electrochemical potential difference between base metals, is a primary concern in dissimilar welds [10]. The corrosion behavior is significantly influenced by welding process parameters and post-weld heat treatment (PWHT) [11]. Calcium chloride ($CaCl_2$) solution is often studied for its resemblance to industrial chloride-rich conditions, which promote pitting and crevice corrosion in stainless steels [12] and [13]. PWHT mitigates the adverse effects of welding by relieving residual stresses and homogenizing the microstructure [14] and [15]. Methods such as high- and low-temperature treatments each affect the welded joint's properties differently [16]. Proper PWHT parameters can significantly enhance the corrosion resistance of dissimilar welds in harsh chloride environments [17]. This study evaluates the corrosion resistance of AISI2205-AISI310 dissimilar joints subjected to PWHT at two temperatures, using electrochemical techniques to monitor corrosion behavior in 5 % aqueous calcium chloride over 12 days.

2 MATERIALS & METHODS

2.1 Material Preparation and Welding

The base materials used in this research were AISI 310 stainless steel (SS) and AISI 2205 duplex stainless steel (DSS), both acquired from Kheteshwar Metals, Mumbai, India, as rolled sheets with a thickness of 5 mm. Selecting the right filler wire is crucial for achieving optimal joint quality. ER2205 filler wire is particularly sought after due to its lower ferrite content, which demonstrably improves weldability [18]. As a better option, 2.6 mm ER2205 filler wire was chosen for conducting welding studies. The chemical aspects of both the base material (BM) and filler wire were determined by using spark spectrometer. Sparks were ignited at various regions, and the elemental composition was subsequently recorded. The BMs were sectioned into rectangular pieces measuring 150 mm in length and 100 mm in width using abrasive cutting machine, and the edges were then properly ground. Then, the cut pieces underwent a thorough cleaning process for removing any dirt, oil, or impurities. The welding process was done using a single V-butt joint configuration. According to ASTM E8M 04 standards [19], V-shaped grooves were prepared with a 40º angle and a root gap of 1.2 mm [20].

DOI: 10.5545/sv-jme.2024.1084

A dual shielding gas controller and a customized GTAW welding setup were used for fabrication of the joints. A 2.4 mm diameter, 2 % thoriated tungsten electrode that was positioned at a 45° angle was used for the welding tests. The shielding gas was directed by a (12.2 mm internal diameter) nozzle that was positioned 5 mm distance. An electronic gas management unit was designed so that shielding gases could be switched between. Two timing circuits, one for each solenoid valve regulating the gases, were present in this machine. To maintain a balanced 50 % duty cycle, both gases were supplied at equal flow rates but alternated at regular intervals. Based on the reported literatures [21] and [22] and trial experiments, specific technological parameters for the welding experiments were selected and are detailed in Table 1.

Table 1. Designation of joints, welding parameters and heat treatment details

Joint	AISI310-AISI2205		
Designation	As-welded	LPWHT	HPWHT
Ageing temperature [°C]	-	800	1000
Welding current [A]	90 to 120	90 to 120	90 to 120
Welding voltage [V]	14 to 18	14 to 18	14 to 18
Welding speed [mm/s]	3.5	3.5	3.5
Gas flow rate [l/min]	8	8	8

After joining AISI310 SS with AISI2205 DSS, the specimens underwent PWHT. The dissimilar welds were heated for 90 minutes at two aging temperatures, namely 800 °C at lower post-weld heat treatment (LPWHT) and 1000 °C at higher post-weld heat treatment (HPWHT), and subsequently quenched in water. Three sets of joints were subjected to heat treatment, while one set was left untreated for comparative analysis. The designations for the heat-treated joints and information regarding aging temperatures are shown in Table 1.

2.2 Studies on Corrosion Characteristics

Aqueous calcium chloride with a concentration of 5 % was used to create the caustic solution. To conduct each experiment, 100 ml of corrosive solution was added to an open flask and heated to 55 ºC using an electrical heater. AISI2205-AISI310 dissimilar joints in as-welded, LPWHT and HPWHT conditions were used to make the electrodes. After being cut to the dimensions of 10 mm × 5 mm × 2 mm, the samples for the electrochemical procedures were polished using silicon carbide paper, rinsed with distilled water, cleaned with acetone, and dried in a warm air stream. For the electrical connection, the specimens were spot-welded to a 150 mm long, 1 mm diameter 80.0Cr-20.0Ni wire. This wire was then separated from the corrosive solution by enclosing it in glass tubes and filling the gap between

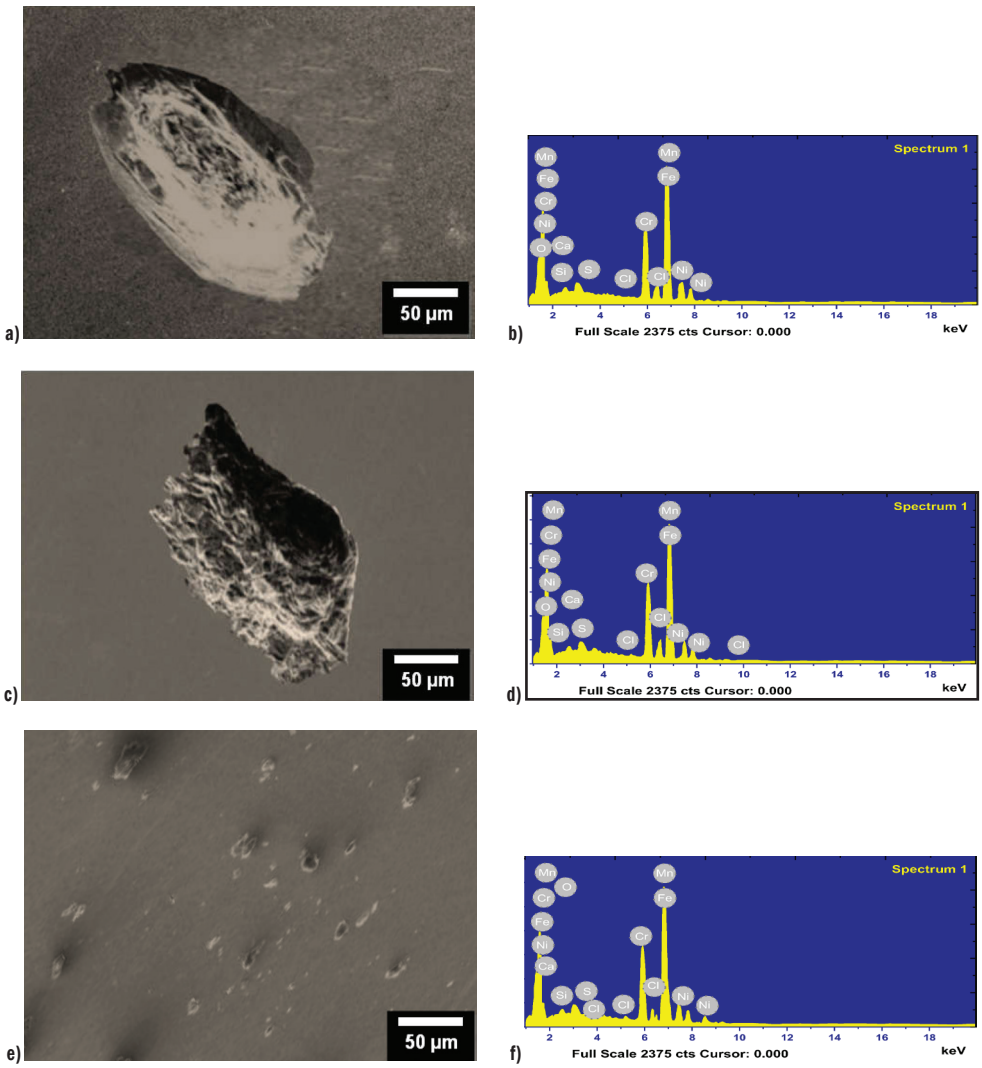

Fig. 1. Micrographs and EDX analysis of dissimilar AISI310-AISI2205 samples exposed to an aqueous $CaCl_2$ solution: a) SEM as-welded sample, b) ADYX as welded sample in the as-welded condition, c) SEM – LPWHT sample, d) EDAX – LPWHT sample, e) SEM – HPWHT sample, and f) EDAX – HPWHT sample

the glass tubes and the electrical connecting wire with refractory silicon. Applying over-potential with a sweep rate of 1 mV/s, ranging from –400 mV below to 800.0 mV above the corrosion potential, the polarization curves were developed [23] and [24].

The electrochemical cell consisted of working electrodes (as-welded, PWHT1, PWHT2), a reference electrode (Ag/AgCl), and an auxiliary electrode (platinum wire). Electrochemical potential and current noise measurements were carried out using a three 'identical' electrode configuration, with one reading per second to compile records of 1024 points every four hours for 12 days. All three electrochemical procedures were performed with an ACM Gill 8AC potentiostat accurately controlled by a personal computer. For qualitative examination, the surface morphology of the corroded specimens was investigated using scanning electron microscopy (SEM) in conjunction with energy dispersive X-ray analysis (EDAX). The SEM examination was carried out utilizing the JEOL JSM-6490LV microscope.

3 RESULTS AND DISCUSSION

3.1 SEM-EDX Analysis

SEM-EDX images of the three corroded dissimilar AISI2250-AISI310 joints (as-welded, LPWHT & HPWHT) which underwent corrosion in CaCl2 solution are shown in Fig. 1a and b, Fig. 1c and d and Fig. 1e and f, respectively.

According to the SEM with EDX examination, the three types of welded samples exhibit diverse corrosion behaviors. The as-welded sample exhibited heavily corroded surface with pits ranging from 270 µm to 360 µm in diameter. EDX analysis found chloride species, indicating that chromium and iron were selectively dissolved, most likely as chlorides. This mixed corrosion process shows localized pitting and general degradation, which are characteristic of untreated weld joints exposed to chloride [25]. The LPWHT sample indicated a morphology similar to the as-welded condition, but with slightly larger pits (310 µm to 370 µm). This indicated that, while LPWHT at 800 °C was intended to relieve tensions and polish the microstructure, it was not completely efficient in preventing the beginning of localized pitting corrosion, particularly in chloride environments. Localized pitting and similar elemental trends reported in both LPWHT and as-welded samples lend support to this theory. The HPWHT sample exhibited an evenly corroded surface with no pits. EDX examination revealed the creation of a protective oxide layer predominantly formed of chromium and iron oxides, with nickel and manganese present in trace levels [26]. Surface ruptures occur in as-welded samples because there is no persistent oxide layer, resulting in localized pitting and selective dissolving of alloy components such as chromium and iron. This makes the surface susceptible to hostile substances such as chlorides. In HPWHT samples, high-temperature treatment promotes the creation of a homogeneous and protective oxide layer, predominantly composed of chromium and iron oxides, which greatly lowers surface deterioration and the risk of localized corrosion. This homogeneous corrosion pattern, together with the existence of a persistent oxide layer, suggests that HPWHT at 1000 °C effectively reduces localized corrosion, offering increased resistance to chloride-induced pitting [27].

3.2 Polarization Curves

Fig. 2 presents the polarization curves of AISI310-AISI2250 at as-welded, LPWHT and HPWHT conditions. The parameters of potentiodynamic polarization curves of dissimilar joints AISI2205-AISI310 with different PWHT conditions exposed in the corrosive solution are shown in Table 2. At higher temperatures, the as-welded, LPWHT, and HPWHT samples behaved differently, according to the corrosion characteristics (Table 2).

Table 2. Parameters of potentiodynamic polarization curves of dissimilar joints AISI2205-AISI310 with different PWHT conditions exposed in the corrosive solution

	AISI2205-AISI310 dissimilar joint	AISI2205-AISI310	AISI2205-AISI310
Condition	As-welded	LPWHT	HPWHT
β_a [mV/decade]	304.7	291.2	134.6
β_c [mV/decade]	71.2	99.6	51.3
E_{corr} [mV]	231.3	–14.8	56.9
I_{corr} [mA/cm^2]	5.26×10^{-3} mA/cm^2	4.6×10^{-4} mA/cm^2	1.4×10^{-4} mA/cm^2

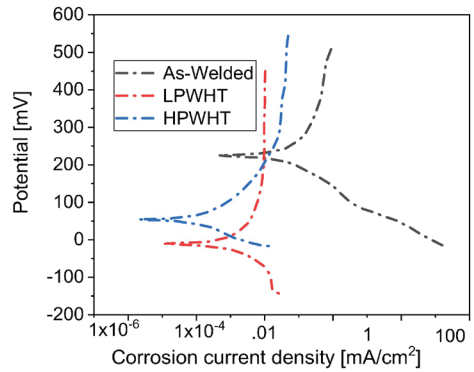

Fig. 2. Polarization curves of AISI310-AISI2250 at as-welded, LPWHT and HPWHT

The as-welded sample had the maximum corrosion rate ($\beta_a = 304.7$ mV/decade, $\beta_c = 71.2$ mV/decade). The corrosion potential E_{corr} was measured at 231.3 mV, and the corrosion current density I_{corr} was 5.55×10^{-3} mA/cm², suggesting maximal susceptibility. Corrosion potential (E_{corr}) denotes a material's ability to corrode; a lower E_{corr} indicates greater susceptibility. Corrosion current density (I_{corr}) indicates the rate of material degradation. Higher I_{corr} values, as seen in the as-welded sample, indicate faster corrosion and a greater sensitivity to corrosion in severe conditions. In comparison to the as-welded sample, the LPWHT sample demonstrated a moderate improvement in corrosion resistance. With β_a at 291.2 mV/decade and β_c at 99.6 mV/decade, the corrosion potential E_{corr} was found to be –14.8 mV.

The corrosion current density was 4.71×10^{-4} mA/cm² (I_{corr}), indicating a medium corrosion rate. Among the samples tested, sample C (HPWHT) exhibited the superior resistance to corrosion. This was evident by its lowest Tafel slopes (β_a at 134.6 mV/decade and β_c at 51.3 mV/decade). Additionally, it had the lowest corrosion potential (E_{corr} at 56.9 mV) and current density (I_{corr} at 1.45×10^{-4} mA/cm²), signifying minimal corrosion susceptibility.

3.3 Electrochemical Noise Measurements

Fig. 3 presents the current and potential time series at 55 ºC for as-welded, LPWHT and HPWHT. These data were used for showing the major localized corrosion activity, taking into account the three typical forms of electrochemical noise generated by different types of corrosion processes [28]:

a. Type I (Pitting): Consist of transients of high intensity with a high repetition rate. This type of corrosion is often characterized by the sudden appearance of small holes or pits in the metal surface.

b. Type II (Mixed): It is a combination of transients of type I and oscillations of short amplitude. This type of corrosion suggests a combination of localized pitting and a more general attack on the metal surface.
c. Type III (Uniform): The pattern noise is formed by oscillations of low amplitude. This type of corrosion refers to a gradual and relatively even attack on the entire exposed metal surface.

The as-welded specimens exhibited the highest corrosion rate, indicated by significantly higher current density values compared to LPWHT and HPWHT. As-welded specimens generally showed potential and current time series with random oscillations of extremely low intensity, resembling those observed at LPWHT & HPWHT. In comparison to LPWHT & HPWHT samples, the potential noise for as-welded specimens showed a greater range, roughly 118 mV, suggesting a nobler nature. This is consistent with the distinct way that the $CaCl_2$ corrosion system responds to heat treatment and lines up with the behavior shown in the polarization curves. LPWHT sample's current and potential time series showed a clear noise pattern with noticeable transients and oscillatory behavior. In electrochemical noise studies, oscillatory behavior in LPWHT samples showed occasional breakdown and recovery of the passive oxide layer caused by localized pitting corrosion [29]. This indicated increased activity, especially on 5th and 6th day, which was compatible with localized corrosion or the breakdown and recovery

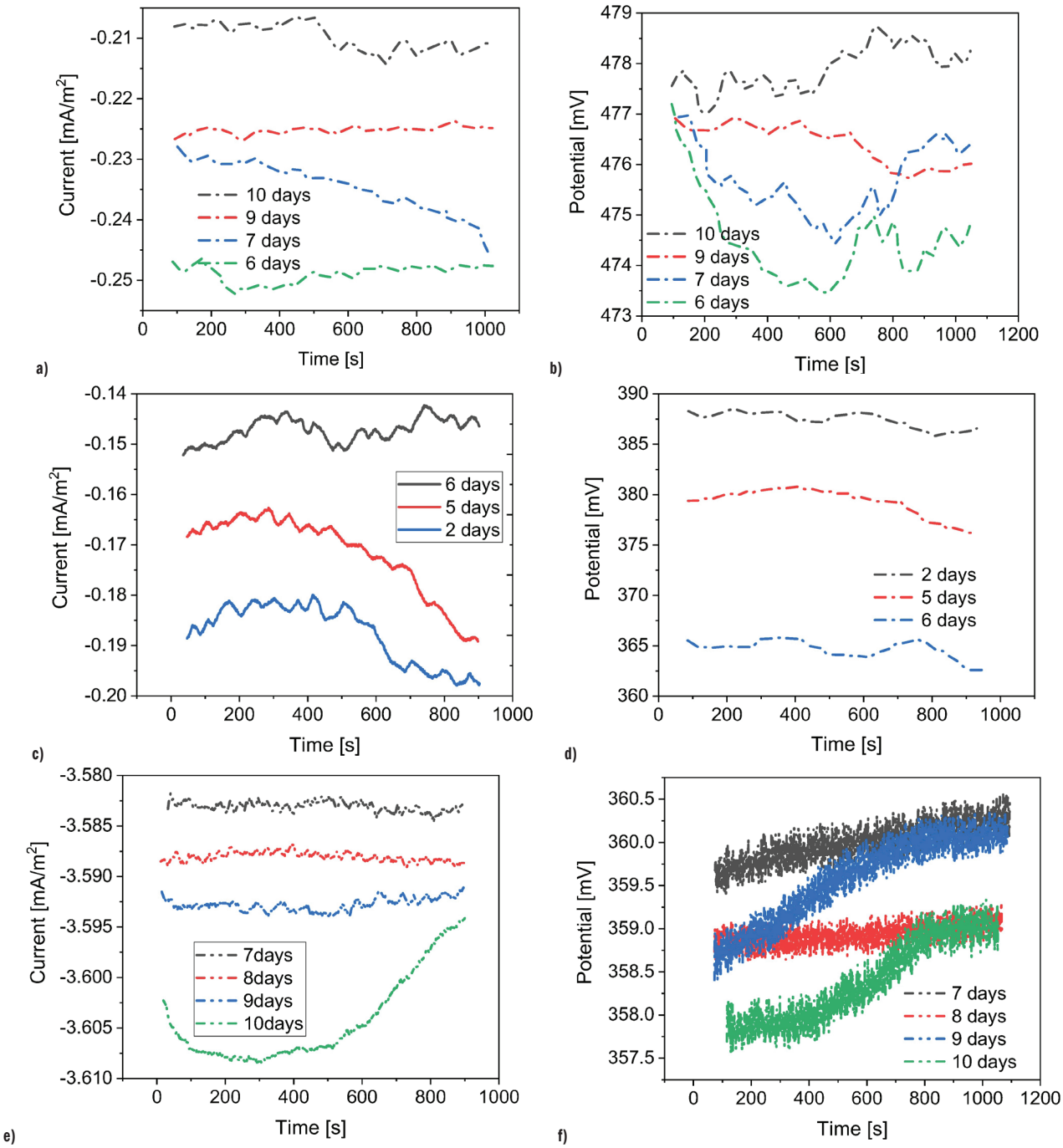

Fig. 3. Current and potential time series of the dissimilar joints exposed to $CaCl_2$ solution; a) current time series for as-welded, b) potential time series for as-welded, c) current time series for LPWHT, d) potential time series for LPWHT, e) current time series for HPWHT, and f) potential time series for HPWHT

of the passive film. Interestingly, the transient activity that was seen on those days did not persist for the duration of the experiment, suggesting that the process was localized and only took place on those days. It is possible to interpret the notable transients seen on those two days as the rupture of the passive oxide coating or localized corrosion events because they were marked by abrupt current rises, potential decreases, and recovery. The rupture of the passive oxide coating in LPWHT samples happens when the protective film that typically protects the metal from corrosion becomes unstable due to localized pressures, impurities, or environmental conditions. This disintegration exposes the underlying metal to corrosive chemicals, which accelerates localized corrosion. Factors such as chloride ions, temperature variations, and mechanical stressors can all weaken the oxide layer and cause it to break. Once the protective coating is compromised, corrosion accelerates until the oxide layer reforms or stabilizes [30].

Even though these transients were noticeable on those two days, the remaining time series showed low-amplitude random oscillations that might have contributed to the localised activity in addition to a mixed corrosion process [31]. This aligned with the findings from the SEM analysis, indicating both techniques identified the susceptibility of AISI2205-AISI310 joints to a combination of localized and mixed corrosion processes. HPWHT showed no notable anodic or cathodic transients in the current and potential time series, in line with the as-welded condition. For HPWHT, the current density stayed negative and extremely low, indicating a low expected rate of corrosion. The cathode electrode's preferential dissolution was indicated by the negative values, which essentially reversed the direction of the current. The present time series indicated low-amplitude random oscillations without any notable anodic transients and just two notable cathodic transients that would indicate the metallic oxide film recovering [32]. As-welded specimens displayed markedly higher current densities than PWHT2, indicating accelerated corrosion rates with rising temperature, a characteristic observed in the $CaCl_2$ corrosion system as reported in previous studies [33].

3.4 Localization Index

The localization index (LI) was computed in order to measure the correlation between the electrochemical noise signals and the corrosion process. Localized corrosion activity is shown by *LI*, which is the ratio of the current noise standard deviation (σ_i) to the root-mean-square current value (I_{rms}). The range of *LI* values, typically between 0 and 1, is taken into account in the study. *LI* approaches 1 for current fluctuations that are noticeably greater than the mean current. On the other hand, *LI* values near 0 suggest that current fluctuations are negligible in relation to the mean current [34].

Localization index of AISI2205-AISI310 dissimilar joints exposed to $CaCl_2$ at different PWHT conditions are shown in Fig. 4. Throughout the experiment, *LI* values were computed from each time series record derived from the electrochemical noise measurements. Values for the localization index were primarily found in the interval between the uniform and mixed corrosion zones. The mixed corrosion zone was primarily where the *LI* of the as-welded sample was located. This observation was consistent with multiple transients being present in the electrochemical noise pattern, indicating a combination of more widespread corrosion processes and localized assault. Multiple transients in the *LI* show the presence of various corrosion mechanisms, including both localized and uniform corrosion processes. This indicates that the electrochemical environment is unstable, with fast swings in corrosion activity resulting in pitting and general degradation, which is typical of mixed corrosion behavior [35]. SEM data, which show a greater vulnerability to localized corrosion attack, supported this observation.

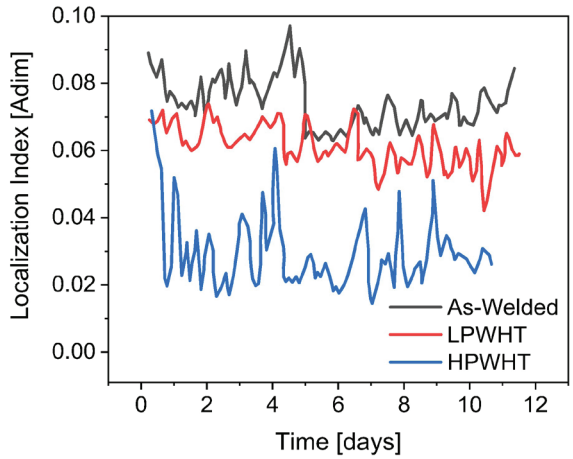

Fig. 4. Localization index (dimensionless) of AISI2205-AISI-310 dissimilar joints exposed to CaCl2 at different PWHT conditions

The LPWHT sample exhibited *LI* values positioned near the border between uniform and mixed corrosion zones. This suggested an intermediate behavior, where localized corrosion was less pronounced compared to the as-welded condition. In mixed corrosion zones, intermediate behavior in LPWHT samples results from partial stabilization of the passive oxide layer, which reduces the severity of localized corrosion when compared to as-welded samples. This results in less noticeable pitting while yet allowing for some localized attack, showing a balance of uniform and localized corrosion processes [36] and [37]. This might be attributed to the absence of significant transients in the corresponding electrochemical noise data, potentially indicating a reduction in localized activity due to the low-temperature post-weld heat treatment. In contrast, the HPWHT sample maintained the *LI* firmly within the uniform or generalized corrosion zone. This consistency aligned with the minimal transients observed in the electrochemical noise pattern, suggesting a predominantly uniform corrosion process [38].

4 CONCLUSIONS

The corrosion performance of post-weld heat-treated AISI2205-AISI310 dissimilar stainless steel joints exposed to a 5 % $CaCl_2$ solution for twelve days was investigated experimentally. The study incorporated SEM analysis alongside polarization curves, electrochemical noise data, and electrochemical impedance plots. According to the results, LPWHT joints and as-welded joints displayed a mixed corrosion process, while HPWHT joints (treated at 1000 ºC) displayed a uniform corrosion process. HPWHT joints had noise signals with a low amplitude and high-frequency pattern, according to electrochemical noise analysis, which coincided with the uniform corrosion that was seen visually. As-welded and LPWHT joints, on the other hand, showed many medium-intensity transients, indicating a more intricate corrosion process. A helpful indicator of corrosion localization was produced by the localization index parameter, which matched the visual observations of the corroded samples quite well.

REFERENCES

[1] Maurya, A.K., Pandey, C., Chhibber, R. Dissimilar welding of duplex stainless steel with Ni alloys: A review. *Int J Press Vessels Pip* 192 104439, (2021) **DOI:10.1016/j.ijpvp.2021.104439**

[2] Verma, J., Taiwade, R.V. Effect of welding processes and conditions on the microstructure, mechanical properties and corrosion resistance of duplex stainless steel weldments-A review. *J Manuf Process* 25 134-152 (2017) **DOI:10.1016/j.jmapro.2016.11.003**

[3] Zhu, P., Cao, X., Wang, W., Zhao, J., Lu, Y., Shoji, T. (2017). An investigation on microstructure and pitting corrosion behavior of 316L stainless steel weld joint. *J Mater Res* 32 3904-3911 **DOI:10.1557/jmr.2017.316**

[4] Xiong, J., Tan, M.Y., Forsyth, M. The corrosion behaviors of stainless steel weldments in sodium chloride solution observed using a novel electrochemical measurement approach. *Desalination*, 327 39-45, (2013) **DOI:10.1016/j.desal.2013.08.006**

[5] Touileb, K., Hedhibi, A. C., Djoudjou, R., Ouis, A., Bensalama, A., Ibrahim, A., Ahmed, M.M. Mechanical, microstructure, and corrosion characterization of dissimilar austenitic 316L and duplex 2205 stainless-steel ATIG welded joints. *Materials* 15 2470 (2022), **DOI:10.3390/ma15072470**

[6] Xiong, J., Tan, M.Y., Forsyth, M. (2013). The corrosion behaviors of stainless steel weldments in sodium chloride solution observed using a novel electrochemical measurement approach. *Desalination*, 327 39-45 **DOI:10.1016/j.desal.2013.08.006**

[7] Mohamed, A.Y., Mohamed, A.H.A., Abdel Hamid, Z., Farahat, A.I.Z., El-Nikhaily, A.E. Effect of heat treatment atmospheres on microstructure evolution and corrosion resistance of 2205 duplex stainless steel weldments. *Sci Rep* 13 4592 (2023) **DOI:10.1038/s41598-023-31803-5**

[8] Rao, P., Mulky, L. An overview of microbiologically influenced corrosion on stainless steel. *Chem Bio Eng Rev* 10 829-840 (2023) **DOI:10.1002/cben.202300001**

[9] Raj, S., Biswas, P. Experimental investigation of the effect of induction preheating on the microstructure evolution and corrosion behaviour of dissimilar FSW (IN718 and SS316L) joints. *J Manuf Process* 95 143-159 (2023) **DOI:10.1016/j.jmapro.2023.04.021**

[10] Okonkwo, B.O., Ming, H., Li, Z., Li, L., Chen, Y., Peng, J., Wang, J. Insight into the galvanic corrosion behaviour of low alloy steel A508/309 L/308 L stainless steel dissimilar metal weld at different temperatures. *Mater Today Comm* 38 107963. (2024) **DOI:10.1016/j.mtcomm.2023.107963**

[11] Liao, T., Zhang, X., Yang, H., Zhou, P., & Chen, F. Microstructural evolution and micro-corrosion behaviour of flash-welded U71Mn Joints as a function of post-weld heat treatment. *Materials* 16 5437 (2023) **DOI:10.3390/ma16155437**

[12] Vucko, F., Nazarov, A., Helbert, V., Thierry, D., Pelletier, S., Pablo, H., et al. Wet corrosion of incinerators under chloride deposits: insights from experimental study on stainless steels and nickel-based alloy weldments. *Corros Sci* 112220 (2024) **DOI:10.1016/j.corsci.2024.112220**

[13] Costa, E.M., Dedavid, B.A., Santos, C.A., Lopes, N.F., Fraccaro, C., Pagartanidis, T., Lovatto, L.P. Crevice corrosion on stainless steels in oil and gas industry: A review of techniques for evaluation, critical environmental factors and dissolved oxygen. *Eng Fail Anal* 144 106955 (2023) **DOI:10.1016/j.engfailanal.2022.106955**

[14] Singh Raman, R.K., Siew, W.H. Microstructures and corrosion/localised corrosion of stainless steels, incoloy and their weldments in nitrite-containing chloride environments. *Materials* 17 1336 (2024) **DOI:10.3390/ma17061336**

[15] Tahaei, A., Vanani, B.B., Abbasi, M., Garagnani, G.L. A comparison of microstructure and mechanical characteristics correlation of the joint specimens for duplex stainless steel UNS S32304 and super-duplex stainless steel UNS S32750: The role of post-weld heat treatment. *P I Mech Eng L-J Mat* (2024) **DOI:10.1177/14644207241233150**

[16] Tuz, L., Sokołowski, Ł., Stano, S. Effect of post-weld heat treatment on microstructure and hardness of laser beam welded 17-4 PH stainless steel. *Materials* 16 1334 (2023) **DOI:10.3390/ma16041334**

[17] Khan, M., Dewan, M.W., Sarkar, M.Z. Effects of welding technique, filler metal and post-weld heat treatment on stainless steel and mild steel dissimilar welding joint. *J Manuf Process* 64 1307-1321 (2021) **DOI:10.1016/j.jmapro.2021.02.058**

[18] Hung, C.H., Chen, W.T., Sehhat, M.H., Leu, M.C. The effect of laser welding modes on mechanical properties and microstructure of 304L stainless steel parts fabricated by laser-foil-printing additive manufacturing. *Int J Adv Manuf Tech* 112 867-877 (2021) **DOI:10.1007/s00170-020-06402-7**

[19] ASTM E8M-04. Standard Test Methods for Tension Testing of Metallic Materials [Metric Units]. American Society for Testing and Materials (ASTM) (2004) West Conshohocken **DOI:10.1520/E0008_E0008M-22**

[20] Lei, Z., Cao, H., Cui, X., Jin, G., Xu, K., Jiang, B., Huang, R. (2022). Analysis of welding solidification crack in narrow gap laser welding of high-strength steel. *Int J Adv Manuf Tech* 119, 4177-4190 **DOI:10.1007/s00170-022-08659-6**

[21] Dong, H., Yang, J., Li, Y., Xia, Y., Hao, X., Li, P., Lei, M. Evolution of interface and tensile properties in 5052 aluminum alloy/304 stainless steel rotary friction welded joint after post-weld heat treatment. *J Manuf Process* 51, 142-150 (2020) **DOI:10.1016/j.jmapro.2020.01.038**

[22] Köse, C., Topal, C. Effect of heat input and post-weld heat treatment on surface, texture, microstructure, and mechanical properties of dissimilar laser beam welded AISI 2507 super duplex to AISI 904L super austenitic stainless steels. *J Manuf Process* 73 861-894 (2022) **DOI:10.1016/j.jmapro.2021.11.040**

[23] Fontinha, I.R., Eustáquio, E. Influence of exposure conditions and particulate deposition on anodized aluminum corrosion. *Corr Mater Degrad* 3 770-786 (2022) **DOI:10.3390/cmd3040040**

[24] Hu, S., Liu, R., Liu, L., Cui, Y., Wang, F. Influence of temperature and hydrostatic pressure on the galvanic corrosion between 90/10 Cu-Ni and AISI 316L stainless steel. *J Mater Res Tech* 13 1402-1415 (2021) **DOI:10.1016/j.jmrt.2021.05.067**

[25] Wang, X, Chen, X., Han, Z., Li, C. Wang, Q. Stress corrosion cracking behavior of 2205 duplex stainless steel in 3.5% NaCl solution with sulfate reducing bacteria. *J Chinese Soc Corr Prot* 41 43-50 (2021) **DOI:10.1016/S0010-938X(99)00105-5**

[26] Dak, G., Sirohi, S., Pandey, C. Study on microstructure and mechanical behavior relationship for laser-welded dissimilar joint of P92 martensitic and 304L austenitic steel. *Int J Press Vess Pip* 196 104629 (2022) **DOI:10.1016/j.ijpvp.2022.104629**

[27] Bozeman, S.C. *The Processing and Microstructures of 309L Stainless Steel Clad onto Carbon Steel with Wire-fed Directed Energy Deposition.* Msc Thesis, Oregon State University, Corvallis (2022).

[28] Parvizi, R. *Electrochemical and interfacial characterisation of localised corrosion at heterogeneous structures in AA2024*. PhD Thesis, Deakin University, Victoria, (2022)

[29] Li, J., Jia, C., Gao, S., Guo, L. (2024). Experimental and numerical study on axial compression behavior of slender CFST columns with localized pitting corrosion damage. *Constr Build Mater* 414 134858 **DOI:10.1016/j.conbuildmat.2023.134858**

[30] Singh, J., Shahi, A.S. Microstructure and corrosion behavior of duplex stainless steel electron beam welded joint. *J Mater Sci* 57 9454-9479 (2022) **DOI:10.1007/s10853-022-07241-5**

[31] Jiang, L., Zhang, Z., Fu, H., Huang, S., Zhuang, D., Xie, J. Corrosion behavior and mechanism of Al-Zn-Mg-Cu alloy based on the characterization of the secondary phases. *Mater Charact* 189, 111974 (2022) **DOI:10.2139/ssrn.4009387**

[32] Örnek, C., Davut, K., Kocabaş, M., Bayatlı, A., Ürgen, M. Understanding corrosion morphology of duplex stainless steel wire in chloride electrolyte. Corr Mater Degr 2 397-411 (2021) **DOI:10.3390/cmd2030021**

[33] Hammood, A.S., Esmailzadeh, M., Hosseini, S.N., Karimi, S., Calliari, I., Pezzato, L., Brittain, R. Effect of friction stir welding parameters on microstructure and corrosion behavior of 2101 duplex stainless steel in simulated body fluid. *Int J Pr Eng Man-GT* 10 327-337 (2023) **DOI:10.1007/s40684-022-00440-0**

[34] Amiri, E., Ostovan, F., Toozandehjani, M., Shafiei, E., Mohamed, I.F. Study and selection of most appropriate filler rod for GTAW of S32750 super duplex steel joints: A comprehensive study on microstructural, mechanical and corrosion properties. *Mater Chem Phys* 270 124839 (2021) **DOI:10.1016/j.matchemphys.2021.124839**

[35] Wang, Q., Zhang, Q., Zheng, H., Liu, L., Wu, X., Zhao, C Li, X. (2023). Insight into anti-corrosion behavior of protein extract as eco-friendly corrosion inhibitor. *Sust Chem Pharm* 34 101177 **DOI:10.1016/j.scp.2023.101177**

[36] Örnek, C., Davut, K., Kocabaş, M., Bayatlı, A., Ürgen, M. Understanding corrosion morphology of duplex stainless steel wire in chloride electrolyte. *Corr Mater Degr* 2 397-411. (2021) **DOI:10.3390/cmd2030021**

[37] Lovše, A., Skale, S., Vojvodić-Tuma, J. Evaluation of the Condition of the Bottom of the Tanks for Petroleum Products-Forecast of the Remaining Operating Life. *Stroj Vestn-J Mech E*, 70, 282-292. (2024) **DOI:10.5545/sv-jme.2023.682**

[38] Calabrese, L., Galeano, M., Proverbio, E. Data mining applied to the electrochemical noise technique in the time/frequency domain for stress corrosion cracking recognition. *Corr Mater Degr* 4 659-679 (2023) **DOI:10.3390/cmd4040034**

Acknowledgement

The authors would like to thank National Central Instrumentation Facility, Tamil Nadu, India for assistance in microstructural evaluation and M/s.Vikram Engineering Industry, Trichy, Tamil Nadu, India for assistance in welding and heat treatment studies.

Received 2024-07-03, revised 2024-09-29, accepted 2024-11-05,
Original Scientific Paper.

Data availability *The data supporting the study's findings are included in the paper.*

Author contribution *Mahadevan Govindasamy contributed to data curation, drafting; Lloyd Jenner Mangalakaran Joseph Manuel contributed to analysis; and Senthilkumar Thamilkolunthu contributed to implementation of the work.*

Študija korozije neenakih zvarov AISI2205 in AISI310 po varjenju z elektrokemično analizo šuma

Povzetek *Korozijsko obnašanje neenakih zvarov nerjavnih jekel AISI310 in AISI2205v 5-odstotni raztopini kalcijevega klorida pri 50 °C je bilo raziskano pod tremi pogoji: kot varjeno, z nižjo toplotno obdelavo po varjenju pri 800 °C in z višjo toplotno obdelavo po varjenju pri 1000 °C. Mikrostrukturna analiza je pokazala izrazito jamasto korozijopri varjenem vzorcu, pri čemer so bile širine jamic med 270 µm in 360 µm. Vzorec z nižjo toplotno obdelavo je imel večje vdolbine (310 µm do 370 µm), medtem ko je pri vzorcu, ki je bil toplotno obdelan višje, opaziti homogeno korozijo z zaščitno oksidno prevleko. Najvišjo stopnjo korozije je imel varjeni vzorec, sledil mu je nizko-toplotno obdelani vzorec z zmerno stopnjo, najnižjo stopnjo korozije pa je imel visoko-toplotno obdelani vzorec. Gostote korozijskega toka so bile* $5{,}26 \times 10^{-3}$ *mA/cm²,* $4{,}6 \times 10^{-4}$ *mA/cm²* *oziroma* $1{,}4 \times 10^{-4}$ *mA/cm². Elektrokemične meritve šuma so potrdile te ugotovitve, pri čemer je vzorec, ki je bil obdelan z višjo toplotno obdelavo, pokazal zanemarljivo lokalizirano korozijo in homogeno korozijsko obnašanje.*

Ključne besede *AISI2205, AISI310, korozija, elektrokemijska impedančna spektroskopija,* $CaCl_2$

Thermal Design and Constrained Optimization of a Fin and Tube Heat Exchanger Using Differential Evolution Algorithm

Nader Afsharzadeh – Mohammad Eftekhari Yazdi ✉ – Arash Mirabdolah Lavasani
Islamic Azad University, Department of Mechanical Engineering, Iran
✉ moh.eftekhari_yazdi@iauctb.ac.ir

Abstract *Fin and tube heat exchangers (FTHEs) are utilized for gas-liquid applications frequently. In the current study, a differential evolution (DE) algorithm and JDE as its variant, with α-level constraint-handling technique, are effectively applied to optimize an FTHE. Total weight and total annual cost are selected as objective functions. Seven design variables are taken into consideration: outside tube diameter, transverse pitch, longitudinal pitch, fin pitch, number of tube rows, height, and width of shape. Meanwhile, the logarithmic mean temperature difference (LMTD) method is used for heat transfer analysis under identical conditions such as mass flow rate, inlet and outlet temperatures, heat duty, and other thermal properties. The research findings indicate that the implementation of the DE algorithm coupled with α-level comparison method on optimization problems leads to better solutions for both objective functions compared with those achieved by other approaches such as the genetic algorithm (GA) and heat transfer search (HTS) algorithm. In addition, a parametric analysis is performed for design parameters at the optimum points to show the effects on the objective functions and to identify the feasible design space. The proposed method is straightforward and can generally be employed for thermal design and optimization of FTHEs as well as any other type of compact heat exchangers (CHEs) under different specified duties.*

Keywords *Fin and tube heat exchanger, thermal design, constrained optimization, differential evolution (DE) algorithm, total weight, total annual cost*

Highlights
- *Compact heat exchangers aim to minimize weight and annual cost in industrial use.*
- *Metaheuristic algorithms outperform trial-and-error methods in optimization.*
- *Differential evolution with α-level constraints achieves superior optimization results.*
- *Proposed method cuts weight by 9.33% and cost by 6.87 % from previous best results.*

1 INTRODUCTION

The process of heat exchange between two fluids that are at different temperatures and separated by a solid wall occurs in many engineering applications. The device used to implement this exchange is termed a heat exchanger (HE), and specific applications may be found in space heating and air-conditioning, power production, waste heat recovery, and chemical processing [1]. The area density is the ratio of heat transfer surface to HE volume. A compact heat exchanger (CHE) has a high area density compared to traditional HEs. CHEs are highly effective and low in weight and cost. Fins are used on the gas side of CHEs to compensate for high thermal resistance and enhance the heat transfer coefficient. Plate-fin heat exchangers (PFHEs), fin and tube heat exchangers (FTHEs), and rotary regenerators are examples of CHEs for gas flow on one or both fluid sides [2].

The most common criteria for the optimization of CHEs are the minimum initial cost, minimum operation cost, maximum effectiveness, minimum pressure drop, minimum heat transfer area, minimum weight, or material. The optimization of a CHE can be transformed into a constrained optimization problem and then solved by modern optimization algorithms [3].

The following could be highlighted after looking into the studies accomplished on the thermal design and optimization of PFHEs: Rao and Patel [4] applied the particle swarm optimization (PSO) algorithm for the thermodynamic optimization of a PFHE based on three individual objective functions: total number of entropy generation units, total volume, and total annual cost. Ahmadi et al. [5] used the ε-NTU method and a nondominated sorting genetic algorithm (GA) for the thermal modeling of a PFHE to minimize cost and entropy generation. Wang and Li [6] introduced and carried out an improved multi-objective cuckoo search (IMOCS) algorithm for multi-objective optimization, including efficiency maximization, minimization of pumping power, and total annual cost. Hajabdollahi [7] compared two cases of similar and non-similar fins on each side of the PFHE by using a PSO algorithm for thermo economic optimization.

If one fluid is a liquid, different fin and tube configurations are frequently used; the liquid passes through the tubes while the gas flows across the bank of finned tubes. Various tube shapes might be used such as circular tubes, ovals, rectangles, and any other complex type. Compressor inter-coolers, air-coolers, and fan coils are examples of power engineering and chemical applications that employ FTHEs. Xie et al. [8] and Raja et al. [9] were seeking to achieve the optimal design of an FTHE based on total weight and total annual cost by employing GA and heat transfer search (HTS) algorithms, respectively.

Compared to most other evolutionary algorithms (EAs), differential evolution (DE) is much simpler and more straightforward to implement. The main body of the algorithm takes a few lines to code in any programming language. Also, the performance of DE and its variants is largely better than other optimization algorithms such as PSO, PCX, ALEP, etc. [10]. Babu et al. [11] applied DE algorithm and its various strategies for the optimal design of shell and tube heat exchangers. Ayala et al. [12] proposed a novel multi

 DOI: 10.5545/sv-jme.2023.887

objective free search (FS) approach combined with DE (MOFSDE) algorithm for heat exchanger optimization. Segundo et al. [13] by considering a shell-and-tube heat exchanger and the total annual cost as the objective function, employed DE algorithm, and Tsallis differential algorithm (TDE) to optimize it. Also, Yuan et al. [14] compared two helically coiled tubes' heat transfer characteristics and hydrodynamics by implementing an adaptive multi-objective optimization DE algorithm.

Now, what is the best solution? Perhaps, this is the main question that arises in an engineering optimization problem. However, in most discussed thermal design and optimization studies about CHEs, penalty function-based methods are employed to handle the constraints and seldom can achieve a global solution that satisfies all constraints. Differential evolution with Level Comparison (DELC) for the first time is proposed by Wang and Li [15] and achieves superior searching quality on all the problems with fewer evaluation times than other algorithms. In this paper, DELC and JDE as a variant of standard DE with level comparison (JDELC) are applied to the thermal design and optimization problem of an FTHE.

The remainder of this paper is organized as follows: In Section 2, an FTHE is modeled by using a closed-form equation to predict the heat transfer coefficient. The next section introduces objective functions including total weight and total annual cost in addition to corresponding constraints. Section 4 is about the traditional design method used for FTHEs. Section 5 demonstrates the DE algorithm and employs DE and JDE based on the α-level constraint-handling technique. Section 6 illustrates a case study of FTHE and explains the results and discussion. In Section 7, a parametric analysis is carried out to obtain feasible design space. Finally, the conclusions are delivered in Section 8, followed by the list of symbols and the list of references.

2 THERMAL DESIGN

In the present work, an intercooler is considered as an FTHE with a plain-fin type in which hot air flows normally to a finned tube bundle while cold water flows inside tubes, as illustrated in Fig. 1. However, it is common to use other types of fins, such as wavy, slotted, and louvered.

2.1 Heat Transfer

For the geometry calculations of staggered tube arrangement, the minimum free flow area on the airside is given by the following Eq. (1) [2]:

$$A_{min}=\left[\left(\frac{H}{P_t}-1\right)c+\left(P_t-d_o\right)\left(1-t_fN_f\right)\right]W, \tag{1}$$

where

$$\begin{cases} c=2a & \text{if} \quad 2a<2b \\ c=2b & \text{if} \quad 2b<2a \end{cases}. \tag{2}$$

Values of $2a$ and b are determined as follows:

$$2a=\left(P_t-d_o\right)\left(1-t_fN_f\right), \tag{3}$$

$$b=\left(\left(0.5P_t\right)^2+P_l^2\right)^{0.5}-d_o-\left(P_t-d_o\right)t_fN_f. \tag{4}$$

The total heat transfer area of the heat exchanger is calculated as:

$$A=A_p+A_f, \tag{5}$$

where, A_p and A_f are the primary and secondary (i.e., fin) surface area of the heat exchanger, respectively, and obtained by,

$$A_p=\pi d_oWN_t\left(1-t_fN_f\right), \tag{6}$$

$$A_f=2N_fW\left(LH-\frac{\pi}{4}d_o^2N_t\right)+2t_fN_fWH, \tag{7}$$

where N_t is the number of tubes and N_f is the number of fins per unit length and defined as follows:

$$N_t=\left(\frac{H}{P_t}-1\right)N, \tag{8}$$

$$N_f=\frac{\frac{W}{F_p}+1}{W}. \tag{9}$$

For the air side, when number of tube rows is greater than one, the Colburn factor (j_a) correlation is suggested by Wang [16]:

$$j_a=0.086Re_{d_c}^{j3}N^{j4}\left(\frac{F_p}{d_c}\right)^{j5}\left(\frac{F_p}{d_h}\right)^{j6}\left(\frac{F_p}{P_t}\right)^{-0.93}, \tag{10}$$

where j_3 to j_6 is calculated by the following formulations:

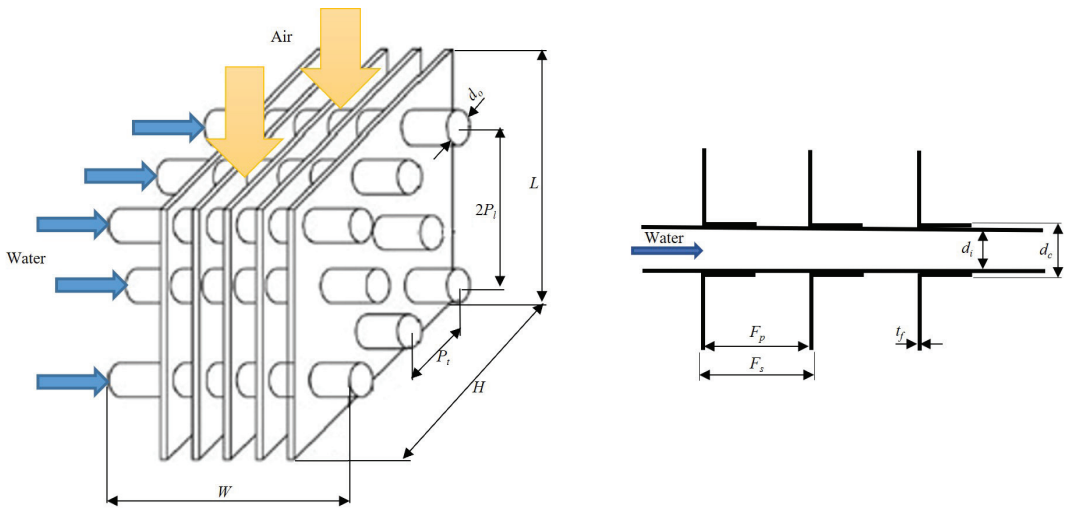

Fig. 1. Fin and tube heat exchanger with cross section view

$$j_3 = -0.361 - \frac{0.042N}{\ln(Re_{dc})} + 0.158\ln\left(N\left(\frac{F_p}{d_c}\right)^{0.41}\right), \quad (11)$$

$$j_4 = -1.224 - \frac{0.076\left(\frac{P_l}{d_h}\right)^{1.42}}{\ln(Re_{dc})}, \quad (12)$$

$$j_5 = -0.083 + \frac{0.058N}{\ln(Re_{dc})}, \quad (13)$$

$$j_6 = -5.735 + 1.21\ln\left(\frac{Re_{dc}}{N}\right), \quad (14)$$

then the heat transfer coefficient on the air side can be achieved by,

$$h_a = j_a \frac{\rho_a \vartheta_a c_{p,a}}{Pr_a^{0.67}}. \quad (15)$$

For the water side, the heat transfer area can be computed by the following relationship:

$$A_i = \pi d_i W N_t. \quad (16)$$

The Nusselt number was approximated through the correlation given by Gnielinski [17]:

$$Nu_w = \frac{\frac{f_w}{8}(Re_w - 1000)Pr_w}{1 + 12.7\left(\frac{f_w}{8}\right)^{1/2}\left(Pr_w^{2/3} - 1\right)}, \quad (17)$$

where f_w is the friction factor and obtained by,

$$f_w = \left(1.82\, log_{10}^{Re_w} - 1.64\right)^{-2}. \quad (18)$$

The heat transfer coefficient on the water side is as follows:

$$h_w = \frac{Nu_w k_w}{d_i}. \quad (19)$$

The basic equation for the design of FTHE is developed in the Eq. (20) [18],

$$Q = UA \cdot T_m = U_o A_o \cdot T_m = U_i A_i \cdot T_m, \quad (20)$$

under dry cooling conditions,

$$\frac{1}{UA} = \frac{1}{\eta_i h_i A_i} + R_{fi} + \frac{ln\left(\frac{d_o}{d_i}\right)}{2\pi k_t W N_t} + R_{fo} + \frac{1}{\eta_o h_o A_o}, \quad (21)$$

where, R_{fi} and R_{fo} are the fouling resistances of inside and outside tubes, respectively, and assumed negligible, η_i and η_o are the fin efficiencies of inside and outside tubes, respectively. The air side fin efficiency is calculated from the modified Schmidt equation that has been proposed by Hong and Webb [19],

$$\eta_f = \frac{\tanh(mr\phi)}{mr\phi} cos(mr\phi), \quad (22)$$

where

$$m = \sqrt{\frac{2h}{t_f k_f}}, \quad (23)$$

$$\phi = \left(\frac{r_{f,eq}}{r} - 1\right)\left(1 + 0.35\ln\left(\frac{r_{f,eq}}{r}\right)\right). \quad (24)$$

For rectangular fins, the equivalent radius is introduced by Schmidt in the following correlation [20],

$$\frac{r_{f,eq}}{r} = 1.28\frac{p_t/2}{r}\left(\sqrt{\frac{P_l}{P_t} - 0.2}\right), \quad (25)$$

where r is the radius of the tube based on the outside tube diameter. Then the air side surface efficiency can be obtained by,

$$\eta_o = 1 - \left(\frac{A_f}{A_O}\right)(1 - \eta_f). \quad (26)$$

Here, the logarithmic mean temperature difference (LMTD) method is applied for heat exchanger analysis.

$$Q = UA \cdot T_{lm}. \quad (27)$$

LMTD is the maximum temperature potential through the heat transfer process that occurs in a counterflow heat exchanger and is described as the following expression:

$$\Delta T_{lm} = \frac{\Delta T_1 - \Delta T_2}{\ln\frac{\Delta T_1}{\Delta T_2}}, \quad (28)$$

where

$$\Delta T_1 = T_{h,i} - T_{c,o}, \quad (29)$$

$$\Delta T_2 = T_{h,o} - T_{c,i}. \quad (30)$$

For a crossflow arrangement, Eq. (27) is modified with a correction factor F_c,

$$Q = UAF_c\Delta T_{lm}. \quad (31)$$

The correction factor F_c is determined from charts or formulas based on two dimensionless parameters: temperature effectiveness P, and the ratio of heat capacity rates, R. Details of calculating these parameters can be found in fundamentals of heat exchanger design [2].

2.2 Pressure Drop

On the air side, the friction factor is obtained from the following correlation given by Wang [16],

$$f_a = 0.0267 Re_{d_c}^{f1}\left(\frac{P_t}{P_l}\right)^{f2}\left(\frac{F_p}{d_c}\right)^{f3}, \quad (32)$$

where

$$f_1 = -0.764 + 0.739\frac{P_t}{P_l} + 0.177\frac{F_p}{d_c} - \frac{0.00758}{N}, \quad (33)$$

$$f_2 = -15.689 + \frac{64.021}{\ln(Re_{dc})}, \quad (34)$$

$$f_3 = 1.696 - \frac{15.695}{\ln(Re_{dc})}, \quad (35)$$

$$Re_{dc} = \frac{G_a d_c}{\mu_a}, \quad (36)$$

where G_a is the mass velocity of air regarding minimum free flow area. Then the pressure drop on air side can be obtained as follows [2]:

$$\Delta p_a = \frac{G_a^2}{2\rho_i}\left[f_a\frac{A}{A_{\min}}\rho_{a,i}\left(\frac{1}{\rho_a}\right)_m + \left(1+\sigma^2\right)\left(\frac{\rho_{a,i}}{\rho_{a,o}} - 1\right)\right],$$
$$\text{s.t.} \quad \left(\frac{1}{\rho_a}\right)_m \neq \frac{1}{\rho_{a,m}} \quad \text{and} \quad \left(\frac{1}{\rho_a}\right)_m = \frac{1}{2}\left(\frac{1}{\rho_i} + \frac{1}{\rho_o}\right). \quad (37)$$

In the above equation, σ is the ratio of $A_{\min}$ to A. Finally, the pressure drop on the water side could be found by the following equation,

$$\Delta P_w = \frac{f_w \rho_w \vartheta_w^2 W}{2 d_i}. \quad (38)$$

3 OBJECTIVE FUNCTIONS AND CONSTRAINTS

Total weight and total annual cost are considered objective functions. Total weight includes weight of fins and weight of tubes,

$$TW = A_f \rho_f t_f + \left(\frac{\pi}{4}\right) N_t \rho_t W \left(d_O^2 - d_i^2\right). \quad (39)$$

Furthermore, total annual cost consists of investment cost and operating cost which are given as:

$$TAC = C_{in} + C_{OP}, \quad (40)$$

$$C_{in} = C_A A^P, \quad (41)$$

$$C_{op} = \left(K_{el} \tau \frac{\Delta P V_t}{\eta}\right)_a + \left(K_{el} \tau \frac{\Delta P V_t}{\eta}\right)_w. \quad (42)$$

The subsequent set of constraints is applied to the mentioned objective functions:

$$\Delta P_a < \Delta P_{a,\max}, \quad (43)$$

$$\Delta P_w < \Delta P_{w,\max}, \quad (44)$$

$$1 < \frac{A}{A_h} < 1.2, \quad (45)$$

$$\frac{W}{d_o} \geq 60, \quad (46)$$

$$300 < Re_a < 2 \times 10^4, \quad (47)$$

$$2300 < Re_w < 2 \times 10^6, \quad (48)$$

where, Re_a and Re_w are Reynolds numbers based on d_c and d_h, respectively. The maximum allowable pressure drops on the air side and water side, respectively, are denoted by $\Delta P_{a,\max}$, and $\Delta P_{w,\max}$.

4 DESIGN METHOD AND PARAMETERS

The steps involved in heat exchanger design based on the LMTD method using a trial-and-error process are as follows [18]:

1. Calculate the outlet temperature according to the heat transfer rate (heat duty) and operating parameters using the steady flow energy equation.
2. Look up the correction factor F_c and calculate LMTD; Eq. (28).
3. Select the size and arrangement of tubes and fins, and calculate the heat transfer area A_{first}; Eq. (5).
4. Calculate the convective heat transfer coefficients of the two sides and then, the overall heat transfer coefficient U; Eqs. (15), (19), and (21).
5. Determine the Calculated heat transfer area A_{cal}; Eq. (20).
6. Compare A_{cal} with A_{first}. If $A_{cal} > A_{first}$, then go back to step 3, until $1 < A_{first}/A_{cal} < 1.2$.
7. Calculate pressure drops and Reynolds numbers on both sides; Eqs. (43), (44), (47), and (48). If they are larger than the allowable pressure drops or are not in valid ranges of Reynolds numbers, then adjust the size and arrangement of tubes and fins until they satisfy specified allowable pressure drops, Reynolds numbers, and step 6.
8. Calculate objective function.

Note that complex factors exist here without consideration and this issue is covered by allowing an additional area of up to 20 %.

The outside tube diameter (d_o), transverse pitch (P_t), longitudinal pitch (P_l), fin pitch (F_p), number of tube rows (N), height of shape (H), and width of shape (W) are assumed as seven design parameters. These parameters and the range of their variations are listed in Table 1 [8]. Shape length, L, is not considered an independent variable, because it can be directly obtained from N and P_l.

Constructional parameters except for the number of tube rows are considered continuous for optimization purposes, however, they are available in discrete quantities. If the precision of design parameters is set to 0.01 (N excluded, which takes values 2, 3, 4, 5, and 6), there are 600, 1000, 1900, 750, 5, 350, and 200 choices for the above tabled variables and therefore $600 \times 1000 \times 1900 \times 750 \times 5 \times 350 \times 200 \approx 10^{17}$ trial-and-error efforts are needed to find the optimal design which is impossible. In the next section, first DE is explained, then we implement DELC and JDELC algorithms instead of a trial-and-error method to attain minimum objective functions in the feasible design space.

Table 1. The upper and lower bounds of design variables

Design variable	Search range
Outside tube diameter, [mm]	7 to 13
Transverse pitch, [mm]	20.5 to 30.5
Longitudinal pitch, [mm]	13 to 32
Fin pitch, [mm]	1 to 8.5
Number of tube rows	2 to 6
Height of shape, [m]	4.5 to 8
Width of shape, [m]	3 to 5

5 DIFFERENTIAL EVOLUTION ALGORITHM

A heuristic called an evolutionary algorithm (EA) was first inspired by biological evolution and employs mechanisms such as mutation, recombination, and selection. In other words, EA evolves an initial population after several generations. Therefore, the use of these algorithms has become popular in solving many problems, including engineering optimizations. In an optimization problem, the candidate vectors represent the individuals of a population.

DE is a simple, yet powerful algorithm proposed by Price et al. [21] and as a metaheuristic seeks to evolve an initial population toward the optimal solutions by iteratively improving them. This algorithm makes a few assumptions about the problem and can quickly reach the best solutions.

5.1 Standard DE

The DE in its standard form has three main parameters: population size NP, mutation factor F, and crossover rate CR. Attaining better solutions and convergence completely depends on the setting of these parameters. To adjust them, a few authors have suggested as following: Price et al. [21] proposed the setting $NP = 10n$, where, n is the number of design parameters, $F \in [0.5, 1]$, and $CR \in [0.8, 1]$. According to Rönkkönen et al. [22], a reasonable choice for population size is between $2n$ and $40n$, $F \in (0.4, 0.95]$, and $CR \in (0, 0.2)$ or $CR \in (0.9, 1)$ for separable and non-separable objective functions, respectively. Note that here objective functions are non-separable. Zielinski et al. [23] reported that, in many cases, the best results are obtained with the setting of $F \geq 0.6$ and $CR \geq 0.6$.

The standard DE includes four principal operations during an optimization problem: 1) initialization 2) mutation 3) crossover 4) selection. The general structure of the algorithm is shown in Fig. 2.

5.1.1 Initialization

In a problem with n design variable, each candidate vector is defined as $X = (x_1, x_1, \ldots, x_n)$. The purpose is to optimize objective function

$f(X)$. In the beginning, an initial population is generated including vectors as many as NP. Each member of the initial population is generated from Eq. (49). As a result, the initial population is an NP by n matrix.

$$x_{i,j} = x_{j(\min)} + rand(0,1) \times \left(x_{j(\max)} - x_{j(\min)} \right), \quad i = 1,2,\ldots,NP \quad \text{and} \quad j = 1,2,\ldots,n, \tag{49}$$

where, $x_{j(\max)}$ and $x_{j(\min)}$ are the maximum and minimum values of each design variable, respectively. Furthermore, $rand(0,1)$ is a uniformly distributed random number between 0 and 1.

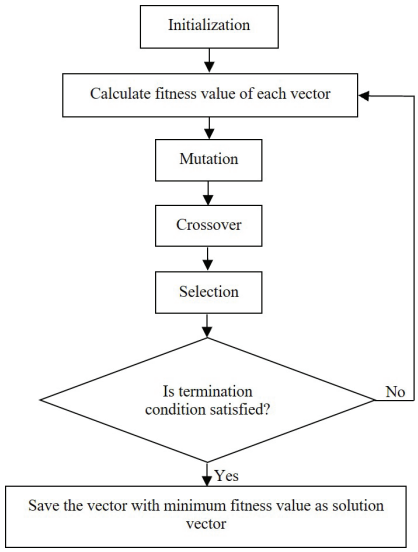

Fig. 2. Flowchart of standard DE algorithm

5.1.2 Mutation

In this step, a noisy population (donor vectors) is produced from the initial population as follows: for each vector from the current population, i^{th}, the mutated vector is obtained by combining three randomly selected vectors according to the formulation below:

$$\mathbf{M}_i = \left(m_{i,1},\ldots,m_{i,n} \right) = \mathbf{X}_c + F \times \left(\mathbf{X}_a - \mathbf{X}_b \right), \tag{50}$$

where, $\mathbf{X}_a$, $\mathbf{X}_b$, and $\mathbf{X}_c$ are three random vectors in the current population between 1 and NP except i^{th}. The mutation factor, F, is a positive real number that controls the rate at which the population evolves. F has no upper bound, however effective values are rarely larger than 1 [21]. This mutation step is replicated for all original vectors of the current population to produce new population members that would improve the search space. This strategy, named DE/rand/1, is the most popular and simplest DE variant, which uses one difference as a perturbation of the base vector. There are many other variants of the mutation mechanism that have been subsequently proposed by Das et al. [10] and Price et al. [21], such as DE/rand/2, DE/best/1, DE/best/2, etc. [24].

5.1.3 Crossover

After mutation, the i^{th} original vector from the current population is recombined with the corresponding vector from the mutated population to produce the trial vector $\mathbf{U}_i = (u_{i,1}, \ldots, u_{i,n})$. Each element of the trial vector is determined based on the following equation:

$$u_{i,j} = \begin{cases} m_{i,j} & \text{if } rand(0,1) < CR \text{ or } j = R \\ x_{i,j} & \text{otherwise} \end{cases}, \tag{51}$$

where CR is between 0 and 1 which represents the probability of selecting a trial vector from the original vector and mutated vector, and R is a random integer number between 1 and n.

5.1.4 Selection

As the last step, just one of the vectors, $\mathbf{X}_i$ (original) and $\mathbf{U}_i$ (crossed) can survive. This selection is done based on the type of problem as follows:

1. for an unconstrained problem, objective function values of the two above vectors are the comparison criteria. If the goal is a minimization problem, the vector with a lower objective function value will be selected, and vice versa. Eq. (52) represents the selection step due to the minimization of an objective function. The following process is repeated for a certain number of generations or until convergence criteria are satisfied.

$$\mathbf{X}_i^{t+1} = \begin{cases} \mathbf{U}_i^t & \text{if} \quad f\left(\mathbf{U}_i^t\right) < f\left(\mathbf{X}_i^t\right) \\ \mathbf{X}_i^t & \text{otherwise} \end{cases}. \tag{52}$$

2. If the problem is constrained, like the present case, in addition to checking the objective function, the constraints' fitness should also be checked.

In the next section, we apply α-level comparison to handle the optimization problem constraints.

5.2 Differential Evolution with Level Comparison

The canonical versions of EAs, including DE, lack a mechanism to bias the search to the most feasible area since they were not designed inherently to solve constrained optimization problems [25]. Hence, this has triggered a significant amount of investigation, and during the last years, many different methods for incorporating constraints into the fitness function of an EA have been proposed [26]. Practically, adjusting control parameters such as F and CR and coupling them with suitable and effective constraint-handling strategies can considerably enhance the search capability of DE algorithms. Differential evolution with level comparison (DELC) performs initialization, mutation, and crossover operations similar to standard DE, but besides objective function values, a satisfaction level for the constraints is considered, which indicates how well a search point (candidate vector) satisfies the constraints. In other words, this method quantifies the constraint violation [27].

Below, $f(\mathbf{X})$ is assumed to be a general function that should be minimized by the inequality constraints set $g_k(\mathbf{X})$ with $k = 1,\ldots,p$, and equality constraints set $h_s(\mathbf{X})$ with $s = 1,\ldots,q$.

$$\min_{\mathbf{X}} f\left(\mathbf{X}\right) \quad \text{s.t.} \quad g_k\left(\mathbf{X}\right) \le 0; \quad k = 1,2,\ldots,p; \quad h_s\left(\mathbf{X}\right) = 0; \quad s = 1,2,\ldots,q. \tag{53}$$

From the first generation ($t=1$) to the end ($t=Gen_{\max}$), the selection between each original vector ($\mathbf{X}_i$) and its trial ($\mathbf{U}_i$) from the current population, will be done regarding DELC. Also, f_1 and f_2 are the objective function values of the mentioned vectors, respectively, and μ_1 and μ_2 are their related satisfaction levels. For instance, the resulting satisfaction level of vector $\mathbf{X}_i$ is determined by,

$$\mu_1 = \mu\left(\mathbf{X}_i\right) = \min_{k,s}\left\{ \mu_{g_k}\left(\mathbf{X}_i\right), \mu_{h_s}\left(\mathbf{X}_i\right) \right\}, \tag{54}$$

where all constraints are calculated from piecewise linear functions as follows:

$$\mu_{g_k}\left(\mathbf{X}_i\right) = \begin{cases} 1 & \text{if} \quad g_k\left(\mathbf{X}_i\right) \le 0 \\ 1 - \dfrac{g_k\left(\mathbf{X}_i\right)}{b_k} & \text{if} \quad 0 \le g_k\left(\mathbf{X}_i\right) \le b_k \\ 0 & \text{otherwise} \end{cases}, \tag{55}$$

$$\mu_{h_s}(\mathbf{X}_i)=\begin{cases}1-\dfrac{|\mathbf{h}_s(\mathbf{X}_i)|}{b_s} & \text{if} \quad |h_s(\mathbf{X}_i)|\le b_s,\\ 0 & \text{otherwise}\end{cases} \tag{56}$$

where b_k and b_s are two positive numbers. In this study, the median values of the constraint violations in the initial population are employed and these parameters are updated after each generation.

Here, the selection between two sets of ($f(\mathbf{X}_i)$, $\mu(\mathbf{X}_i)$) and ($f(\mathbf{U}_i)$, $\mu(\mathbf{U}_i)$) based on DELC with α satisfaction level is according to:

$$\mathbf{X}_i^{t+1}=\begin{cases}\mathbf{U}_i^t & \left(f(\mathbf{U}_i^t),\mu(\mathbf{U}_i^t)\right)\le_\alpha\left(f(\mathbf{X}_i^t),\mu(\mathbf{X}_i^t)\right)\\ \mathbf{X}_i^t & \text{else}\end{cases}. \tag{57}$$

The α-level comparison $<\alpha$ and $\le\alpha$ between ($f(\mathbf{X}_i)$, $\mu(\mathbf{X}_i)$) = (f_1, μ_1) and ($f(\mathbf{U}_i)$, $\mu(\mathbf{U}_i)$) = (f_2, μ_2) are defined in this way:

$$(f_1,\mu_1)\le_\alpha(f_2,\mu_2)\Leftrightarrow\begin{cases}f_1\le f_2 & \mu_1,\mu_2\ge\alpha\\ f_1\le f_2 & \text{if} \quad \mu_1=\mu_2\\ \mu_1\ge\mu_2 & \text{otherwise}\end{cases}, \tag{58}$$

It means that due to $\le\alpha$ comparison, (f_1, μ_1) is a better individual compared to (f_2, μ_2) when $f_1\le f_2$ (in case of μ_1, $\mu_2\ge\alpha$ or $\mu_1=\mu_2$) or $\mu_1\ge\mu_2$. Similar consequences can be pointed for $<\alpha$ comparison. Fig. 3 depicts the detailed implementation of the DELC algorithm. For those problems subjected to strong equality constraints, the α-level should be controlled to obtain high quality results. However, in this study, the α-level does not need to be controlled and like many constrained problems, can be solved when α is constantly 1 [27].

5.3 JDE

A standard DE algorithm contains a set of parameters that are remained constant throughout the optimization process. In order to achieve optimal performance, the tuning of these parameters for each optimization problem is necessary. Some researchers claim that manually setting the DE inputs is not too difficult [21]. However, some argue that this process may be effortful, especially for certain optimization problems [28]. The setting of the control parameters greatly affects the efficiency, effectiveness, and robustness of the DE algorithm. Hence, best parameter selection is a problem-specific question, because some may work well for some problems but not for others [29]. JDE has self-adaptive control parameter settings and shows acceptable performance in benchmark problems. JDE operates in such a way that uses a self-adaptive approach to adjust F and CR parameters for the best optimization results. The control parameters for JDE algorithm are:

$$F_i^{t+1}=\begin{cases}F_l+rand_1F_u, & \text{if} \quad rand_2<\tau_1\\ F_i^t, & \text{otherwise}\end{cases}, \tag{60}$$

$$CR_i^{t+1}=\begin{cases}rand_3, & \text{if} \quad rand_4<\tau_2\\ CR_i^t, & \text{otherwise}\end{cases}. \tag{61}$$

$rand_j$ with $j\in\{1,2,3,4\}$ are uniformly distributed random numbers between 0 and 1 and τ_1 and τ_2 represent probabilities to set factors F and CR where $\tau_1=\tau_2=0.1$ is recommended, while $F_l=0.1$ and $F_u=0.9$, therefore the new range for F value will be [0.1, 1] [30].

As well as DELC, we use JDE with level comparison (JDELC) to obtain optimal structural parameters associated with an FTHE. Note that JDELC has a similar procedure to Fig. 3, except that it does not need to guess good values of F and CR in the initialization step and it has a self-adaption nature. The task of thermal design and optimization by DELC and JDELC algorithms is conducted in the Fortran programming language.

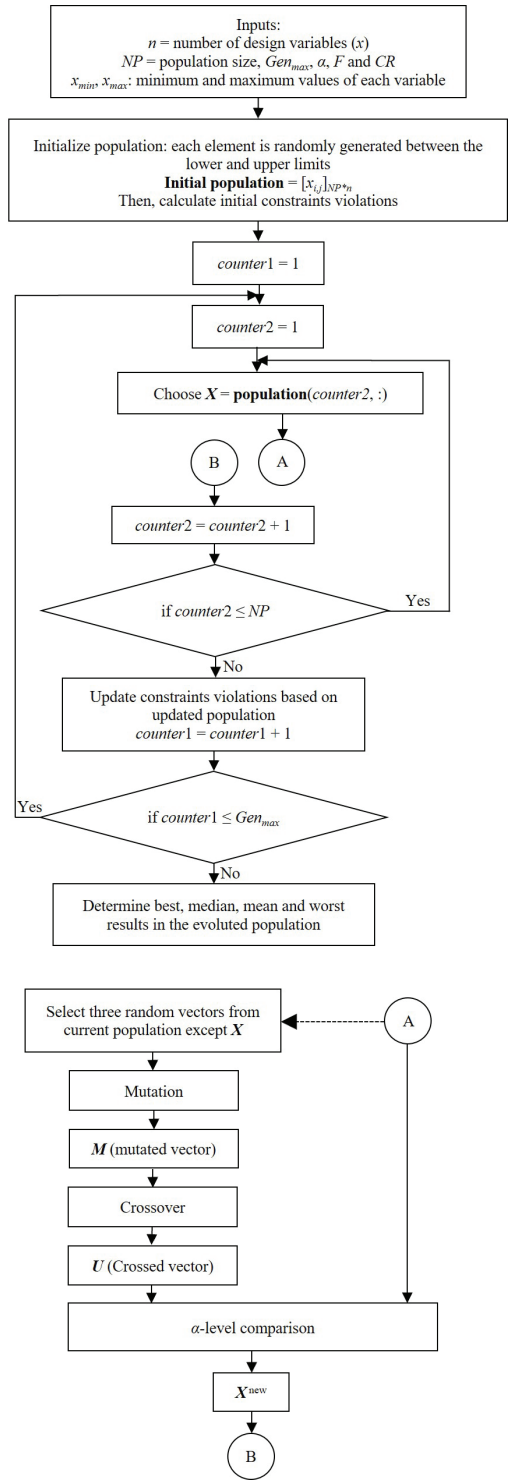

Fig. 3. Flowchart of DELC

6 A CASE STUDY AND RESULTS

To demonstrate the described procedure, a case study is considered and the effectiveness of the proposed algorithm is assessed by analyzing an application example that was earlier investigated by GA [8] and HTS [9]. The model of FTHE is cross-flow and both fluids are unmixed. The material of the tubes is stainless steel with a thermal conductivity of 15 W/(m·K) and a density of 7820 kg/m³, while the fin material is aluminum with a thermal conductivity of

170 W/(m·K) and a density of 2790 kg/m³. Tables 2 and 3 show operating conditions and cost function constants, respectively.

Table 2. Operating parameters

Variable	Water side	Air side
Flow rate, [kg/s]	39.2	58.2
Inlet temperature, [°C]	20	104
Outlet temperature, [°C]		51
Inlet pressure, [kPa]	174.5	174.5
Allowable pressure drop, [Pa]	5200	5200
Heat duty, [kW]	3115	3115

Table 3. Economic constants

Variable	Value	Variable	Value
Cost per unit area, [$/m²]	100	Electricity price, [$/MWh]	30
Exponent for area	0.6	Pump efficiency	0.5
Hour of operation, [h/year]	6500		

For consistent comparison with previous works, air side, and water side allowable pressure drops are considered as 30 Pa and 4500 Pa, respectively. Also, the thermophysical properties of the fluids have been shown in Table 4. The subscript *t, m* returns to the mean temperature value.

Table 4. Thermophysical properties

Fluid	Air	Water
$T_m = (T_1+T_2)/2$, [°C]	77.5	29.5
ρ_i, [kg/m³]	1.612	-
ρ_o, [kg/m³]	1.875	-
$\rho_{t,m}$, [kg/m³]	1.734	995.8
$\rho_{ave} = (\rho_i+\rho_o)/2$, [kg/m³]	1.7435	-
$\mu_{t,m}$, [Pa·s]	0.00002085	0.0008059
$Cp_{t,m}$, [J/(kgK)]	1008	4180
$Pr_{t,m}$	0.7162	5.489
$k_{t,m}$, [W/(mK)]	-	0.6137
$\Delta T_1 = T_{h,i} - T_{c,o} = 104 - 39 = 65$ [°C]		
$\Delta T_2 = T_{h,o} - T_{c,i} = 51 - 20 = 31$ [°C]		
$\Delta T_{lm} = (\Delta T_1 - \Delta T_2) / (\ln(\Delta T_1/\Delta T_2)) = 45.916$ [°C]		
$F_c = 0.946$		

6.1 Minimum Weight Optimization

Table 5, reports the statistical results for total weight minimization, including the best, median, mean, worst, and SD. The optimum results are marked with boldface.

Table 5. Algorithms' statistical results for total weight optimization

$G_{max} = 500$, $NP = 70$, and $\alpha = 1$						
	F	Best	Median	Mean	Worst	SD
DELC $CR = 0.9$	0.2	1080.00	1206.5	1206.5	1464.11	1.27e2
	0.4	**1013.17**	**1013.17**	1014.97	1041.77	5.9855
	0.6	**1013.17**	**1013.17**	**1013.17**	**1013.17**	**1.16e-16**
	0.8	**1013.17**	1015.02	1015.40	1019.14	1.5978
	1	**1013.17**	1014.62	1017.11	1039.78	5.9981
	1.2	1026.69	1055.82	1056.01	1089.65	16.668
JDELC: $\tau_1 = \tau_2 = 0.1$, $F_l = 0.1$, $F_u = 0.9$	F (Eq. (60)) CR (Eq. (61))	1013.17	1013.17	1013.31	1016.5	0.665

Table 6. Design results for minimum total weight consideration compared to GA [8] and HTS [9]

	GA	HTS	DE
Outside diameter, [mm]	12.63	11.9	10.72
Transverse pitch, [mm]	28.94	30.8	20.5
Longitudinal pitch, [mm]	27.26	30.7	14.89
Fin pitch, [mm]	1.23	1.2	1
Height of shape, [m]	7.29	7.79	8
Width of shape, [m]	4.08	3	3.39
Length of shape, [m]	0.0545	0.0614	0.0298
Number of tubes	502	504	779
Number of fins	3318	2501	3391
Number of tube rows	2	2	2
Fin thickness, [mm]	0.12	0.12	0.12
Volume, [m³]	1.62	1.43	0.81
Heat transfer area, [m²]	2294.48	2165.3	1222.59
Pressure drop on air side, [Pa]	30	30	30
Pressure drop on water side, [Pa]	4464	4495.1	4471.96
Total annual cost, [$/year]	10873.7	10523	7580.1
Weight of tubes, [kg]	584.66	406.45	630.61
Weight of fins, [kg]	750.42	711.65	383.12
Total weight, [kg]	1335.08	1118.1	1013.73

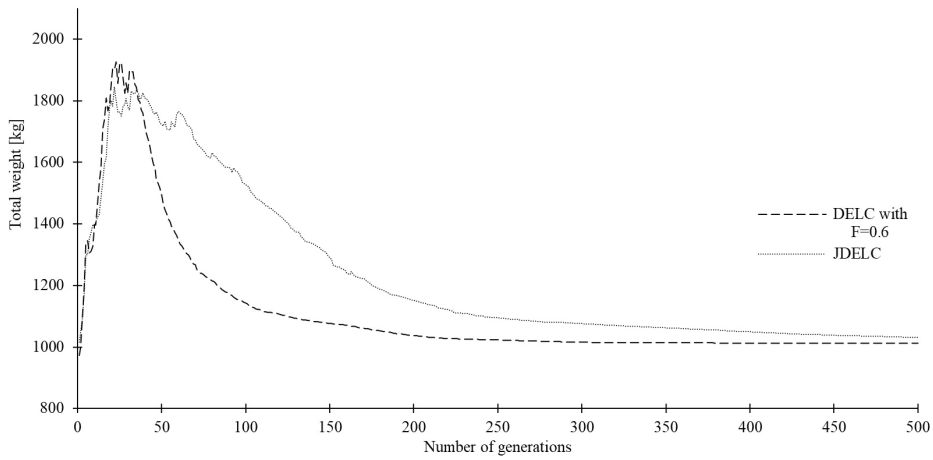

Fig. 4. Algorithms' convergence performance for total weight minimization

From the results provided in Table 5, it is observed that DELC with $F = 0.4$, 0.6, 0.8, and 1 and JDELC obtain the finest solution at least once, but only DELC with $F = 0.6$ and JDELC have a minimum of the median, mean, and worst. Moreover, the SD of these two cases is the lowest. So, these concluded as the best schemes. Fig. 4 demonstrates the evolution process related to total weight optimization. As seen from Fig. 4, DELC with $F = 0.6$ converges considerably earlier. Also, after about 150 generations, there are very slight variations in individuals, and finally, an acceptable level of optimal weight is reached. As a result, DELC with $F = 0.6$ provides better performance than others and has been chosen as the best manner.

Table 6 shows DELC algorithm's optimum solution for minimum total weight and those obtained by the GA and HTS algorithms previously. When compared to the results of the HTS algorithm, which were reported before as the best in terms of total weight, a significant decrease (33.4 %) in transverse pitch leads obviously to an enormous increase (54.6 %) in the number of tubes and, consequently, the weight of tubes increases by 55.2 %. The number of fins increases (35.6 %) due to the rise in width of shape (13 %) and decrease in fin pitch (16.7 %). Despite an increase in the number of fins, a significant decrease in the length of shape (51.5 %) besides an increase in the number of tubes (As confirmed by Eqs. (5) and (7), resulted in a noticeable decrease (43.5 %) in the heat transfer area, and so weight of fins decreases by 46.2 %.

Overall, the combined effect of changes in the weight of tubes and fins results in a reduction of total weight of about 24.07 % and 9.33 % employing DE as compared to GA and HTS, respectively.

6.2 Minimum Cost Optimization

Like the first objective function, shown in Table 5, outcomes for total annual cost optimization are calculated and listed in Table 7. Similarly, the optimal cases are mentioned in boldface.

From the results presented in Table 7, five items achieve the elite solution, but the median, mean, and worst are minimum for DELC only with $F = 0.6$ and $F = 0.8$ besides the SD of both choices is too small. Again, DELC with $F = 0.6$ has a higher speed of convergence compared to the other as illustrated in Fig. 5. Furthermore, the number of generations needed to gain a good approximation is about 150. It may make sense that convergence curves have considerable overshoot in both weight and cost optimizations, as shown in Figs. 4 and 5, however, it has been observed that the behavior is significantly influenced by design variable N. The optimum solution found by the DELC algorithm for minimum total annual cost is gathered in Table 8.

Table 7. Algorithms' statistical results for total annual cost optimization

$G_{max} = 500$, $NP = 70$, and $\alpha = 1$						
	F	Best	Median	Mean	Worst	SD
DELC $CR = 0.9$	0.2	6778.76	7377.44	7491.69	8605.47	508.364
	0.4	**6286.38**	6287.96	6484.78	7002.65	261.387
	0.6	**6286.38**	**6286.38**	**6286.38**	**6286.38**	**1.85e-12**
	0.8	**6286.38**	**6286.38**	6286.39	6286.68	**0.05968**
	1	**6286.38**	**6286.38**	6288.43	6298.81	3.86347
	1.2	6333.65	6403.27	6396.35	6462.06	37.4456
JDELC: $\tau_1 = \tau_2 = 0.1$, $F_l = 0.1$, $F_u = 0.9$	F (Eq. (60)) CR (Eq. (61))	**6286.38**	**6286.38**	6286.58	6291.36	0.996

Table 8. Design results for minimum total annual cost consideration compared to GA [8] and HTS [9]

	GA	HTS	DE
Outside diameter, [mm]	13	13	13
Transverse pitch, [mm]	21.78	20.4	20.5
Longitudinal pitch, [mm]	27.26	24.6	16.89
Fin pitch, [mm]	2.87	2.37	1.5
Height of shape, [m]	7.59	5.8	5.54
Width of shape, [m]	4.95	5	5
Length of shape, [m]	0.0545	0.0492	0.03378
Number of tubes	454	567	539
Number of fins	2645	2111	3335
Number of tube rows	2	2	2
Fin thickness, [mm]	0.12	0.12	0.12
Volume, [m^3]	2.05	1.43	0.9357
Heat transfer area, [m^2]	1114.45	989.37	876.73
Pressure drop on air side, [Pa]	30	29.14	30
Pressure drop on water side, [Pa]	2654	1856.9	4151.17
Total weight, [kg]	1388.52	1137.46	1054.13
Capital cost, [$/year]	6733.4	6269.2	5830.69
Operating cost, [$/year]	689.1	483.6	457.97
Total annual cost, [$/year]	7422.5	6752.8	6288.66

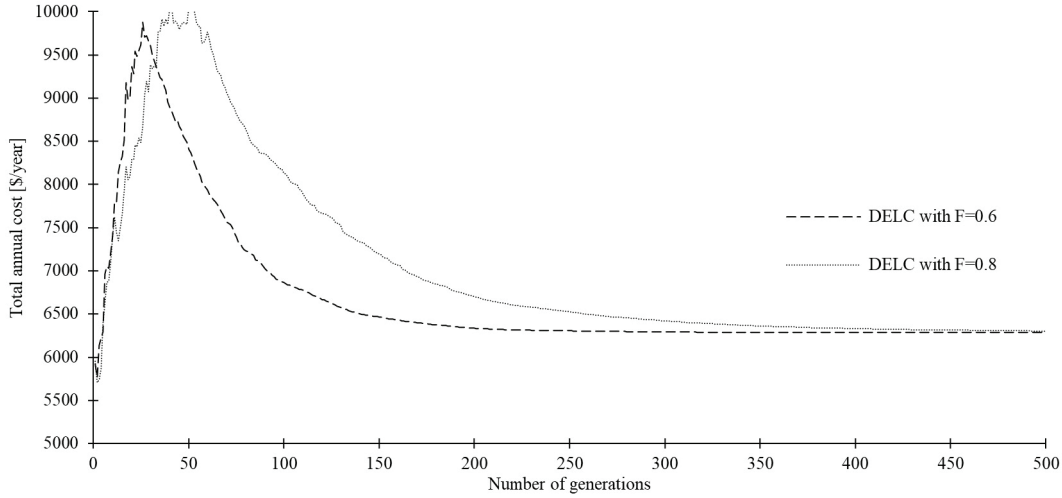

Fig. 5. Algorithms' convergence performance for total annual cost minimization

As before, when comparing the optimum solution obtained by the DELC method to HTS findings, as the best result for total annual cost, while the width of shape remains constant, a remarkable increase (58 %) in the number of fins occurred by a large decrease (36.7 %) in fin pitch. Despite an increase in the number of fins, a noticeable decrease (31.3 %) in the length of shape has resulted in a significant decrease (11.4 %) in the heat transfer area (As expected from Eqs. (5) and (7)) and a considerable decrease in capital cost by 7 %. Furthermore, an increase in transverse pitch and a decrease in height of shape reduce the number of tubes by 4.9 % and operating cost by 5.3 %. As a result, when compared to GA and HTS, the DELC algorithm saves 15.28 % and 6.87 % of the total annual cost, respectively. It is important to mention that the design variables are rounded in Tables 6 and 8 and the objective functions are calculated accordingly.

The achievements for both objective functions show that the DE algorithm with α-level constraint control, provides significant improvements in optimal designs by finding the desirable variables with satisfied constraints, compared to GA and HTS.

7 PARAMETRIC ANALYSIS

In this section, sensitivity analysis is used to determine how objective functions are affected based on changes in structural parameters and to indicate the feasible design space. For this purpose, each variable is changed within the predefined ranges, while others are kept constant at their optimum obtained by DE. Figs. 6 and 7 show the influence of variation of outside tube diameter, transverse pitch, longitudinal pitch, fin pitch, number of tube rows, height of shape, and width of shape on total weight. In these figures, only areas shown with symbols are feasible.

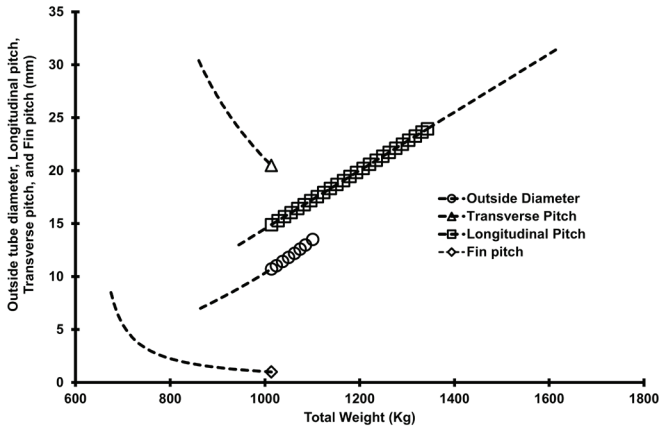

Fig. 6. Effect of outside tube diameter, transverse pitch, longitudinal pitch, and fin pitch on total weight

As seen from these figures, increases in the outside tube diameter, longitudinal pitch, number of tube rows, height of shape, and width of shape lead to a linear increment in the total weight of the heat exchanger, furthermore, as expected when transverse pitch and fin pitch increase, the mentioned objective function values decrease. Figures show that parametric optimization results agree with the solutions acquired by DE algorithm because total weight is optimum when transverse pitch and fin pitch are minimum and height of shape is maximum. Accordingly, the optimum solution occurs when there are two rows of tubes and the outside tube diameter, longitudinal pitch, and width of shape are equal to 10.72 mm, 14.89 mm, and 3.39 m, respectively. Moreover, the feasible space for the design parameters; outside tube diameter, longitudinal pitch, and width of shape is obtained in this way: 10.72 mm to 13.5 mm, 14.89 mm to 23.95 mm, and 3.39 mm to 3.41 m. Beyond this range, constraint violation happens. As a result of parametric analysis, 24.45 % of the solutions are practicable around the obtained optimal point. Similarly, Figs. 8 and 9 illustrate the variation of those parameters in the solution space for the total annual cost objective function.

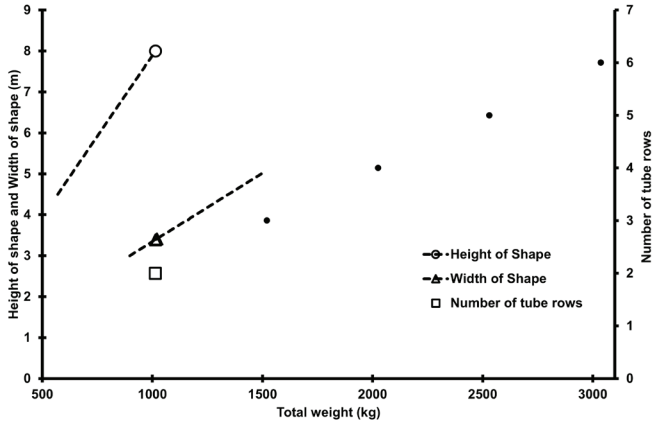

Fig. 7. Effect of height of shape, width of shape, and number of tube rows on total weight

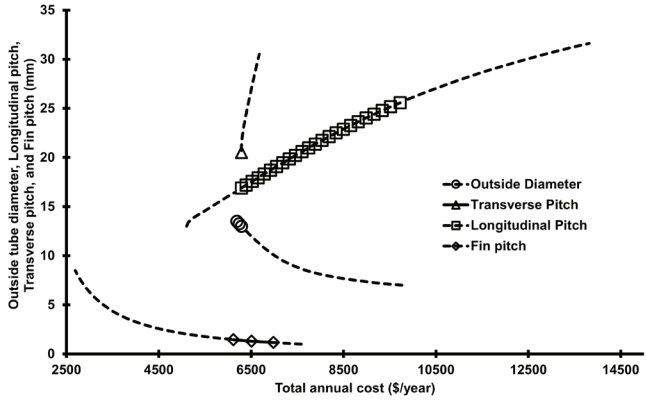

Fig. 8. Effect of outside tube diameter, transverse pitch, longitudinal pitch, and fin pitch on total annual cost

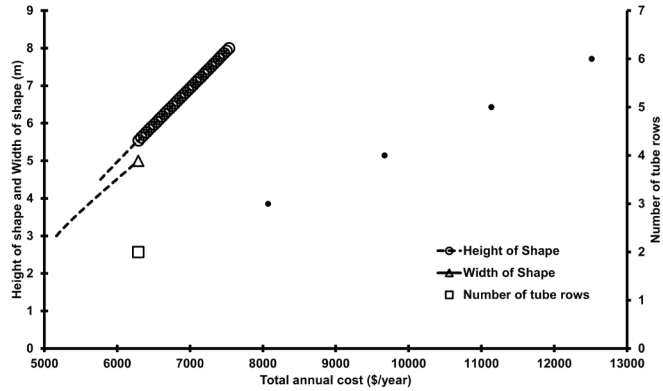

Fig. 9. Effect of height of shape, width of shape, and number of tube rows on total annual cost

The above figures indicate that an increase in the outside tube diameter and fin pitch leads to a decrease in the total annual cost of the heat exchanger, primarily due to the reduction in pressure drop, which subsequently lowers the operation cost. However, increases in transverse pitch, longitudinal pitch, number of tube rows, as well as the height and width of the shape, result in a higher total annual cost. This cost is optimal when the outside tube diameter, transverse pitch,

and width of shape are at their maximum (13 mm), minimum (20.5 mm), and maximum (5 m), respectively. Also, the optimum solution is obtained where the longitudinal pitch, number of tube rows and height of shape are equal to 16.89 mm, 2 m and 5.54 m, respectively. In addition, as shown, those parameters are feasible for outside tube diameter, longitudinal pitch, fin pitch and height of shape which are within 13 to 13.5 mm, 16.89 mm to 25.57 mm, 1.17 mm to 1.5 mm, and 5.54 m to 8 m, respectively. It should be noted that an outside tube diameter between 7 mm and 13 mm is selected as the search range in the DE routine, but up to 13.5 mm is in the valid range [16], and used in the parametric analysis. A violation of the constraint occurs outside of these ranges. As a whole, 24.68 % of the space in total annual cost parametric analysis is applicable.

8 CONCLUSION

In this paper, the DE algorithm and JDE as a variant of standard DE are successfully implemented in the thermal design of a plain fin and tube heat exchanger based on the minimization of the total weight and total annual cost as two individual objective functions. For this purpose, the α-level constraint-handling method is incorporated into the global search capability of DE. Improvements in the results are observed for both objective functions with those reported by GA and HTS approaches previously. Finally, 24.07 % and 9.33 % reduction in total weight, and 15.28 % and 6.87 % in total annual cost are achieved using the DELC algorithm as compared to the two mentioned procedures. Consequently, applying the DELC algorithm to optimize FTHEs could give better results than the others. The performance of the gas side in the present FTHE may be improved by replacing continuous plain fins with high-performance fins, i.e., strip fins, slit fins, and louver fins. Furthermore, this study can be extended to the optimization of other types of heat exchangers for different goals in future work.

NOMENCLATURES

A initial heat transfer area, [m^2]
A_h heat transfer area based on overall heat transfer coefficient, [m^2]
A_i water side heat transfer area, [m^2]
$A_{\min}$ minimum free flow area, [m^2]
A_o air side heat transfer area, [m^2]
CR crossover rate,
C_A price per unit area, [\$/m^2]
C_{in} annual cost of investment, [\$/year]
C_{op} annual cost of operation, [\$/year]
C_p specific heat at constant pressure, [J/(kgK)]
d_c fin collar outside diameter, [mm]
d_h hydraulic diameter, [mm]
d_i inside tube diameter, [mm]
d_o outside tube diameter, [mm]
f friction factor,
F mutation factor,
F_c correction factor,
F_p fin pitch, [mm]
F_s fin space, [mm]
H height of shape, [m]
k thermal conductivity, [W/(m^{2}K)]
N_f number of fins per unit length,
NP population size,
N_t number of tubes,
Nu Nusselt number,
m fin parameter defined by Eq. (23),
n number of design variables,
p exponent of area,
P_l longitudinal tube pitch, [mm]
Pr Prandtl number,
P_t transverse tube pitch, [mm]
R radius of tube based on d_o, [mm]
$r_{f,eq}$ equivalent circular fin radius, [mm]
Re Reynolds number based on d_h,
Re_{dc} Reynolds number based on d_c,
R_{fi} internal fouling resistance, [m^{2}K/W]
R_{fo} external fouling resistance, [m^{2}K/W]
t_f fin thickness, [mm]
TAC total annual cost, [\$/year]
TW total weight, [kg]
U overall heat transfer coefficient, [W/(m^{2}K)]
V volumetric flow rate, [m^3/s]
W width of shape, [m]
x design variable,
$\mathbf{X}$ vector of design variables

Greek letters

η pump and compressor efficiencies,
η_f fin efficiency,
η_i internal surface efficiency,
η_o external surface efficiency,
υ minimum flow velocity, [m/s]
μ fluid dynamic viscosity, [Pa·s]
σ contraction ratio of cross-sectional area,
ρ density, [kg/m^3]
τ hours of operation per year, [hours/year]
ΔP pressure drop, [Pa]
ΔT_m mean temperature difference, [K]
ΔT_{lm} logarithmic mean temperature difference, [K]
ϕ parameter defined by Eq. (24)

Subscripts

a air side
c cold side
f fin
h hot side
i inlet
m mean
min minimum
max maximum
o outlet
t tube
w water side

REFERENCES

[1] Bergman, T.L., Lavine, A.S., Incropera, F.P., DeWitt, D.P. *Fundamentals of Heat and Mass Transfer*, 8th Edition. John Wiley & Sons (2018) New York.

[2] Shah, R.K., Sekulic, D.P. *Fundamentals of Heat Exchanger Design*. John Wiley & Sons (2003) New York **DOI: 10.1002/9780470172605**

[3] Castro Gómez, L., Manuel Velázquez Flores, V., Navarrete Procopio, M. Kharaji, S, *Heat exchangers design and optimization*. Intechopen (2022), chapter 7 **DOI:10.5772/intechopen.100450**

[4] Rao, R.V., Patel, V.K. Thermodynamic optimization of cross flow plate-fin heat exchanger using a particle swarm optimization algorithm. *Int J Therm Sci* 49, 1712-1721 (2010) **DOI:10.1016/j.ijthermalsci.2010.04.001**

[5] Ahmadi, P., Hajabdollahi, H., Dincer, I. Cost and entropy generation minimization of a cross-flow plate fin heat exchanger using multi-objective genetic algorithm. *ASME J Heat Mass Tran* 133, 02180 (2011) **DOI: 10.1115/1.4002599**

[6] Wang, Z., Li, Y. Irreversibility analysis for optimization design of plate fin heat exchangers using a multi-objective cuckoo search algorithm. *Energ Convers Manage* 101, 126-135 (2015) **DOI:10.1016/j.enconman.2015.05.009**

[7] Hajabdollahi, H. Investigating the effect of non-similar fins in thermoeconomic optimization of plate fin heat exchanger. *Appl Therm Eng* 82, 152-161 (2015) **DOI:10.1016/j.applthermaleng.2014.12.077**

[8] Xie, G., Wang, Q., Sunden, B. Application of a genetic algorithm for thermal design of fin-and-tube heat exchangers. *Heat Transfer Eng* 29, 597-607 (2008) **DOI:10.1080/01457630801922337**

[9] Raja, B.D., Patel, V., Jhala, R.L. Thermal design and optimization of fin-and-tube heat exchanger using heat transfer search algorithm. *Therm Sci Eng Progr* 4, 45-57 (2017) **DOI:10.1016/j.tsep.2017.08.004**

[10] Das, S., Suganthan, P.N. Differential evolution: A survey of the state-of-the-art. *IEEE T Evolut Comput* 15, 4-31 (2011) **DOI:10.1109/TEVC.2010.2059031**

[11] Babu, B.V., Munawar, S.A. Differential evolution strategies for optimal design of shell-and-tube heat exchangers. *Chem Eng Sci* 62, 3720-3739 (2007) **DOI:10.1016/j.ces.2007.03.039**

[12] Ayala, H.V.H., Keller, P., Morais, M. de F., Mariani, V.C., Coelho, L.D.S., Rao, R.V.Design of heat exchangers using a novel multi objective free search differential evolution paradigm. *Appl Therm Eng* 94, 170-177 (2016) **DOI:10.1016/j.applthermaleng.2015.10.066**

[13] Segundo, E.H.D.V., Amoroso, A.L., Mariani, V.C., Coelho, L.D.S. Economic optimization design for shell-and-tube heat exchangers by a Tsallis differential evolution. *Appl Therm Eng* 111, 143-151 (2017) **DOI:10.1016/j.applthermaleng.2016.09.032**

[14] Yuan, Y., Cao, J., Wang, X., Zhang, Z., Lio, Y. Economic-effectiveness analysis of micro-fins helically coiled tube heat exchanger and optimization based on multi objective differential evolution algorithm. *Appl Therm Eng* 201, 117764 (2022) **DOI:10.1016/j.applthermaleng.2021.117764**

[15] Wang, L., Li, L.P. An effective differential evolution with level comparison for constrained engineering design. *Struc Multidiscip O* 41, 947-963 (2010) **DOI:10.1007/s00158-009-0454-5**

[16] Wang, C.C. Recent progress on the air-side performance of fin and tube heat exchangers. *Int J Heat Exch* 1, 57-84 (2000)

[17] Gnielinski, V. New equations for heat and mass transfer in turbulent pipe and channel flow. *Int Chem Eng* 16, 359-367 (1976)

[18] Xie, G.N., Chen, Q.Y., Zeng M., Wang, Q.W. Thermal design of heat exchanger with fins inside and outside tubes. *Proceedings of the ASME Turbo Expo 2006: Power for Land, Sea, and Air ASME Turbo Expo 2006: Power for Land, Sea, and Air* (2006) p. 263-268 **DOI:10.1115/GT2006-90260**

[19] Hong, K.T., Webb, R.L. Calculation of fin efficiency for wet and dry fins. *HVAC&R Res* 2, 27-41 (1996) **DOI:10.1080/10789669.1996.10391331**

[20] Schmidt, T.E. Heat transfer calculation for extended surfaces. *Refr Eng* 57, 351-357 (1949)

[21] Price, K.V., Storn, R.M., Lampinen, J.A. *Differential Evolution: A Practical Approach to Global Optimization*. Springer (2005) Berlin, Heidelberg **DOI:10.1007/3-540-31306-0_2**

[22] Ronkkonen, J., Kukkonen, S., Price, K.V. Real-parameter optimization with differential evolution. *IEEE Congress on Evolutionary Computation* (2005) p. 506-513 **DOI:10.1109/CEC.2005.1554725**

[23] Zielinski, K., Weitkemper, P., Laur, R., Kammeyer, K.D. Parameter study for differential evolution using a power allocation problem including interference cancellation. *IEEE International Conference on Evolutionary Computation* (2006) p. 1857-1864 **DOI:10.1109/CEC.2006.1688533**

[24] Neri, F., Tirronen, V. Recent advances in differential evolution: a survey and experimental analysis. *Artif Intell Rev* 33, 61-106 (2010) **DOI:10.1007/s10462-009-9137-2**

[25] Michalewicz, Z., Schoenauer, M. Evolutionary algorithms for constrained parameter optimization problems. *Evol Comput* 4, 1-32 (1996) **DOI:10.1162/evco.1996.4.1.1**

[26] Coello, C.A.C. Theoretical and numerical constraint-handling techniques used with evolutionary algorithms: a survey of the state of the art. *Comput Method Applied M* 191, 1245-1287 (2002) **DOI:10.1016/s0045-7825(01)00323-1**

[27] Takahama, T., Sakai, S. Constrained optimization by applying the /spl alpha/ constrained method to the nonlinear simplex method with mutations. *IEEE T Evolut Comput* 9, 437-451 (2005) **DOI:10.1109/tevc.2005.850256**

[28] Gämperle, R., Müller, S.D., Koumoutsakos, P. A parameter study for differential evolution. *Adv Intel S Fuzz S Evol C* 293-298 (2002)

[29] Liu, J., Lampinen, J. On setting the control parameter of the differential evolution method. *Proceedings of the 8th International Conference Soft Computing* (2002) p. 11-18

[30] Brest, J., Greiner, S., Boskovic, B., Mernik, M., Zumer, V. Self-adapting control parameters in differential evolution: a comparative study on numerical benchmark problems. *IEEE T Evolut Comput* 10, 646-657 (2006) **DOI:10.1109/TEVC.2006.872133**

Received 2023-11-29, revised 2024-08-28, accepted 2024-11-05
Original Scientific Paper

Data Availability *The data supporting the findings of this study are included in the article.*

Author Contribution *Afsharzadeh N. contributed to conceptualization, methodology, resources, validation, data curation, formal analysis, and programming. Yazdi, M.E. provided conceptualization, methodology, supervision. Lavasani A.M. completed conceptualization, review and editing, and consultation.*

Uporaba diferencialnega evolucijskega algoritma za termodinamično snovanje in omejena optimizacija cevno orebrenega prenosnika toplote

Povzetek *Cevno orebreni prenosniki toplote (COPT) so vrsta kompaktnih prenosnikov toplote (KPT), ki je razširjena v aplikacijah prenosa toplote med plini in tekočinami. V pričujoči študiji se za optimizacijo COPT učinkovito uporabljata algoritem diferencialne evolucije (DE) in njegova različica JDE s tehniko obvladovanja omejitev na ravni α. Za ciljni funkciji sta bili izbrani skupna teža in letni strošek obratovanja prenosnika toplote. Zajetih je bilo sedem konstrukcijskih spremenljivk: zunanji premer cevi, prečni razmik, vzdolžni razmik, razmik reber, število vrst cevi, višina in širina oblike. Za analizo prenosa toplote pod enakimi pogoji, kot so masni pretok, vstopna in izstopna temperatura, toplotna obremenitev in druge toplotne lastnosti, se uporablja metoda srednje logaritemske temperaturne razlike. Za reševanje optimizacijskih problemov so bistveno primernejši metahevristični iskalni algoritmi. Pri obeh ciljnih funkcijah so se izboljšali rezultati v primerjavi z genetskim algoritmom (GA) in tako imenovanim algoritmom iskanja prenosa toplote. Parametrična analiza je potrdila, da sta vrednosti ciljnih funkcij minimalni pri najmanjši vrednosti prečnega razmika. Predlagana metoda je preprosta in v splošnem uporabna pri termodinamičnem snovanju in optimizaciji COPT in drugih vrst KPT za različne namene.*

Ključne besede *cevno orebreni prenosnik toplote, termodinamična zasnova, optimizacija z omejitvami, diferencialni evolucijski (DE) algoritem, skupna teža, skupni letni strošek*

Microstructural and Mechanical Characterization of WAAM-fabricated Inconel 625: Heat Treatment Effects

Saravanakumar Krishnasamy ✉ – Saravanan Sambasivam – Balaji Vaiyampalayam Govindaraj
PSG College of Technology, Department of Production Engineering, India
✉ ksaravanakumr@gmail.com

Abstract *Wire arc additive manufacturing (WAAM) is a promising technique for producing complex geometries of nickel-based superalloys, such as Inconel 625. In this work, the microstructure and mechanical properties of Inconel 625 alloy produced by gas tungsten arc welding (GTAW) process of WAAM technology were analyzed to investigate the effects of heat treatment on the top and bottom zones of the multi-layered wall structure. The deposited specimens were heat treated at 980 °C for 2 hours, then water quenched (solution annealing). After heat treatment, microstructure reveals that the most common phases like laves, gamma, and mono carbides (MC) are dissolved, which is clear by optical microscopy (OM), scanning electron microscopy (SEM), and energy dispersive spectroscopy (EDS). Even after the heat treatment process, mechanical properties, such as micro-hardness results, demonstrate that the bottom zone of the multilayer wall structure has a higher hardness value than the top zone. After the secondary phases were eliminated by the solution annealing procedure, the ultimate tensile strength and yield strength were increased by nearly 17 % to 38 % and 15 % to 22 % in the top and bottom one of the multilayer wall structures, respectively.*

Keywords *wire arc additive manufacturing (WAAM), heat treatment, optical microscope, tensile strength*

Highlights:
- *WAAM with GTAW used to build multiwall Inconel 625 nickel-based superalloy structures.*
- *Heat treatment at 980 °C for 2 hours followed by water quenching was applied.*
- *Phases like Laves, gamma, and MC carbides dissolved after heat treatment.*
- *Hardness and strength improved; tensile strength increased by 17 % to 38 % after annealing.*

1 INTRODUCTION

Additive manufacturing (AM) has revolutionized the production of components with complex shapes, offering increased production flexibility and efficiency [1]. This method allows for the creation of fully dense parts using engineering and industrial materials such as steel, titanium, and aluminium [2]. wire arc additive manufacturing (WAAM) is a type of additive manufacturing (AM) that uses a digital model to build complex metal parts by melting and adding metal wire to the base material [3]. WAAM differs from powder-bed fusion systems, such as laser and electron beam ones, since it uses wire feedstock instead of powder [4]. WAAM has several advantages over powder-based AM technologies, including more availability of wire feedstock, cost-effectiveness, higher quality feedstock and deposition, and less work-in-progress waste [4]. Laser bed fusion and wire arc additive have their own advantages and disadvantages, and the choice between them depends on the specific requirements of the project. Laser powder bed fusion is better for small to medium-sized components with high detail and internal features, while WAAM is more suitable for large builds and customized objects with decent precision and accuracy [3] and [4]. Particularly, arc-welding-based additive manufacturing techniques, like WAAM, have gained popularity in the manufacturing industry for their ability to assemble large metal components quickly and cost-effectively [5]. WAAM utilizes an electrical arc as a heat source to melt and deposit filler wire layer by layer, creating near-net structure components. The process has successfully produced massive metallic components, demonstrating its potential for cost-effective manufacturing [6]. Three main types of WAAM processes exist: gas tungsten arc welding (GTAW), gas metal arc welding (GMAW), and plasma arc welding (PAW). GMAW boasts a higher deposition rate (2 to 3 times) compared to GTAW or PAW, but it comes with drawbacks such as instability, increased weld smoke, and spatter [7]. On the other hand, GTAW-based WAAM provides direct control over energy and material inputs, allowing for more stable welding. Unlike traditional automatic welding, GTAW WAAM follows a non-unidirectional welding path [8].

AM technologies, such as direct laser deposition (DLD), microplasma additive manufacturing (MPAM), and cold metal transfer wire arc additive manufacturing (CMT-WAAM), have garnered significant attention in the manufacturing industry due to their ability to produce complex metal parts with high precision and minimal material waste. Among these technologies, WAAM, particularly the cold metal transfer (CMT) variant, has shown notable advancements in the production of heat-resistant superalloys like Inconel 625, making it a preferred method for manufacturing components that require high strength and durability under extreme conditions [9] and [10].

Crucial parameters influencing the WAAM process with GTAW include welding current, voltage, polarity, gas flow rate, welding speed, and electrode tip angle [11]. Inconel 625, a nickel-based superalloy renowned for its exceptional corrosion resistance, high strength, and toughness, finds applications across various industries like aerospace, chemical processing, and marine engineering. When produced using WAAM, Inconel 625 exhibits a microstructure characterized by elongated crystallites, accompanied by favorable mechanical properties [12]. WAAM offers several advantages, including high energy density, excellent surface forming capabilities, and the ability to customize microstructures by adjusting process parameters. Refractory metals like niobium and molybdenum, present in nickel-chromium alloys, contribute to solid-solution hardening, further enhancing the properties of alloys like Inconel 625 [13].

The CMT discontinuous WAAM strategy, in particular, allows for lower heat input and improved control over the welding process, leading to finer details and enhanced performance in thin-walled components. Recent studies have demonstrated that this method can significantly improve the material properties of Inconel 625, including a 15 % increase in ultimate tensile strength at room temperature and improved wear resistance at elevated temperatures [14] and [15].

The selection of Inconel 625 for this study is based on its exceptional properties, including high strength, corrosion resistance, and weldability, which are essential for applications requiring durability under extreme conditions. The alloy's higher nickel content compared to other Inconel grades enhances its performance in high-temperature environments, making it a preferred choice in sectors like aerospace and chemical processing. Furthermore, the ability to fabricate complex shapes directly from digital models using WAAM provides significant advantages in design flexibility and material utilization, which are critical in modern engineering applications. As the research into Inconel 625 continues to evolve, the findings not only contribute to the understanding of additive manufacturing techniques but also support the development of innovative solutions for high-performance engineering challenges [9], [10], [14], and [15].

Studies exploring Inconel 625 production using WAAM techniques have shown diverse results. A low heat input WAAM process with a metal inert gas technique demonstrated increased hardness, while a pulsed tungsten inert gas (TIG) welding process with activated flux improved penetration and tensile strength [16]. Additionally, WAAM-produced Inconel 625 alloys exhibited favorable microstructure, forming quality, and metallurgical bonding, with Ni and granular precipitated phases identified and promising microhardness values reported [17]. The WAAM method has been extended to create functionally gradient materials, such as SS321/Inconel 625, with minimal interface issues. The resulting alloy displayed a columnar dendritic structure with enhanced mechanical properties [18]. Furthermore, the adoption of AM technology and practices has been explored, focusing on their impact on mechanical properties, microstructures, and welding parameters [19].

Optimization studies on WAAM techniques, such as activated tungsten inert gas welding, have been conducted to identify ideal welding process parameters for specific plate thicknesses [19]. Discussions on WAAM techniques and commonly used metallic feedstock materials emphasize the cost-effectiveness and efficiency of wire-based AM compared to powder-based AM for producing large structural metallic components [20] and [21]. Following the GTAW of the WAAM process, a solution annealing process at 980 °C for two hours is employed to dissolve secondary phases further enhancing the mechanical qualities. Subsequently, water quenching is utilized to rapidly cool the material, preventing the formation of new secondary phases and improving tensile qualities. In summary, the WAAM production method for Inconel 625 alloy, incorporating the GTAW process, solution annealing, and water quenching, consistently delivers high-quality, mechanically sound parts suitable for diverse industrial applications. The significance of selecting 980 °C and a 2-hour duration for annealing WAAM-printed Inconel 625 alloy lies in the observed effects on material properties. Research indicates that annealing at 980 °C for 2 hours increases the yield strength of the material. Specifically, the yield strength remains stable up to 1 hour of annealing but exhibits growth after the 2-hour heat treatment. Additionally, this annealing process is linked to the dissolution of a significant amount of the Laves phase and the precipitation of the δ phase, signifying a substantial impact on the material's microstructure. Moreover, the annealing conditions have been associated with the absence of softening behavior in Inconel 625 at 980 °C, in contrast to the observed softening at 1050 °C. Therefore, the deliberate choice of 980 °C and 2 hours for annealing is crucial due to its profound influence on the mechanical properties and microstructure of WAAM-printed Inconel 625, ultimately shaping the material's strength and behavior [16], [22], and [23].

In the realm of AM, particularly with WAAM utilizing the GTAW process, the current research aims to delve into the microstructural and mechanical characterization of Inconel 625. This nickel-based super alloy, renowned for its remarkable corrosion resistance and high strength, plays a pivotal role in diverse industries, including aerospace, chemical processing, and marine engineering. The novelty of this study lies in its comprehensive exploration of the effects of heat treatment on Inconel 625 additively manufactured through WAAM with the GTAW process. By investigating crucial parameters, the research not only contributes to the understanding of the manufacturing process but also delves into the intricate details of post-processing techniques. The incorporation of solution annealing at 980 °C offers a unique perspective on enhancing mechanical qualities and mitigating the formation of secondary phases. This novel approach promises to provide valuable insights into optimizing the production of high-quality, mechanically robust Inconel 625 components, advancing the field of AM with practical implications for various industrial applications.

2 METHODS AND MATERIALS

A Gantry semiautomatic welding robot and a Fronius TPS 400i LSC ADV power source are utilized to complete the WAAM process, which was employed to construct the multilayer wall structure using the GTAW method, as shown in Fig. 1. The multilayer wall structures are additively welded onto a base plate made of Inconel 625 alloy with a thickness of 13 mm. To determine the elemental composition of the base plate, an optical emission spectroscopy (OES) test is performed. Table 1 displays the elemental compositions found in the base plate.

Fig. 1. Images of a) GTAW welding machine setup with gantry, and b) WELDING TORCH nozzle and WAAM printed multi-layered wall

Table 1. Chemical composition of Inconel 625 Alloy

Elements	Si	Mn	Cr	Mo	Nb	Fe	Ni
wt. %	0.27	0.25	21.12	8.84	3.80	4.26	60.15

The substrate was machined using a grinding machine and cleaned with acetone to get rid of faults and ensure a flawless weld structure. The process parameters considered were: current of 220 V, travel speed of 90 mm/min, and filler wire feed speed of 380 mm/min. The voltage was kept between 12 V and 14 V. The plate is firmly fixed on the fixture after the parameters are established to avoid distortion. Using a 3.2 mm diameter thoriated tungsten electrode that cannot be consumed, the base metal is fused to create the molten pool. To construct the thin-walled component, a molten pool was formed in

the base plate and filled with Inconel 625 alloy filler wire with a 1.2 mm diameter using a GTAW method based on WAAM technology. The shielding gas used throughout the deposition procedure was pure 99.99 % argon inert gas with a flowing at a rate of 15 l/min.

By using the selected process parameter, the thin multilayer wall structure is built layer by layer. By keeping a cooling period of 120 seconds between succeeding layer depositions, the interlayer temperature was decreased to room temperature. As shown in Fig. 1b, the multilayer wall structure was built, which has 10 mm thickness, 66 mm height, and 120 mm length.

2.1 Heat Treatment Process

A muffle furnace, a kind of furnace that delivers homogeneous heating of the material, is commonly used for the heat treatment process. This makes it easier to make sure that the whole material is heated to the needed temperature and maintained there for the necessary amount of time, leading to a more uniform microstructure throughout the material. The material is heated to a certain temperature, with 980 °C, and maintained at that temperature for a specific amount of time 2 hours, throughout the heat treatment process [23] and [24]. Based on the material being annealed and the required qualities, this temperature and time are carefully selected [12]. Overall, the solution annealing procedure is a crucial step in producing high-quality Inconel 625 weldments made by WAAM since it helps to enhance the material's mechanical qualities and make sure it satisfies the specifications of several industrial applications.

2.2 Specimen Processing and Characterization

The top and bottom zones of the fabricated multilayer wall structure's microstructure, mechanical properties, and fractography morphologies were then examined in two states: as-deposited and heat-treated condition.

Samples from the top and bottom zones of the multilayered wall structure are obtained, each measuring 10 mm by 10 mm, to perform a microstructural examination. The extracted samples are polished to a mirror-like finish without any noticeable scratch marks using coarse and fine grid emery sheets. Sample specimens are electrolytically etched for 15 to 20 seconds while connected to the direct current (DC) supply using 2.1 grams of oxalic acid mixed with 200 milliliters of distilled water. To obtain the samples' microstructures, etched samples were analyzed for microstructure under an optical microscope and with a SEM at various magnifications and locations in as-deposited and heat-treated condition.

The top and bottom zones of the constructed multilayer wall structure were subjected to tensile, fractography, and microhardness tests, both in as-deposited and heat-treated condition. The American Society for Testing Materials (ASTM) E8 standard's tensile test was carried out using a Universal Testing Machine (UTM) 600 kN [25]. The tensile specimens are extracted from the multi-layered wall structure using wire-cut EDM machining process. This test is used to determine the metallic material's tensile strength, yield strength, and ductility.

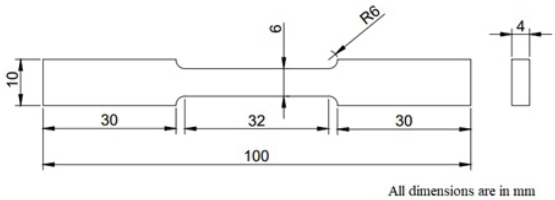

Fig. 2. Schematic of Tensile specimen dimensions as per ASTM - E8 standard [25]

The dimensions of the tensile specimen according to the ASTM E8 standard are displayed in Fig. 2 Also, the fractography test on the fractured surface of the broken tensile specimen was analyzed in the SEM system to better understand the properties of the fractured surface. To determine the hardness of the samples from the created multilayer wall structure in as-deposited and heat-treated condition, a microhardness test was carried out in the Vickers hardness machine with a force of 1 kg.

3 RESULT AND DISCUSSIONS

3.1 Physical Characteristics

The GTAW process's semi-automatic welding robot deposits the multilayer wall structure, which consists of 42 layers with a height of 65 mm and a length of 120 mm. Due to the unidirectional deposition technique, building and collapse are seen at the beginning and end of deposition in the produced multilayer wall structure, as shown in Fig. 3.

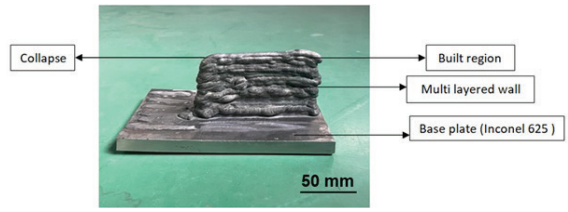

Fig. 3. Image of WAAM printed Inconel 625 Multilayer wall structure

The built zone reaches its maximum height in comparison to the collapse region as the number of layers rises. This leads to inaccurate deposited component dimensions. This issue is fixed by adding extra passes at the wall's end point to maintain an equal height between the starting and ending points.

3.2 Microstructural Analysis

An optical microscope (OM) and a SEM were used to conduct a microstructural study on the sample in order to understand the underlying changes in phases and grain structure morphology in the top and bottom zones of the constructed multilayer wall structure in as-deposited and heat-treated conditions. The constructed multilayer wall structure exhibits the effective grain structure.

3.2.1 Optical Microstructure as-Deposited Condition

The top and bottom zones of the created multilayer wall structure's optical microstructure pictures in their as-deposited form are depicted in Fig. 4.

Most of the heat input during the WAAM process is lost by convection and radiation to the surrounding atmosphere. The bottom layer has efficient heat conduction because of the heat being transported away through the substrate as well; as a result, solidification happens quickly. Equiaxed blocky-like structure and crystallite morphology are only practically feasible at very low temperature gradient levels. The rate of solidification, however, is slower at the top of the formed structure than it is at the bottom because of the slow heat transfer. The observed microstructure has varied in various areas of the deposit because of this difference in thermal behavior during the additive welding process. The microstructure in the top zone appears to be layered, and the deposited layer can be identified by elongated crystallites, as shown in Fig. 4a. The equiaxed blocky structure in the bottom zone of the multilayer wall structure is shown in Fig. 4b due to the varied

solidification rates. Moreover, gamma phases are only present in the top zone of the multilayer wall structure, while secondary phases can be found in both the top and bottom zones of the built structure. These secondary phases' generation and distribution in Inconel 625 produced by WAAM can be influenced by several process variables, including heat input and cooling rate. Controlling these variables is crucial for reducing the production of detrimental phases and improving the material's properties for the intended application. This can be achieved by performing a heat treatment process.

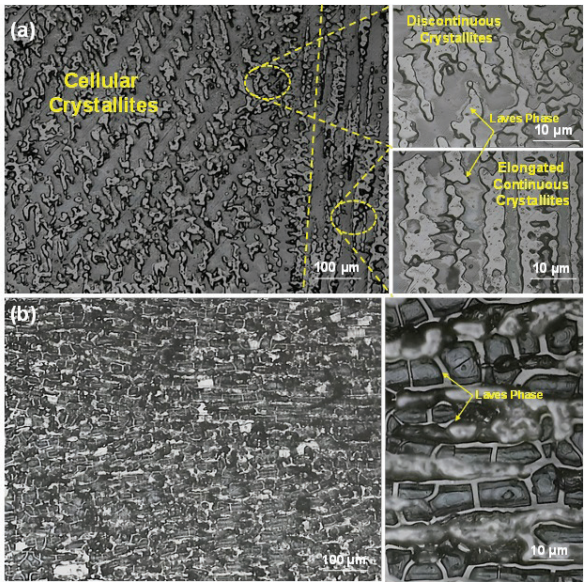

Fig. 4. Optical microstructure of Inconel 625 alloy in as – WAAM deposited condition from: a) top zone, and b) bottom zone

3.2.2 Optical Microstructure with Heat Treatment

After heat treatment, it is found that there is an elimination of secondary phases that can lead to a more homogeneous microstructure in both the top and bottom zones of the multilayer wall structure. Improvements in mechanical characteristics and microstructure can all be attained through the disappearance of secondary phases after heat treatment of multilayer wall structures.

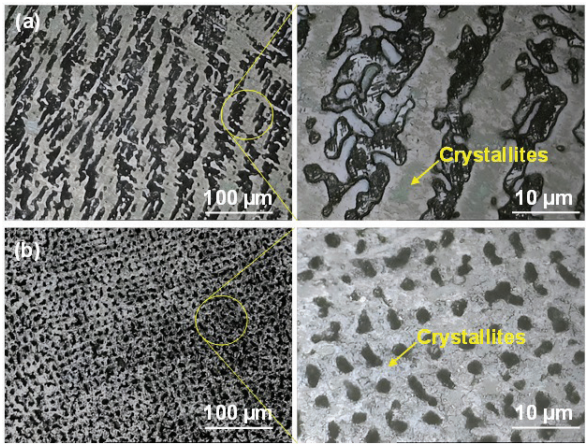

Fig. 5. Optical microstructure of Inconel 625 alloy in WAAM deposited and post heat treated condition from: a) top zone, and b) bottom zone

Due to recrystallization occurring during the heat treatment process in the bottom zone of the built structure, the microstructure changes from the blocky structure to the refined grain structure, as shown in Fig. 5b. Moreover, there is less uniaxial segregation of microstructure. After heat treatment, the precipitates in the microstructure were dissolved, and evenly distributed re-precipitation occurred.

Overall, recrystallization is encouraged by the heat treatment process, which also improves the microstructure, and produces finer, more equiaxed grains and better material properties. As a result, components made in as-deposited and heat treated condition using Inconel 625 WAAM have different optical microstructures. The blocky microstructure of Inconel 625 also changes into a fine-grained one after heat treatment, which enhances the material's mechanical properties.

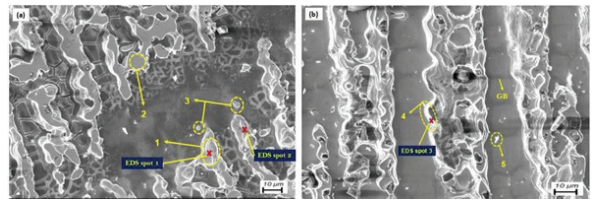

Fig. 6. SEM image of: a) top zone as-deposited condition alloy by WAAM manufacturing, and b) bottom zone as-deposited condition alloy by WAAM manufacturing

To understand the microstructure in its as-deposited condition, a SEM image at higher magnification, as shown in Fig. 6 was utilized. The top zone of the constructed multilayer wall structure's zones 1 and 2 (Fig. 7a and b) revealed by EDS analysis has a composition that is nearly identical to that of the Inconel 625 alloy's primary phase, the Ni-based matrix. This composition amply demonstrates the solute segregation with the erratic bright patches known as the 'laves phase' and the small particle sizes also visible in the microstructure image, which is identified as MC carbides. The EDS data presented in Fig. 7d further elucidates the elemental distribution across three spots, showing the following weight percentages.

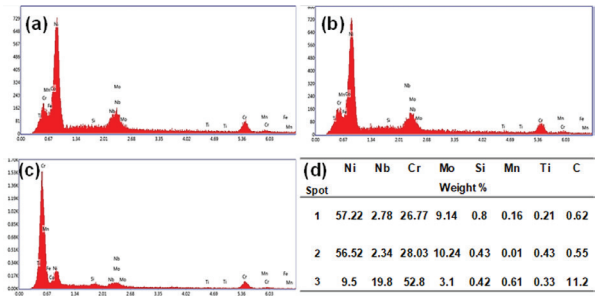

(d)

Spot	Ni	Nb	Cr	Mo	Si	Mn	Ti	C
	Weight %							
1	57.22	2.78	26.77	9.14	0.8	0.16	0.21	0.62
2	56.52	2.34	28.03	10.24	0.43	0.01	0.43	0.55
3	9.5	19.8	52.8	3.1	0.42	0.61	0.33	11.2

Fig. 7. EDS spectra from: a) spot 1 of top zone, b) spot 2 of top zone, c) spot 3 of bottom zone, and d) elemental analysis at the spots

The Cr-rich M23C6 carbides at the grain boundaries were confirmed by the EDS image in Fig. 7c, according to a spot examination of the bottom zone. Further the EDS data indicates a high niobium content in Spot 3 suggests the formation of MC carbides, which are critical for enhancing the strength and stability of the alloy at elevated temperatures.

Fig. 8 displays the presence of delta precipitates, which are formed due to the dissolution of secondary phases like laves phase, gamma matrix, and MC carbides.

The dissolution of secondary phases is clear by the EDS spot analysis, which is shown in Fig. 9 on the top and bottom zones of the multilayer wall structure, and some of the secondary phases are undissolved, which results in the reduction of ductility after the heat treatment process of additively deposited Inconel 625 alloy. Notably, the chromium (Cr) content is significantly higher in the bottom zone (34.04 %) compared to the top zone (20.79 %), which may enhance

corrosion resistance and strength. Additionally, niobium (Nb) is much lower in the bottom zone (2.34 %) than in the top zone (11.32 %), potentially explaining the observed decrease in ductility.

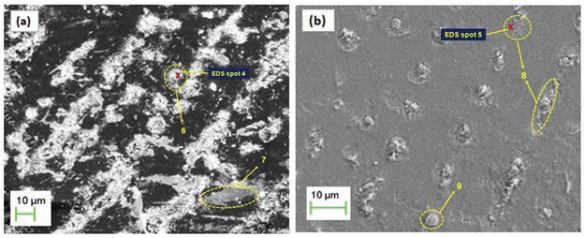

Fig. 8. SEM microstructure of WAAM printed Inconel 625 alloy from: a) top zone heat treated condition, and b) bottom zone heat treated condition

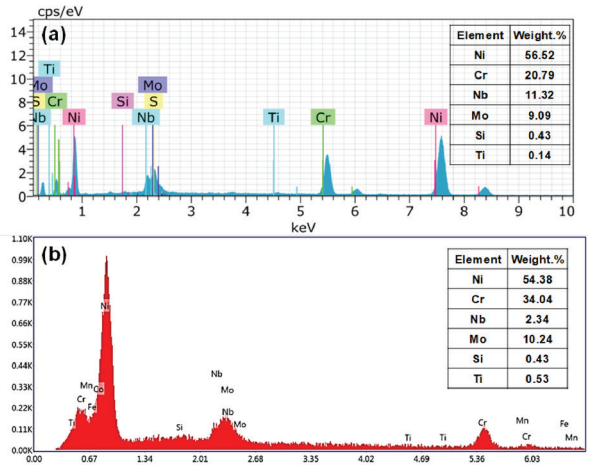

Fig. 9. EDS spectra from: a) spot 4 of the top zone after heat treated condition, and b) spot 5 of the top zone after heat treated condition

3.3 Mechanical Characteristics

To analyze the mechanical property of the multilayer wall structure, a tensile test was taken on the top and bottom zones. Additionally, a fractography test was carried out in the fractured zone of the tensile specimen to correlate the results of the mechanical and microstructural property tests. Microhardness tests were also carried out. These tests were carried out both in as-deposited and heat-treated condition in the top and bottom zones of the built multilayer wall structure.

3.3.1 Tensile Test

The top and bottom zones of the multilayer wall structure's tensile specimens, as per ASTM-E8 standard dimensions, were extracted using wire cut EDM and tested using a universal testing machine (UTM) under two different conditions: as-deposited and heat-treated. Tensile test data, including yield strength, elongation, and tensile strength, are displayed in Table 2. In the as-deposited condition, the yield strength of the Inconel 625 alloy ranges from 340 MPa to 394 MPa, with the top zone exhibiting slightly higher values than the bottom zone. This variation is likely due to differences in cooling rates and thermal gradients during the deposition process. The tensile strength also shows notable differences between the top and bottom zones, with values ranging from 527 MPa to 623 MPa. The elongation percentage was observed to be higher in the bottom zone (59 %) compared to the top zone (53 %), suggesting a more ductile microstructure in the bottom region, possibly due to lower residual stresses or a more favorable grain structure.

According to the results of the tensile tests, the yield strength and tensile strength in the top and bottom zones are improved by 15 % and 22 % and 17 % and 38 %, respectively, after the heat treatment process. Specifically, the yield strength increases to 457 MPa in the top zone and 416 MPa in the bottom zone, which aligns with literature data, suggesting that heat treatment promotes precipitation strengthening and the relaxation of residual stresses, leading to improved yield strength. The tensile strength also improves significantly, reaching approximately 729 MPa in both zones. However, the elongation percentage decreases after heat treatment, with the top zone showing 43.5 % and the bottom zone 47 %. This reduction in elongation could be attributed to the formation of precipitates that hinder dislocation movement, resulting in increased strength but reduced ductility. The comparison with literature data indicates that the mechanical properties of Inconel 625 fabricated using WAAM are competitive with traditional methods such as casting.

3.3.2 Fractography Test

The fractured surface of the tensile specimen was analyzed by using SEM is shown in the Fig. 10a and b which represents the top and bottom zones of multilayer wall structure in as-deposited condition, whereas Fig. 10c and d represents the top and bottom zones with heat treated condition. Fractography test was conducted using the fractured tensile specimen to identify the connection between the microstructure and the mechanical properties.

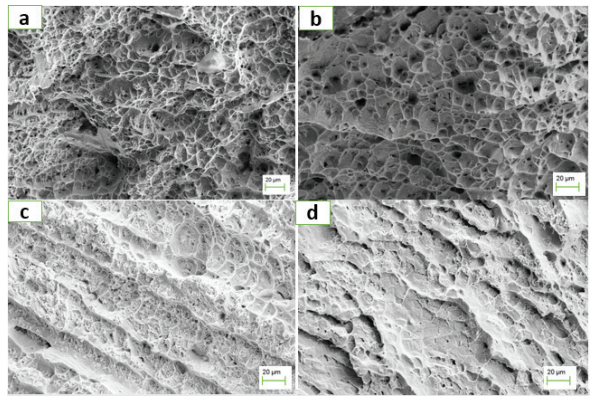

Fig. 10. Fractography micrograph of: a) and b) samples in as-deposited condition, and c) and d) in heat treated condition of top and bottom zone of the multilayer wall structure

The deep dimples in the as printed samples corroborates the occurrence of micro void coalescence and associated ductile fracture with an elongation of 50 % to 60 %. However, on the other hand, the

Table 2. Tensile test results of as deposited and post printing heat treated Inconel 625 alloy

Mechanical properties	As deposited			Heat treated			As cast
	Top zone	Bottom zone	Literature data [9], [10], [26]	Top zone	Bottom zone	Literature data [9], [10], [26]	
Yield strength [MPa]	394 ± 12	340 ± 08	376.9 to 400.8	457 ± 11	416 ± 6	414 to 615	350
Tensile strength [MPa]	623 ± 11	527 ± 09	647.9 to 687.7	729 ± 8	728 ± 11	827 to 1024	710
Elongation [%]	53 ± 5	59 ± 2	43 to 46.5	43.5 ± 4	47 ± 4	30 to 60	40

heat treated sample shows a shallow dimples with plateau formation, which indicates the chances of localized plastic deformation and inter-granular cracking along with a minimal amount of micro-void coalescence. Similar observations were reported in welding studies of Ramor 500 Armor Steel [27] and [28]. Further studies are required to understand the mechanism.

3.3.3 Microhardness Test

The built multilayer wall structure's top and bottom zones were measured for microhardness using the Vicker's hardness testing machine under two conditions: as-deposited and heat treated. Table 3 displays the results that were obtained. The hardness values for the samples that were heat-treated and that were as-deposited is appear to have undergone minimal change. However as compared to the top and bottom zone of the constructed multilayer wall structure, the hardness value in the bottom zone has improved in both the conditions. When compared to the literature data, the hardness values from the present study is higher than the reported ranges of 145 HV to 220 HV for the annealed condition and 243 HV to 247 HV for the as printed condition. This indicates that the multilayer wall structure in the current investigation demonstrates enhanced hardness properties relative to previously documented results.

Table 3. Microhardness of WAAM deposited Inconel 625 alloy in as-deposited and heat-treated condition

Mechanical properties Micro-hardness (HV)	Heat treated condition		As-deposited condition	
	Top zone	Bottom zone	Top zone	Bottom zone
Present study	215.9 ± 09	273.8 ± 08	209.4 ± 04	287 ± 06
Literature data [10]	145 to 220		243 to 247	

4 CONCLUSIONS

The Inconel 625 alloy multi-layered wall construction underwent unidirectional GTAW welding, resulting in decreased height at the end of the process, necessitating additional passes for dimensional accuracy. Following a 2-hour heat treatment at 980 °C, the microstructure exhibited fine dentrites, a transformation from discontinuous and elongated dentrites. The multilayer wall structure primarily comprised Ni-Cr matrix-based gamma phase, laves phases, and MC carbides, dissolved through the heat treatment process. This treatment led to a 17 % to 38 % improvement in ultimate tensile strength and yield strength in the top zone and a 15 % to 22 % enhancement in the bottom zone, attributed to delta precipitate formation and laves phase dissolution. While the average microhardness showed no significant change post-heat treatment, the bottom zone exhibited a higher microhardness value compared to the top zone.

REFERENCES

[1] Nguyen, H.D., Pramanik, A., Basak, A.K., Dong, Y., Prakash, C., Debnath, S., Buddhi, D. A critical review on additive manufacturing of Ti-6Al-4V alloy: Microstructure and mechanical properties. J Mater Res Technol 18 4641-4661 (2022) **DOI:10.1016/j.jmrt.2022.04.055**

[2] Korkmaz, M.E., Waqar, S., Garcia-Collado, A., Gupta, M.K., Krolczyk, G.M. A technical overview of metallic parts in hybrid additive manufacturing industry. *J Mater Res Technol* 18 384-395 (2022) **DOI:10.1016/j.jmrt.2022.02.085**

[3] Günen, A., Gürol, U., Koçak, M., Cam, G. A new approach to improve some properties of wire arc additively manufactured stainless steel components: Simultaneous homogenization and boriding. *Surf Coat Technol* 460 129395 (2023) **DOI:10.1016/j.surfcoat.2023.129395**

[4] Gürol, U., Altınay, Y., Günen, A., Bölükbaşı, Ö.S., Koçak, M., Çam, G. Effect of powder-pack aluminizing on microstructure and oxidation resistance of wire arc additively manufactured stainless steels. *Surf Coat Technol* 468 129742 (2023) **DOI:10.1016/j.surfcoat.2023.129742**

[5] Pan, Z., Ding, D., Wu, B., Cuiuri, D., Li, H., Norrish, J. Arc welding processes for additive manufacturing: a review. *Trans Intell Weld Manuf* 1 3-24 (2018) **DOI:10.1007/978-981-10-5355-9_1**

[6] Chintala, A., Tejaswi Kumar, M., Sathishkumar, M., Arivazhagan, N., Manikandan, M. Technology development for producing Inconel 625 in aerospace application using wire arc additive manufacturing process. *J Mater Eng Perform* 30 5333-5341 (2021) **DOI:10.1007/s11665-021-05781-6**

[7] Owais M., Mridul J., Noor W., N.H. Wire arc additive manufacturing (WAAM) of Inconel 625 Alloy and its microstructure and mechanical properties. *Int Res J Eng Technol* 08 1518-1528 (2021)

[8] Geng, H., Li, J., Xiong, J., Lin, X., Zhang, F. Optimization of wire feed for GTAW based additive manufacturing. *J Mater Process Technol* 243 40-47 (2017) **DOI:10.1016/j.jmatprotec.2016.11.027**

[9] Ferreira, A.A., Reis, A.R., Amaral, R.L., Cruz, J.M., Romio, P.C., Seabra, J.O., et al. Mechanical and microstructural characterisation of bulk Inconel 625 produced by direct laser deposition. *Mater Sci Eng A* 838 142777 (2022) **DOI:10.1016/j.msea.2022.142777**

[10] Yuan, X., Qiu, H., Zeng, F., Luo, W., Li, H., Wang, X. et al. Microstructural evolution and mechanical properties of Inconel 625 superalloy fabricated by pulsed microplasma rapid additive manufacturing. *J Manuf Process* 77 63-74 (2022) **DOI:10.1016/j.jmapro.2022.03.008**

[11] Wang, X., Wang, A., Wang, K., Li, Y. Process stability for GTAW-based additive manufacturing. *Rapid Prototyp J* 25 809-819 (2019) **DOI:10.1108/RPJ-02-2018-0046**

[12] Thakur, P.P., Chapgaon, A.N. A review on effects of GTAW process parameters on weld. *IJRASET* 4 136-140 (2016) **DOI:10.13140/RG.2.2.11535.38569**

[13] Kumar, S.P., Elangovan, S., Mohanraj, R., Ramakrishna, J.R. A review on properties of Inconel 625 and Inconel 718 fabricated using direct energy deposition. *Mater Today: Proc* 46 7892-7906 (2021) **DOI:10.1016/j.matpr.2021.02.566**

[14] Hack, H., Link, R., Knudsen, E., Baker, B., Olig, S. Mechanical properties of additive manufactured nickel alloy 625. *Addit Manuf* 14 105-115 (2017) **DOI:10.1016/j.addma.2017.02.004**

[15] Yangfan, W., Xizhang, C., Chuanchu, S. Microstructure and mechanical properties of Inconel 625 fabricated by wire-arc additive manufacturing *Surf Coat Technol* 374 116-123 (2019) **DOI:10.1016/j.surfcoat.2019.05.079**

[16] Tanvir, A.N.M., Ahsan, M.R., Ji, C., Hawkins, W., Bates, B., Kim, D.B. Heat treatment effects on Inconel 625 components fabricated by wire+ arc additive manufacturing (WAAM)-part 1: microstructural characterization. *Int J Adv Manuf Technol* 103 3785-3798 (2019) **DOI:10.1007/s00170-019-03828-6**

[17] Akselsen, O.M., Bjørge, R., Ånes, H.W., Ren, X., Nyhus, B. Microstructure and properties of wire arc additive manufacturing of Inconel 625 *Metals* 12 1867 (2022) **DOI:10.3390/met12111867**

[18] Mohan Kumar, S., Rajesh Kannan, A., Pravin Kumar, N., Pramod, R., Siva Shanmugam, N., Vishnu, A.S., Channabasavanna, S.G. Microstructural features and mechanical integrity of wire arc additive manufactured SS321/Inconel 625 functionally gradient material. *J Mater Eng Perform* 30 5692-5703 (2021) **DOI:10.1007/s11665-021-05617-3**

[19] Kumar, S.S., Maheswaran, C.B., Kannan, T.D.B. Experimental investigation on a pulsed TIG welding of Inconel 625. *Mater Today: Proc* 45, 2109-2114 (2021) **DOI:10.1016/j.matpr.2020.09.724**

[20] Guo, C., Ying, M., Dang, H., Hu, R., Chen, F. Microstructural and intergranular corrosion properties of Inconel 625 superalloys fabricated using wire arc additive manufacturing. *Mater Res Express* 8 035103 (2021) **DOI:10.1088/2053-1591/abe977**

[21] Ravi, G., Murugan, N., Arulmani, R. Microstructure and mechanical properties of Inconel-625 slab component fabricated by wire arc additive manufacturing. *Mater Sci Technol* 36 1785-1795 (2020) **DOI:10.1080/02670836.2020.1836737**

[22] Karayel, E., Bozkurt, Y. (2020). Additive manufacturing method and different welding applications. *J Mater Res Technol* 911424-11438 **DOI:10.1016/j.jmrt.2020.08.039**

[23] Sivakumar, J., Vasudevan, M., Korra, N.N. (2020). Systematic welding process parameter optimization in activated tungsten inert gas (A-TIG) welding of Inconel 625. Trans Indian Inst Met 73 555-569 **DOI:10.1007/s12666-020-01876-1**.

[24] Dhinakaran, V., Ajith, J., Fahmidha, A.F.Y., Jagadeesha, T., Sathish, T., Stalin, B. (2020). Wire arc additive manufacturing (WAAM) process of nickel-based superalloys-A review. *Mater Today: Proc* 920-925 **DOI:10.1016/j.matpr.2019.08.159**

[25] Holt, J.M. *Uniaxial tension testing. In Mechanical Testing and Evaluation*. ASM International (2000) Materials Park
[26] Seow, C.E., Coules, H.E., Wu, G., Khan, R.H., Xu, X., Williams, S. Wire+ arc additively manufactured Inconel 718: Effect of post-deposition heat treatments on microstructure and tensile properties. *Mater Des* 183 108157 (2019) **DOI:10.1016/j.matdes.2019.108157**
[27] Günen, A., Gürol, U., Koçak, M., Çam, G. Investigation into the influence of boronizing on the wear behavior of additively manufactured Inconel 625 alloy at elevated temperature. *Prog Addit Manuf* 8 1281-1301 (2023) **DOI:10.1007/s40964-023-00398-8**
[28] Günen, A., Bayar, S., Karakaş, M.S. Effect of different arc welding processes on the metallurgical and mechanical properties of Ramor 500 armor steel. *J Eng Mater Technol* 142 021007 (2020) **DOI:10.1115/1.4045569**

Received 2024-03-14, revised 2024-08-20, accepted 2024-10-03
Original Scientific Paper.

Data availability *The data that support the findings of this study are available from the corresponding author upon reasonable request.*

Author contributions *Saravanakumar K contributed to conceptualization, formal analysis, investigation, methodology, and writing – original draft; Saravanan S provided supervision, project administration, writing – review & editing, and resources; Balaji VG contributed to data curation, validation and visualization.*

Karakterizacija mikrostrukture in mehanskih lastnosti Inconela 625 po obločnem navarjanju z žico: učinki toplotne obdelave

Povzetek *Obločno navarjanje z žico (WAAM) je obetavna tehnika za izdelavo kompleksnih geometrij superzlitin na osnovi niklja, kot je Inconel 625. V pričujoči raziskavi smo analizirali mikrostrukturo in mehanske lastnosti zlitine Inconel 625, izdelane s postopkom obločnega varjenja s plinskim volframom (GTAW) v tehnologiji WAAM, da bi raziskali učinke toplotne obdelave na zgornjo in spodnjo cono večplastne stenske strukture. Vzorci so bili dve uri toplotno obdelani pri 980 °C, nato pa ohlajeni z vodo (žarjenje z raztopino). Po toplotni obdelavi mikrostruktura razkriva, da so najbolj pogoste faze, kot so laves, sekundarne faze (γ') in monokarbidi (MC), raztopljene, kar je jasno opazno z optično mikroskopijo (OM), skenirno elektronsko mikroskopijo (SEM) in energijsko disperzijsko spektroskopijo (EDS). Tudi po postopku toplotne obdelave mehanske lastnosti, kot so rezultati mikrotrdote, kažejo, da ima spodnja cona večplastne stenske strukture višjo vrednost trdote kot zgornja cona. Po odstranitvi sekundarnih faz s postopkom raztopinskega žarjenja sta se natezna trdnost in meja plastičnosti v zgornjem in spodnjem delu večplastne stenske strukture povečali za skoraj 17 % do 38 % oziroma 15 % do 22 %.*

Ključne besede *obločno navarjanje z žico (WAAM), toplotna obdelava, optični mikroskop, natezna trdnost*

Quantitative Sequential Modelling Approach to Estimate the Reliability of Computer Controlled Pneumatically Operated Pick-and-Place Robot

Satheesh Pandian Durairaj ✉

KLN College of Engineering, India

✉ satheesh.klnce@gmail.com

Abstract *Pneumatically controlled pick-and-place robots are an integral part of contemporary manufacturing processes and have the potential to enhance the precision and velocity of numerous production-related tasks. As automation continues to disrupt various sectors, the role of these robots is becoming increasingly crucial. Achieving peak performance in robot operations requires a relentless focus on safety and reliability. As a result, subsequence reliability should be considered carefully from the initial part of the design phase. Roboticists need to identify the dependable subsequences and parts of the robot's operational framework in prior to access the system's overall reliability. This analytical technique aids in component identification and demonstrates how to measure redundancy to ensure dependability and robustness. Based on recent theories and frameworks, the researchers can understand the factors that have more impact towards the reliability of pneumatically driven pick-and-place robots. Thus, this research work improves an exhaustive dependability analysis of a computer-controlled pneumatically operated pick-and-place robot. As part of our methodology, we use modern LabVIEW software to conduct a comprehensive failure analysis and estimate the reliability of the sequence.*

Keywords *pneumatically controlled pick-and-place robots, automation, reliability, LabVIEW software, failure analysis*

Highlights:

- *Modern factories use pneumatic robots to boost production speed and accuracy.*
- *Subsequence reliability ensures safety and optimal system performance.*
- *LabVIEW aids in dependability analysis, identifying key parts and redundancies.*
- *MRPM model focuses on redundancy and quantitative reliability calculations.*

1 INTRODUCTION

Pneumatically operated pick-and-place robots are essential components of contemporary manufacturing operations, providing accuracy and efficiency in task execution. These robots employ compressed air as propulsion, enabling them to execute rapid and precise pick-and-place operations within assembly lines and other manufacturing settings. The relevance of these entities lies in their capacity to optimize efficiency through the reduction of cycle times and the augmentation of throughput. Pneumatically controlled pick-and-place robots significantly enhance efficiency and quality assurance within manufacturing operations by effectively managing a wide range of materials and components [1].

The importance of automation in manufacturing is growing, as it brings about a significant transformation in industries by improving efficiency and production. Robots facilitate this shift by optimizing industrial processes accurately and efficiently. Their adaptability enables the completion of diverse activities, ranging from assembly to packaging, with uniformity and precision. In the current market landscape, firms are compelled to adopt automation and robots to maintain competitiveness, foster innovation, and effectively address the changing needs of consumers [2] and [3].

Safety and reliability are of utmost importance in robot activities within industrial settings, owing to the substantial hazards associated with such operations. Robots frequently collaborate with humans, operating extensive machinery and possibly dangerous substances. Using stringent safety standards mitigates the likelihood of accidents, injuries, and equipment damage. Moreover, ensuring dependable robot performance is essential for sustaining output and averting expensive periods of inactivity. The prioritization of safety and reliability serves the dual purpose of safeguarding workers and assets while cultivating a working environment that promotes efficiency and success [4].

Ensuring the entire reliability of the system is crucial during the design phase of robotics, with a particular emphasis on sequence reliability. Through careful evaluation of the dependability of each subsequence from the beginning, engineers will detect any vulnerabilities and enhance them for optimal reliability. This entails evaluating individual elements' dependability and interplay within the administrative structure. Through this approach, designers can minimize potential hazards and boost the robot's overall dependability, resulting in heightened operational availability, decreased expenses associated with maintenance, and improved efficacy in practical scenarios [5] to [7].

Analytical methodologies are of paramount importance in evaluating the dependability of robotic systems. Roboticists employ many techniques, including failure mode and effect analysis (FMEA), fault tree analysis (FTA), and reliability block diagrams (RBD), to detect potential failure modes and assess their influence on system reliability. Identifying components is a crucial aspect of this process, as it enables the recognition of essential elements and their respective probabilities of failure. Furthermore, redundancy techniques are employed to improve reliability and resilience, which may include the integration of backup components or duplicate

 DOI: 10.5545/sv-jme.2024.999

systems. By utilizing these analytical methodologies, roboticists can proficiently assess and enhance the dependability of robotic systems, guaranteeing optimal functionality across a wide range of operational contexts [8].

Current studies have concentrated on comprehending the variables that impact the dependability of pneumatically operated pick-and-place robots. This entails analyzing the impact of factors such as air pressure variations, component deterioration, and environmental circumstances on the system's functioning. Researchers can build theories and frameworks to optimize these robots' design, maintenance, and operation by gaining insights into these issues. The comprehension of these factors has significant importance in enhancing the overall reliability of a system, as it empowers engineers to enact proactive steps, such as carefully selecting sturdy components and establishing regular maintenance plans, to reduce prospective concerns. Eventually, it improves the reliability and durability of pneumatically operated pick-and-place robots in many industrial settings.

The primary aim of this study is to conduct a comprehensive examination of the reliability of a computer-controlled pneumatically operated pick-and-place robot. This seeks to assess multiple elements that impact the dependability of the robot, such as its components, operational conditions, and environmental factors. Through a comprehensive examination, this research aims to offer valuable insights that can improve the design, maintenance, and operation of comparable robotic systems. Finally, the objective is to enhance the reliability and performance of these systems in industrial environments.

The research approach employed in this study entails the utilization of contemporary LabVIEW software to perform an exhaustive failure analysis and assess the reliability of sequences. LabVIEW is a robust programming environment that empowers researchers to create customized programs to accomplish their research requirements. In our research, it enables the examination of several failure modes and their influence on the dependability of the pneumatically controlled pick-and-place robot. Using LabVIEW's functionalities, researchers can effectively collect and analyze data, enabling a comprehensive assessment of the system's reliability [9] and [10].

2 METHODS AND MATERIALS

The computer-controlled robot uses three pneumatic cylinders to rotate its base, lift things, and clamp them. The movable arm of the robotic system is fixed on a rotating base that can move from the source point to the target point in the appropriate locations. The base rotation is controlled by rack and pinion mechanism, which is fully operated by pneumatic cylinders and controlled with computers through solenoid direction control valves (DCV) [11]. The electrical relays and data acquisition cards (DAQ cards) with hardware interfacing circuits are connected with LabVIEW software are used to control the robot. The major components in automatic robot are shown in the Fig. 3.

The pneumatic cylinders 1, 2, and 3 in the pick-and-place robot are sequentially activated by energizing the solenoid coils 1, 2, and 3. The first cylinder serves the purpose of securing the objects within the conveyor line. In contrast, the second cylinder elevates the robotic arm to a predetermined height, preventing potential collisions with other peripherals linked to the machining center. Subsequently, the third cylinder is engaged to rotate the base to the designated position to position the components. The operational sequence exhibits a uniform temporal delay of five seconds. To obtain the reverse sequences in the pick and place robot, the computer consecutively energizes solenoid coils 2, 1, and 3 with a time delay of five seconds. Fig. 1 depicts the connectivity diagram of a computer-controlled pick-and-place robot [12].

The successive parts encompass the steps involved in sequence reliability estimation, the collection of failure data for each subsequence, the experimental test, the assessment of the failure probability function, the analysis of computer reliability, the subsequence reliability model, the results obtained, and the subsequent analysis and interpretation.

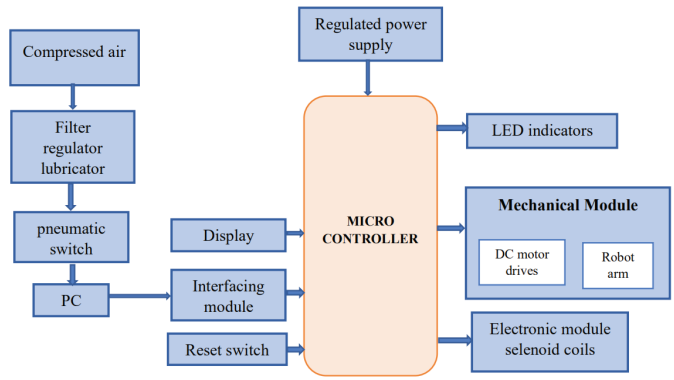

Fig. 1. Connectivity diagram of computer-controlled pick and place robot

The concluding section elucidates the outcome of this endeavor. The image of the pick and place robot (prototype) is taken for reliability analysis is shown in Fig 2.

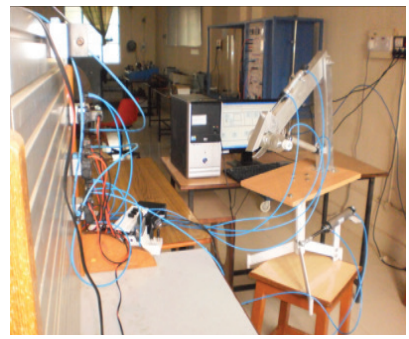

Fig. 2. Computer controlled pick and place robotic arm

2.1 Steps in Sequence Reliability Estimation

Sequential reliability estimation is a process used to assess the reliability of a system or process over time, often in the context of ongoing operation or testing [13] and [14]. Here are the general steps involved in sequential reliability estimation:

- Define the system: Clearly define the system or process you are evaluating for reliability. This includes identifying all components, subsystems, and their interconnections.
- Identify failure modes: Determine the potential failure modes of each component or subsystem within the system. This entails knowing the circumstances or stresses that can lead to failure as well as how each component can fail.
- Define reliability metrics: Establish the reliability metrics that will be used to evaluate the system. Common metrics include mean time between failures (MTBF), probability of failure within a given time frame, or reliability function over time.
- Data collection: Collect data on system performance and failures over time. This data may come from field observations, testing, or

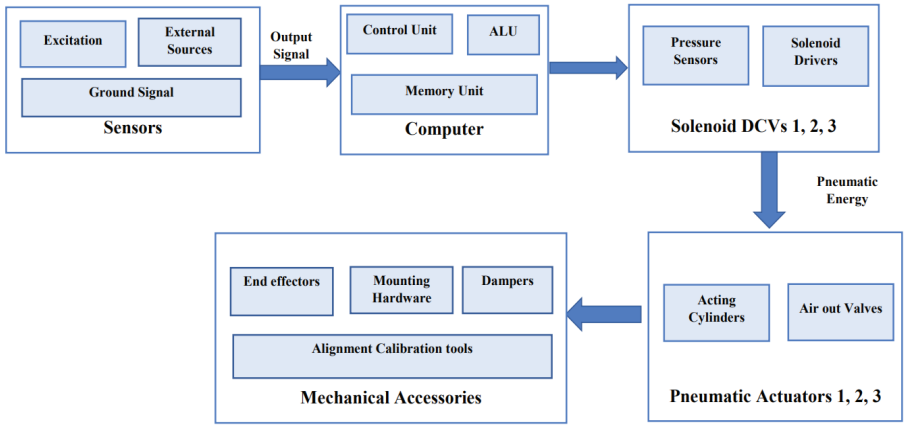

Fig. 3. Major components of automatic pick and place robot

simulations. Ensure that the data is comprehensive and accurately reflects the operational conditions of the system.

- Model development: Develop a statistical model to represent the reliability of the system based on the collected data. This model describe factors such as time, usage, environmental conditions, and maintenance activities.
- Initial reliability assessment: Use the initial data and model to estimate the current reliability of the system. This provides a baseline for comparison as the analysis progresses.
- Continuous monitoring: Continuously monitor the system for additional failures and collect updated data. This may involve real-time monitoring, periodic inspections, or ongoing testing
- Update model: Incorporate new data into the statistical model and update the reliability estimates accordingly. This allows the reliability assessment to adapt to changes in the system's performance over time.
- Evaluate trends: Analyze the trend of reliability over time to identify patterns or anomalies. Look for factors that may be influencing reliability, such as changes in operating conditions or maintenance practices.
- Risk assessment: Assess the implications of the observed reliability trends on system performance, safety, and cost. Identify potential risks associated with ongoing operation and determine if any corrective actions are necessary.
- Decision making: Use the reliability estimates and risk assessment to inform decision-making processes regarding system maintenance, repair, or replacement. Consider factors such as cost-effectiveness, safety, and operational requirements.
- Iterative process: Sequential reliability estimation is an iterative process that may require periodic updates and adjustments as new data becomes available or as the system undergoes changes. Continuously refine the analysis to improve the accuracy of reliability assessments and optimize system performance.

By following these steps, organizations can effectively assess and manage the reliability of their systems over time, helping to ensure safe and efficient operation.

Fig. 5 illustrates the systematic failure analysis of each subsequential component in the computer-controlled pick-and-place robot as part of the reliability analysis.

2.2 Connectivity of the Sequences

The concept of connectivity within a pick and place robot system pertains to the coherent integration and synchronization of diverse

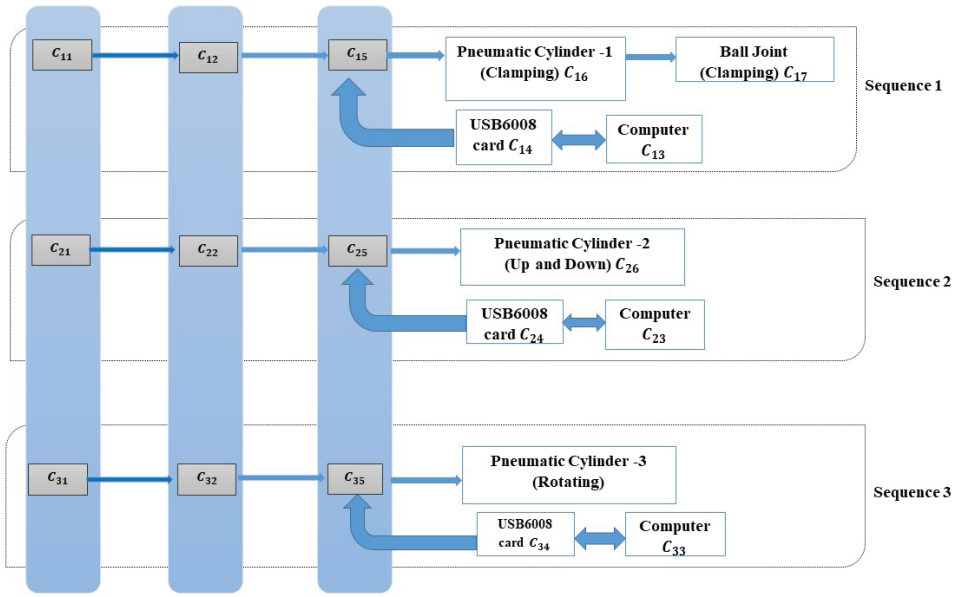

Fig. 4. Connectivity diagram of the sequences

components and processes that are fundamental to the functioning of the system [15]. The major components in the sequences are illustrated in Fig. 4.

2.2.1 Sequence 1

The activation of the solenoid DCV is accomplished by the computer, which transmits a signal to the universal serial bus (USB) card [16]. The solenoid DCV is responsible for starting pneumatic cylinder 1, which facilitates the execution of the clamping action via the ball joint. Activating the pneumatic module involves using pneumatic accessory components, including an air compressor, filter, and solenoid DCV.

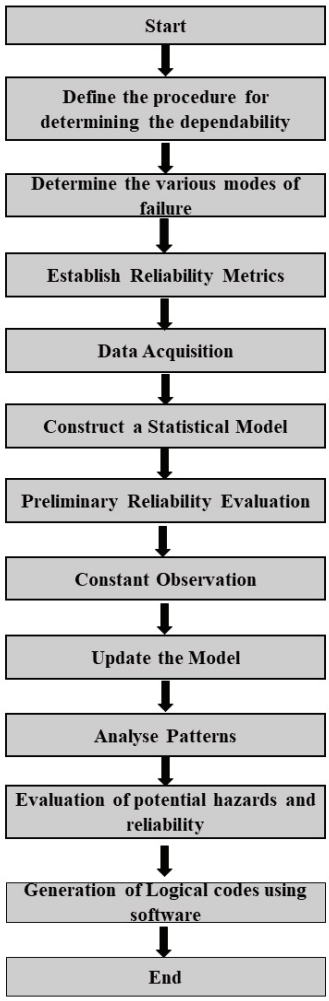

Fig. 5. Steps in sequential reliability estimation

Let, P_{11} probability of failure for component C_{11}, P_{12} probability of failure for component C_{12}, P_{13} probability of failure for component C_{13}, P_{14} probability of failure for component C_{14}, P_{15} probability of failure for component C_{15}, P_{16} probability of failure for component C_{16}, and P_{17} probability of failure for component C_{17}.

2.2.2 Sequence 2

In sequence 2, the robot comprises a pneumatic module and a USB acquisition card connected to a computer. This configuration is similar to sequence 1, except for the ball joint.

Let, P_{21} probability of failure for component C_{21}, P_{22} probability of failure for component C_{22}, P_{23} probability of failure for component C_{23}, P_{24} probability of failure for component C_{24}, P_{25} probability of failure for component C_{25}, and P_{26} probability of failure for component C_{26}.

2.2.3 Sequence 3

Sequence 3 encompasses all the constituent elements included in sequence 1 except the ball joint. Additionally, it incorporates the rack and pinion, base, and column structures.

Let, P_{31} is probability of failure for component C_{31}, P_{32} probability of failure for component C_{32}, P_{33} probability of failure for component C_{33}, P_{34} probability of failure for component C_{34}, P_{35} probability of failure for component C_{35}, P_{36} probability of failure for component C_{36}, P_{37} probability of failure for component C_{37}, and P_{38} probability of failure for component C_{38}.

2.3 Failure Data Collection for Each Sub Sequence

The failure rate for each sub-sequential component of sequences 1, 2, and 3 is measured in million hours. The fault data is obtained by measuring the difference between the necessary output value and the actual output value of the subcomponents under the condition of random input values. The robot's overall functioning primarily relies on a computer connected to a USB 6008 DAQ card. It is necessary to employ a distinct evaluation approach to assess the reliability of both the computer and the USB DAQ card. This dependability prediction model is beneficial for obtaining accurate outcomes in analytical tasks [17]. Except for the failure rate data for the computer and USB DAQ card, the remaining component data is presented in the subsequent table, arranged sequentially, specifically numbered 1, 2, and 3.

3 EXPERIMENTAL

Accurate prediction of reliability in mechanical subsystem is crucial for the robot as it significantly influences its total functionality. The reliability of each material in the mechanical structure is computed and utilized as input values to forecast the entire automatic machine using the merged reliability prediction model (MRPM). Tension and torsion tests are performed on various materials, including mild steel, cast iron, and aluminum. Subsequently, to determine the failure probability and dependability for each material, obtaining the failure rate distribution for different load circumstances is necessary. Therefore, the probability distribution is employed to represent the distribution of failure rates. The selection of the appropriate material for constructing the mechanical frame structure of automatic machines based on the failure probability and reliability values.

Computer-based pneumatically controlled pick and place robots utilize materials such as mild steel, cast iron, and aluminum due to their adequate mechanical strength and stress resistance for various operating load circumstances at each structural point. Furthermore, these components can endure thermal characteristics, such as heat capacity, thermal expansion, thermal conductivity, and thermal stress, at the operational temperature of the automation system within each sub-module. Therefore, the materials mentioned above are chosen to conduct tension and torsion tests to analyze reliability [18].

3.1 Failure Probability Function

Probabilistic distribution for loads

$$P(X_X < X_S) = F(X_S) = \frac{e^{\left[\frac{-(X_X \mu)}{2\sigma^2}\right]^2}}{\sigma\sqrt{2\pi}}. \quad (1)$$

Standard deviation of load

$$(\sigma_{load}) = X_S - X_X . \quad (2)$$

Failure probability

$$(P_X) = 1 - F(X_S). \quad (3)$$

The given equation, Eq. (1) uses the normal probability distribution function to characterize the distribution of loads on the materials. This distribution, which spans the range between the ultimate load and the actual load, determines the materials' failure rate. When the load fluctuates within its elastic limit about the mean load, every material undergoes a failure rate. The average probability distribution determines the probabilistic distribution of failure rates for the actual load applied during material testing [19]. The failure rate and reliability data for the selected materials and standard mechanical accessories are presented in Tables 1 and 2.

Table 1. Failure rate and reliability of various materials

Material	Predicted operating load, X_X [kN]	Probabilistic distribution for actual load, P_X	Actual stress [N/mm²]	Probabilistic distribution for actual stress	Reliability $1–P(X)$
Mild steel	30	9.973×10^{-3}	149.2	2.005×10^{-3}	0.99899
Cast iron	5	0.1101	10.1859	0.06228	0.8899
Aluminum	0.8	0.054200	15.915	0.07574	0.92426

Table 2. Failure rate and reliability data for common Mechanical parts

Components	Time [10^6 h]	No. of failures	Failure rate	Probability of failure rate* $\times10^{-4}$	Reliabiltiy**	Average reliability
Directional control valves (solenoid), C_{14}	1	8.993	8.993	0.09	0.999991	0.999901
	2	35.972	17.986	0.36	0.999964	
	3	80.937	26.979	0.81	0.999919	
	4	143.888	35.972	1.44	0.999856	
	5	224.825	44.965	2.25	0.999775	
Pneumatic actuators, C_{15}	1	11.498	11.498	0.12	0.999988	0.9998848
	2	45.992	22.996	0.46	0.999954	
	3	103.482	34.494	1.04	0.999896	
	4	183.968	45.992	1.84	0.999816	
	5	287.45	57.490	2.3	0.999770	

*$(P_{kl} = 1– e^{-\lambda t})$, **$(R_{kl} = 1– P_{kl})$

Table 3. Probability of failure and reliability data for accessories

Component	Probability of failure (P)	Reliabiltiy (R)
Compressor	0.00621	0.99379
Filter	0.00600	0.99400
Ball joint	0.00300	0.99700
Rack and pinion	0.10194	0.89806
Base and column	0.10840	0.89150

Table 4. Failure rate and reliability data for DAQ card

Components	Failure rate (λ)	Probability of failure $(P_{kl} = 1– e^{-\lambda t}) \times 10^{-4}$	Reliabiltiy $(R_{kl} = 1– P_{kl})$
DAQ card (C36)	0.035	0.0343	0.9657

All components' reliability and failure statistics, except for the ball joints, are extracted from the table above and recorded in sequence 2. The compressor and filter unit failure rate was obtained from Tables 3 and 4 and recorded.

3.2 Reliability Analysis of Computer

The assessment of computer reliability comprises the analysis of the stability and dependability of computer systems, hardware, software, and networks to ensure consistent and error-free operation over the course of their lifetime [20] to [22]. Computer engineering and system design play a crucial role in various businesses, mainly where downtime or malfunctions can result in substantial financial losses, safety risks, or data breaches.

3.2.1 Reliability Prediction Model for Computer

The non-Poisson process model has been chosen as the framework for assessing the performance and measuring the reliability of the computer system. To evaluate the reliability of a computer system, the likelihood of failure is determined by calculating the anticipated number of failures. During the testing phase, data is collected periodically and utilized in the non-homogeneous Poisson process (NHPP) and programmable logic controller (PLC) prediction models.

3.2.2 Failure Data Collection of Computer

The calendar testing method involves providing input values to the system and collect the data on certain computer failure. This aids in identifying certain failure issues under vaious scenarios within the system. The quantity of disparities between the actual and desired production is recorded and organized in the Table 5.

Table 5. Fault data of computer in testing phase

Week	No. of failures	Actual failure rate (λ)	Week	No. of failures	Actual failure rate (λ)
1	4	0.066	9	3	0.05
2	3	0.05	10	5	0.0833
3	2	0.033	11	6	0.100
4	6	0.100	12	8	0.133
5	1	0.0166	13	4	0.066
6	7	0.1166	14	3	0.05
7	4	0.066	15	2	0.033
8	2	0.033			

3.3 Goodness of Fit Test

The goodness of fit test is used to determine whether the failure data obtained is sufficient to anticipate the computer's reliability. In this experiment, the hypothesis is chosen based on the adequacy of the acquired data for predicting dependability.

As computed, the total difference between F and F^* is compared with the standard values in the Table 6. The computed $(F–F^*)$ value is lower than the critical value of 3.5 (0.3740) found in the Table 6. As a result, the above hypothesis is accepted and the reliability calculation use the data above. The hypothesis test's outcomes indicate that the failure data gathered has enough predictive power to estimate the computer's reliability. Therefore, the reliability model that follows predicts the computer's reliability [23].

The model computes the reliability R_i and the $P_i(x)$ probability of failure.

Expected number of failures is defined in Eq. (4) as follows

$$\mu_w = \lambda\theta t_w + \frac{1}{\theta}. \quad (4)$$

Failure probability is calculated by Eq. (5) as

$$P_w = \frac{\mu_w}{t_{CPU}}, \quad (5)$$

and the reliability as in Eq. (6)

$$R_w = 1 - P_w, \tag{6}$$

where, t_{CPU} is CPU execution time for week, and θ probability parameter (assumed as 0.16). Sample calculation to find R_w using Eq. (6), and to find P_w we have to calculate μw as given in Eq. (5) as follows. For $t_w = 5$, $\lambda = 0.0714$ and $\theta = 0.16$, μw is calculated as

$$\mu_w = \frac{(0.0166 \times 0.16 \times 5) + 1}{0.16} = 6.333,$$

where $t_{CPU} = 8 \times 7 \times 5 = 280$, $P_w = 6.333/280 = 0.0226$, and $R_w = 1 - 0.0226 = 0.9774$.

Table 6. Goodness of fit test

Week	Number of failures	F	Expected number of failures	F^*	$D = \lvert F - F^* \rvert$
1	4	0.066	6.316	0.0619	0.0041
2	3	0.05	6.35	0.0623	0.0123
3	2	0.033	6.349	0.0623	0.0293
4	6	0.100	6.650	0.0652	0.0348
5	1	0.0166	6.333	0.0621	0.0455
6	7	0.1166	6.949	0.0682	0.0484
7	4	0.066	6.712	0.0658	0.0002
8	2	0.033	6.514	0.0639	0.0309
9	3	0.05	6.70	0.0657	0.0157
10	5	0.0833	7.083	0.0695	0.0138
11	6	0.100	7.35	0.0721	0.0279
12	8	0.133	7.846	0.0770	0.0560
13	4	0.066	7.108	0.0697	0.0037
14	3	0.05	6.95	0.0682	0.0182
15	2	0.033	6.745	0.0662	0.0332
Total ($F-F^*$)					0.3740

Table 7. Failure rate and reliability data of computer

Week (w)	No. of failures	Actual failure rate for CPU hours (λ)	Expected failures (μ)	Pobability of failure (P_w)	Reliabiity (R_w)	Reliabilty of computer (R_{com})
1	4	0.066	6.316	0.1127	0.8873	
2	3	0.05	6.35	0.0566	0.9434	
3	2	0.033	6.349	0.0377	0.9623	
4	6	0.100	6.650	0.0296	0.9704	
5	1	0.0166	6.333	0.0226	0.9774	
6	7	0.1166	6.949	0.0206	0.9794	
7	4	0.066	6.712	0.0171	0.9829	
8	2	0.033	6.514	0.0145	0.9855	0.9742
9	3	0.05	6.70	0.0132	0.9868	
10	5	0.0833	7.083	0.0126	0.9874	
11	6	0.100	7.35	0.0119	0.9881	
12	8	0.133	7.846	0.0116	0.9884	
13	4	0.066	7.108	0.0097	0.9903	
14	3	0.05	6.95	0.0088	0.9912	
15	2	0.033	6.745	0.0080	0.992	

3.4 The Reliability of Computer, R_{com}

The reliability values for each week execution hours are taken from the Table 7 and average reliability of computer is calculated as $R_{com} = 0.9742$.

3.5 The Reliability Model for Sub Sequences

For sequence 1:

$$RS_1 = \frac{[1-P_{11}]\cdot[1-P_{12}]\cdot[1-P_{13}]\cdot[1-P_{14}]\cdot[1-P_{15}]\cdot[1-P_{16}]+[1-P_{17}]}{2} = \frac{[R_{11}]\cdot[R_{12}]\cdot[R_{13}]\cdot[R_{14}]\cdot[R_{15}]\cdot[R_{16}]+[R_{17}]}{2}. \tag{7}$$

For sequence 2:

$$RS_2 = \{[1-P_{21}]\cdot[1-P_{22}]\cdot[1-P_{25}]\cdot[1-P_{26}]\}\cdot\{[1-P_{23}]\cdot[1-P_{24}]\}. \tag{8}$$

here, $P_{21}=P_{11}$, $P_{22}=P_{12}$, $P_{23}=P_{13}$, $P_{24}=P_{14}$, $P_{25}=P_{15}$, and $P_{26}=P_{16}$.

$$RS_2 = \{[R_{21}]\cdot[R_{22}]\cdot[R_{25}]\cdot[R_{26}]\}\cdot\{[R_{23}]\cdot[R_{24}]\}. \tag{9}$$

For sequence 3:

$$RS_3 = \frac{\left(\{[1-P_{31}]\cdot[1-P_{32}]\cdot[1-P_{33}]\cdot[1-P_{34}]\cdot[1-P_{35}]\cdot[1-P_{35}]\}\cdot\{[1-P_{37}]\cdot[1-P_{38}]\}\right)}{2}, \tag{10}$$

here, $P_{31}=P_{11}$, $P_{32}=P_{12}$, $P_{33}=P_{13}$, $P_{34}=P_{14}$, $P_{35}=P_{15}$, and $P_{36}=P_{16}$.

$$RS_3 = \frac{\{[R_{31}]\cdot[R_{32}]\cdot[R_{33}]\cdot[R_{34}]\cdot[R_{35}]\cdot[R_{36}]\}+\{[R_{37}]\cdot[R_{38}]\}}{2}. \tag{11}$$

Table 8: Reliability for all the sequences

Sequences	Components (C_{kl})	Reliability of each component	Reliability of sequences (RS)
Sequence 1	Air compressor (C_{11})	0.9938	0.9631
	Filter (C_{12})	0.9940	
	Computer (C_{13})	0.9742	
	USB 6008 DAQ (C_{14})	0.9657	
	Solenoid DCV (C_{15})	0.9999	
	Pneumatic actuator (C_{16})	0.9999	
	Ball joint (C_{17})	0.9970	
Sequence 2	Air compressor (C_{21})	0.9938	0.9291
	Filter (C_{22})	0.9940	
	Computer (C_{23})	0.9742	
	USB 6008 DAQ (C_{24})	0.9657	
	Solenoid DCV (C_{25})	0.9999	
	Pneumatic actuator (C_{26})	0.9999	
Sequence 3	Air compressor (C_{31})	0.9938	0.8650
	Filter (C_{32})	0.9940	
	Computer (C_{33})	0.9742	
	USB 6008 DAQ (C_{34})	0.9657	
	Solenoid DCV (C_{35})	0.9999	
	Pneumatic actuator (C_{36})	0.9999	
	Rack and pinion (C_{37})	0.8981	
	Base and column (C_{38})	0.8915	

The equation provided above is used to evaluate the reliability of each sequence for the computer-controlled pick-and-place robot by assessing the chance of failure with reliability. Table 8 displays the computed dependability of sequences 1, 2, and 3.

3.6 Reliability Calculation for Each Sequence

Reliability calculation for each sequence can be calculated using Eqs. (7) to (10):

For sequence 1:

$$RS_1 = \{\{0.9938 \times 0.9940 \times 0.9742 \times 0.9657 \times 0.9999 \times 0.9999\} + 0.9970\} / 2 = 0.9631.$$

For sequence 2:

$$RS_2 = \{0.9938 \times 0.9940 \times 0.9999 \times 0.9999\} \times \{0.9742 \times 0.9657\} = 0.9876 \times 0.9408 = 0.9291.$$

For sequence 3:

$RS_3 = \{\{0.9938\times0.9940\times0.9742\times0.9657\times0.9999\times0.9999\} + \{0.8981\times0.8915\}\}/2 = 0.8650.$

The average values of the above sequential reliabilities are used to quantify the overall robot system reliability as follows:

Total Reliability of robot

$R = (RS_1 + RS_2 + RS_3)/3 = (0.9631+0.9291+0.8650)/3 = 0.9191.$

4 RESULTS AND DISCUSSION

The equation provided above is utilized to evaluate the reliability of each sequence for the computer-controlled pick-and-place robot by assessing the chance of failure. Figs. 6 to 8 display the computed dependability of sequences 1, 2, and 3.

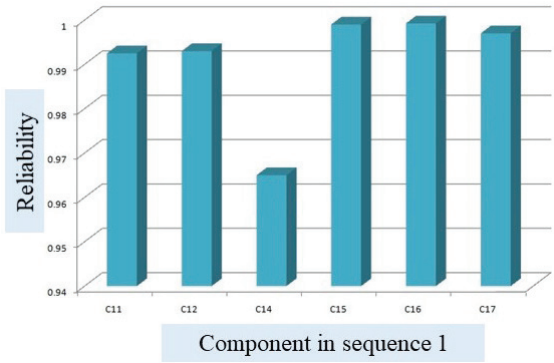

Fig. 6. Reliability of each sub component in sequence 1

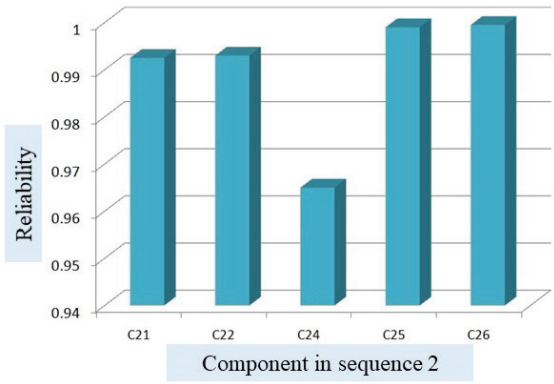

Fig. 7. Reliability of each sub component in sequence 2

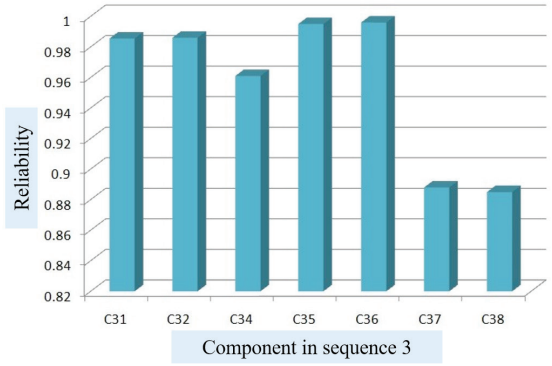

Fig. 8. Reliability of each sub component in sequence 3

The Figs 6 and 7 presents the specifics of sequences 1 and 2. The USB DAQ card (C_{14}) exhibits a imperfect level of reliability compared to other subcomponents utilized in the primary rotation of sequence 1 within the pick and place robot. In sequence 1, the solenoid DCV (C_{15}) and pneumatic actuators (C_{16}) exhibit superior dependability compared to other components, including the compressor (C_{11}), filter (C_{12}), and ball joint (C_{17}).

The Fig. 8 presents the following data for sequence 3. The base and column structure (C_{38}) and rack and pinion (C_{37}) exhibit the lowest reliability compared to the other components.

The USB DAQ card (C_{34}) demonstrates the second lowest reliability in this sequence when compared to other components such as compressors (C_{31}), filters (C_{32}), solenoid DCVs (C_{35}), and pneumatic actuators (C_{36}).

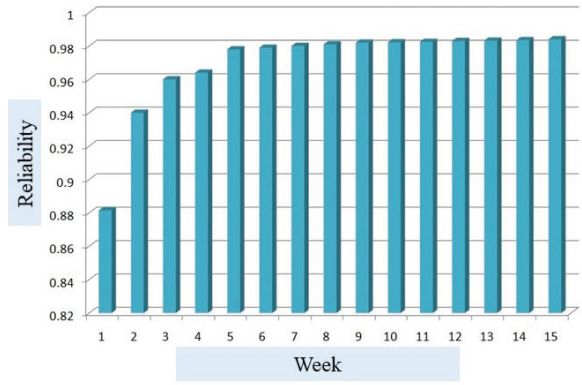

Fig. 9. Reliability of computer (C_{13}, C_{23}, and C_{33}) from testing data

Fig. 9 illustrates that a computer's reliability increases as the testing duration is extended. This is because faults or bugs are identified and rectified weekly during testing. Hence, the dependability of a computer is enhanced before its integration with operational components.

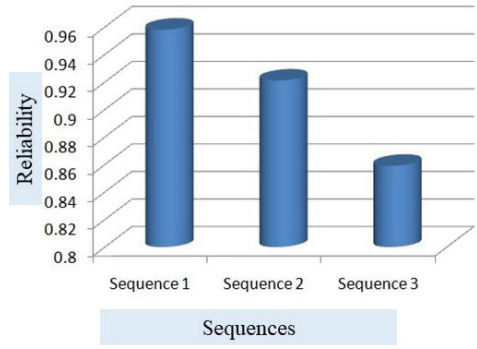

Fig. 10. Reliability for each sequence

In computer-controlled pick-and-place robots, the graph presented above serves the purpose of identifying the essential sequence. The pick and place robot utilizes the sequence 3 for base rotation, which exhibits comparatively lower reliability when compared to other sequences such as lift and down actuation and clamping. The crucial sequence for the autonomous pick-and-place robot in this case study is sequence 3. The key subcomponents of a computer-controlled pick-and-place robot are determined by utilizing the prior probability of failures derived from expert data and the failure rate data obtained from testing [24] to [25]. The failure probability distribution function and previously computed failure probability are used to rank all the modules in the provided graph in Fig. 10.

5 CONCLUSION

To enhance the dependability of the automation system, it is necessary to identify the intricacies of its functional components and develop a reliability model to measure its reliability. Using the MRPM model enables the designer to focus on the redundancy design. Quantitative reliability calculations are employed to ascertain the sequences with the highest criticality level. Qualitative and quantitative evidence can also be used to forecast prior and posterior reliability. The total reliability of the real-time mechatronic system was assessed throughout the design phase through a comprehensive failure analysis and a merged reliability prediction model. The absolute reliability of the robot was evaluated by estimating the reliability of its mechanical accessory components and materials. A number of materials, such as aluminium, cast iron, and mild steel, have their likelihood of failure assessed using the failure probability distribution function that was created from experimental test data from the tensile test. The test is performed on all materilas under operational load situation to find the probability distribution function for failure. The reliability of all materials pertaining to mechanical components is also evaluated by the computation of failure probability. The selection of the appropriate material for the material's structure was determined using a dependability calculation, as outlined in this research article. Furthermore, it was determined that the base rotation sequences (sequence 3) hold the utmost significance in the computer control pick and place robot.

REFERENCES

[1] Li, S., Rameshwar, R., Votta, A.M., Onal, C.D. Intuitive control of a robotic arm and hand system with pneumatic haptic feedback. *IEEE Robot Autom Let* 4, 4424-4430 (2019) **DOI:10.1109/LRA.2019.2937483**

[2] Bakrania, K., Patel, K. Failure mode and effect analysis of pneumatically operated pick and place robot. *Int J Adv Res Comp EngTech* 492-498 (2020)

[3] Jha, M.K., Raval, N.S. Analytical study on pneumatically controlled pick and place robot. *Int J Res Appl Sci Eng Tech* 6, 2384-2390 (2018)

[4] Liu, Z., Hu, J., Li, Y. Research on the reliability analysis of pneumatically controlled pick-and-place robot in manufacturing. *IEEE 4th International Conference on Mechanical, Control and Computer Engineering* 170-174 (2021)

[5] Rahman, M.H., Haque, S., Monir, M.F.A., Uddin, M.F., Alam, S.B. Fabrication of a revolutionary pick-and-place robot with omnidirectional mobility. *International Conference on Image Processing and Robotics* 1-6, (2024) **DOI:10.1109/ICIPRoB62548.2024.10544036**

[6] Borrell, J., Perez-Vidal, C., Segura, J.V. Optimization of the pick-and-place sequence of a bimanual collaborative robot in an industrial production line. *Int J Adv Manuf Tech* 130, 4221-4234 (2024) **DOI:10.1007/s00170-023-12922-9**

[7] Zhou, J., Huang, J., Ma, X., Lee, A., Kosuge, K., Liu, Y.-H. Design, modeling, and control of soft syringes enabling two pumping modes for pneumatic robot applications. *IEEE-ASME T Mech* 29 889-901 (2024) **DOI:10.1109/TMECH.2023.3345458**

[8] Maheshwari, S., Jain, V.K. (2019). Design and analysis of pneumatic pick and place robot. *Int J EngAdv Tech* 9, 197-201

[9] Yu, J., Ren, Y. Reliability analysis and improvement of pneumatic pick-and-place robot based on fault tree analysis. *J Mech Eng Resea Develop* 43, 30-36 (2020)

[10] Patel, A., Desai, S. Study of reliability analysis of pneumatically operated pick and place robot. *Int J Eng Inn Techn* 8 50-55 (2018)

[11] Amuthak Kannan, R., Kannan, S.M. Satheesh Pandian, D. (2005). Reliability analysis of software-based automation system. *2nd International Conference on Mechatronics* 805-811.

[12] Kotaiah, B. Prasad, M.V.S., Khan, R.A. An analysis of software reliability assessment with neuro fuzzy based expert systems. *Procedia Comput Sci* 62, 92-98 (2015) **DOI:10.1016/j.procs.2015.08.418**

[13] Dai, R., Guo, C. Researches and investigation on manufacturers reliability test data of electronics parts. *Enrgy Proced* 127 242-246 (2017) **DOI:10.1016/j.egypro.2017.08.125**

[14] Habchi, G., Barthod, C. An overall methodology for reliability prediction of mechatronic systems design with industrial application. *Reliab Eng Syst Safe* 155, 236-254 (2016) **DOI:10.1016/j.ress.2016.06.013**

[15] Kaczor, G., Mlynarski, S., Szkoda, M. Verification of safety integrity level with the application of Monte Carlo simulation and reliability block diagrams. *J Loss Prevent Proc* 41, 31-39 (2016) **DOI:10.1016/j.jlp.2016.03.002**

[16] Iqbal, J., Ullah, M.I., Khan, A.A., Muhammad, I. Towards sophisticated control of robotic manipulators: An experimental study on a pseudo-industrial arm. *Stroj vest-J Mech Eng* 61 465-470 (2018) **DOI:10.5545/sv-jme.2015.2511**

[17] Mahkovic, R. Position sensor for a mobile robot. *Stroj vest-J Mech Eng* 53 285-296 (2007)

[18] Yan, H., Li, J., Kou, Z., Liu, Y., Li, P., Wang, L. Research on the traction and obstacle-surmounting performance of an adaptive pipeline-plugging robot. *Stroj vest-J Mech Eng* 68 14-26 (2022) **DOI:10.5545/sv-jme.2021.7361**

[19] Omrčen, D., Nemec, B. Measuring knee movement using an industrial robot - gravity compensation for the automatic gripper. *Stroj vest-J Mech Eng* 48 87-97 (2002)

[20] Finžgar, M., Podržaj, P. Machine-vision-based human-oriented mobile robots: A review. *Stroj vest-J Mech Eng* 63 331-348 (2017) **DOI:10.5545/sv-jme.2017.4324**

[21] Škorc, G., Čas, J., Brezovnik, S., Šafarič, R. Position control with parameter adaptation for a nano-robotic cell. *Stroj vest-J Mech Eng* 57 313-322 (2011) **DOI:10.5545/sv-jme.2009.017**

[22] Bansal, S., Cheung, S.H. Analysis with multiple performance functions. *J Reliab Eng Syst Safe* 58 137-152 (2017)

[23] Yang, I.T., Hsieh, Y.-H., Kuo, C.-G. Integrated multiobjective framework for reliability-based design optimization with discrete design variables. *Automat Constr* 63 162-172 (2016) **DOI:10.1016/j.autcon.2015.12.010**

[24] Vartanov, M., Martynovich, N. Reliability for the robotic assembly of cylindrical parts. *Procedia Engineer* 150, 376-383 (2016) **DOI:10.1016/j.proeng.2016.06.727**

[25] Pandian, S.D., Asha, A. Predicting and enhancing the reliability of computer operated robot by considering software, hardware and interfacing modules. *Int J Chem Tech Res* 10 163-173 (2017)

[26] Pandian, S.D., Asha, A. Design for reliability of PLC based pneumatic operated pick and place robot by considering the mechanical properties and factor of safety - A case study. *Int J Appl Eng Res* 10 22-26 (2015)

Received 2024-03-26, revised 2024-07-03, accepted 2024-08-28
Original Scientific Paper.

Data availability The data used in this study are not available for sharing or distribution, as they are subject to confidentiality agreements and restrictions.

Author contributions Satheesh Pandian Durairaj: Conceptualization, Methodology, Data curation, Writing – original draft, Software, Formal analysis, Visualization.

Kvantitativno modeliranje sekvenc za ocenitev zanesljivosti računalniško vodenega pnevmatskega prijemalno-polagalnega robota

Povzetek *Pnevmatski prijemalno-polagalni (pick-and-place) roboti so ključni v sodobni proizvodni industriji, saj omogočajo natančno in hitro delo. Ker avtomatizacija še naprej spreminja različne sektorje, postaja vloga teh robotov vse pomembnejša. Doseganje vrhunske učinkovitosti pri delovanju robotov zahteva nenehno osredotočanje na varnost in zanesljivost. Zato je treba želeno zanesljivost skrbno preučiti že v začetnem delu faze načrtovanja. Izziv pa predstavlja identifikacija zanesljivih podsekvenc in kritičnih komponent v operativnem okvirju robotov za zagotavljanje celotne zanesljivosti in robustnosti sistema. Za naslovitev omenjenega izziva in potencialnih dvomov v zvezi z zanesljivostjo je potrebna podrobna analiza načinov odpovedi in ukrepov za zagotavljanje redundance. V raziskavi je bila zato opravljena identifikacija kritičnih komponent in delovnih podsekvenc, ki vplivajo na zanesljivost robotov. Razviti so bili ukrepi za redundanco, ki izboljšujejo robustnost sistema. Celovita analiza odpovedi je bila opravljena s programskim paketom LabVIEW. S simulacijo in analizo sekvenc robota je bila ocenjena zanesljivost različnih delovnih podsekvenc in komponent za podrobno oceno celotne zanesljivosti sistema.*

Ključne besede *pnevmatski prijemalno-polagalni (pick-and-place) roboti, natančnost, hitrost, avtomatizacija, varnost, zanesljivost, analiza odpovedi*

Connection Between the Dynamic Character of the Cutting Force and Machined Surface in Abrasive Waterjet Machining

Jelena Baralić[1] ✉ – Suzana Petrović Savić[2] – Branko Koprivica[1] – Stefan Đurić[2]

1 University of Kragujevac, Faculty of Technical Sciences Čačak, Serbia
2 University of Kragujevac, Faculty of Engineering, Serbia

✉ jelena.baralic@ftn.kg.ac.rs

Abstract *This paper presents the results of research on the effect of traverse speed on cutting forces and machined surface in abrasive water jet machining. The results indicated that there is a significant connection between the dynamic character of the cutting force in abrasive waterjet machining, namely, peaks in the cutting force signal, with the appearance of irregularities and uncut parts in the machined surface. Also, the research showed that the increase of the traverse speed produces an increase in the mean value of the static component of the cutting force. In experiments, the vertical component of the cutting force has been measured for an Aluminium AlMg3 12 mm thick rod cut at traverse speeds from 900 mm/min to 1100 mm/min. Cutting with higher traverse speeds yields more irregularities, which are connected with the appearance of peaks in the measured cutting force.*

Keywords *abrasive water jet, cutting force, traverse speed, machined surface*

Highlights:
- *Developed experimental setup for measuring AWJ cutting force.*
- *Proposed a new method for calculating AWJ cutting force.*
- *Analysed the effect of cutting force on machined surface.*
- *Analysed the effect of traverse speed on cutting force.*

1 INTRODUCTION

With the development of new materials such as ceramics, reinforced and composite materials and heat-sensitive alloys, the problem of their machining has arisen. For machining of some new materials, high cutting forces or low clamping forces are required. Some materials must be machined so that high temperatures do not occur in the cutting zone. Hence, there has been an increasing use of an abrasive water jet (AWJ) in the machining of new materials. Almost all types of materials can be cut with AWJ [1]. It is widely used in the contour cutting of materials and the machining of materials that are difficult to process [2]. A great advantage of this machining procedure is that contour cutting becomes very easy, no matter how complex the contour [3].

The AWJ machining process consists of several complex processes (formation of pressurised water, mixing of pressurised water and abrasive, erosion of machined material and others). A short overview of this AWJ cutting technology, with emphasis on the cutting forces, will be given.

AWJ machining is an unconventional process of recent date, which has been the subject of much research during the last two decades. The output of the AWJ machining process is a machined surface. In order to ensure the good quality of the machined surface and detect errors, it is necessary to monitor and control the AWJ process. That is why numerous experimental studies on process monitoring, such as monitoring of cutting forces [4] and [5], monitoring through acoustic and vibration signals [6] and [7] are currently being carried out. An overview of these monitoring methods will also be given. When cutting with an AWJ at high traverse speeds, there is an increase in the value of the roughness parameters of the cut surface, especially in the zone where the AWJ exits the machined material. Increasing the traverse speed results in decreasing the depth of the cut [8]. Depending on the traverse speed, occasionally the material is not completely cut. However, this important subject has not yet been thoroughly investigated.

Previous research of cutting forces in AWJ machining have dealt with the development of a universal system for measuring the cutting force [4] and [9], using the cutting force to determine some parameters of the kerf geometry (mainly the maximum depth of cut) [10]. However, there are very few works on this subject regarding the modelling.

In this paper, a simple mathematical model for the calculation of the cutting force is proposed. The equation for calculating the cutting force in conventional cutting is applied to AWJ machining and the abrasive water jet itself is represented as a cutting tool. When there is an incomplete cut of the material, the cutting force increases, because then the jet acts on the material of the workpiece with its entire surface, that is, the cross-sectional area of the chip is a maximum.

For the purpose of investigation of the variation of the cutting force with the traverse speed also at higher traverse speeds, a specific system for measuring the cutting force has been developed. Thus, this paper presents the experimental setup for force measurement based on a personal computer (PC), the measurement results, along with their discussion and important observations.

In their research, many authors have used the vertical component of the cutting force as the main parameter for monitoring and evaluating the AWJ cutting process. Kovačević [11] measured the vertical force component when cutting with the AWJ. A three-component dynamometer was used to measure the vertical component force. The vertical component of the cutting force was

DOI: 10.5545/sv-jme.2024.1008

measured for different values of the AWJ machining parameters. The aim of the research was to control the depth of cut based on the signal of the vertical force component. A precisely controlled depth of cut is very important when milling with the AWJ, i.e. engraving contours in the material. Measurements showed that the vertical component of the cutting force increases with increasing water pressure, nozzle diameter and abrasive mass flow rate. Also, it was found that it decreases with increasing standoff distance. Large oscillations in the values of the vertical force component indicated wear of the nozzle and that the maximum depth of cut had been reached.

In further research, Kovačević et al. [9] used the same principle for measuring the vertical cutting force component as in the previous work, with the aim of investigating the possibility of connecting the dynamic characteristics of the cutting force with the profile of the machined surface. Various parameters of the AWJ machining process were varied: water pressure, traverse speed, abrasive flow rate and standoff distance, in order to determine their effect on the cutting force and profile of the machined surface. It was found that both the abrasive flow rate and traverse speed have a slight effect on the vertical component of the cutting force. The influence of the AWJ machining parameters on the cutting force was analysed using stochastic modelling of the force data. Autoregressive moving average (ARMA) models are suitable for processing the results of measuring the vertical component of the cutting force for different values of the machining parameters. It was observed that the spectral density of the dynamic force ARMA model behaves in the same way as the measured profile of the machined surface. Based on this, they concluded that the signal of the vertical component of the cutting force can be considered as a potential parameter for the monitoring of the surface profile at the deformation wear zone.

Hassan et al. [10] proposed a model for monitoring the depth of cut during abrasive waterjet machining based on acoustic emission (AE) monitoring. The aim was to establish the dependence between these two parameters, so that the depth of the cut could be predicted based on the AE. Carbon steel AISI 1018 was used as a workpiece. The cut length of the samples was 38 mm to ensure a steady-state of cutting. During cutting, the working pressure values were varied from 100 MPa to 350 MPa. The vertical component of the cutting force was measured for all values of the working pressure, and the AE was also monitored. For all cuts, the mean value of the cutting force and the root mean square of the acoustic emission energy (AErms) for steady-state of cutting were calculated. It was observed that AErms increases linearly with an increase in the depth of cut and could be used for its on-line monitoring [10]. Hlavač et al. [4] constructed a special device for cutting force measurements during machining with AWJ. They monitored the signal of the cutting force in the normal and tangential directions before the start of cutting and during the cutting of the material. The workpieces were made of different materials, such as steels, duralumin, copper, and brass. The cutting of the workpiece was done in different modes. Also, the cutting was performed both with and without rotation of the cutting head. The tangential-to-normal force ratio (TNR) was taken as the most appropriate indicator for monitoring the cutting force and the quality of the machined surface. It was observed that the TNR reaches its maximum value at approximately 50 % of the maximum value of the traverse speed. Hlavač et al. [5] used the same measuring device as in [4], only the obtained signal of the vertical component of the cutting force was used for the detection of irregularities during cutting with AWJ, i.e. for the detection of incomplete cutting of the material.

Orbanić et al. [12] measured the diameter of the AWJ. A hard metal insert was the workpiece. During machining, the cutting force signal was monitored. Three characteristic areas can be observed on the obtained diagram of the cutting force: The first one was where the cutting force is equal to zero - the contact of the jet and the insert has not yet occurred. The second one is where the force increases - the jet comes into contact with the insert and the contact surface increases. The third one is where the force has stabilised - the whole jet is on the insert. The Vishay Transducers 1022 load cell was used to measure the vertical force component. Based on the change in the value of the vertical component of the force and the traverse speed, the diameter of the jet was calculated.

Momber [13] analysed the efficiency of the energy transformation using measurements of the vertical component of the cutting force. A Kistler dynamometer, model 9273, was used to measure the vertical component of the force. It was shown that the forces exerted by the high-speed jet on the workpiece can be successfully used to analyse the energy dissipation process during the formation of high-speed water-jets and during the mixing and acceleration of solid particles and air by high-speed waterjet (during the formation of the AWJ).

Baralić and Nedić [14] measured the cutting force using a three-component dynamometer for turning, KISTLER Type 9265A1, for samples of X5CrNi 18-10 with various thicknesses. The aim was to investigate the influence of the AWJ machining parameters (traverse speed, operating pressure, abrasive mass flow and material thickness) on the cutting force. It was found that an increase in the operating pressure leads to an increase of the cutting force. The effect of the abrasive mass flow on the cutting force is almost negligible, while an increase of the traverse speed, as well as an increase of the thickness of the material being machined, leads to an increase of the cutting force.

In the literature, there is no simple model for expressing the relation of the cutting force, as the significant output parameter of the system that can be measured, and the traverse speed as the input parameter that is set before the cutting of the material. Furthermore, the relation between these two quantities has not yet been thoroughly investigated for higher traverse speeds, when irregular cuts appear, as well as peaks in the cutting force. The present paper focuses on these shortcomings, with the goal of establishing a simplified $F_v(v_c)$ model, measure accurately the cutting force at higher traverse speeds, analyse the peaks in the cutting force in relation to the roughness of the surface, and validate the $F_v(v_c)$ model for the peak values of the cutting force. This paper contributes to the state of the art in the field by introducing a new $F_v(v_c)$ model and its experimental validation.

2 METHODS & MATERIALS

The main goal in today's production is to make as many products as possible in the shortest possible time and with as little investment as possible. In order to make this possible when machining with an AWJ, it is necessary to perform the machining with the highest possible traverse speeds. Machining with a high traverse speed results in an increase in the roughness parameters of the machined surface. This phenomenon is significantly expressed in the rough zone of the machined surface, that is, at the exit of the AWJ from the workpiece [15]. When the maximum traverse speed with which it is possible to completely cut materials of a certain thickness, is reached, the process of cutting with the AWJ becomes unstable and the material is, occasionally, not completely cut. The assumption is that in places where the material has not been completely cut, there is a sudden increase in the vertical component of the cutting force.

In the case that material is not completely cut, in practice the traverse speed is most often changed (reduced). The abrasive mass flow rate is rarely changed, and the operating pressure is almost never changed. Therefore, the influence of traverse speed on cutting force was analysed, even though the process of machining itself is influenced by numerous factors.

2.1 Proposed Model for Calculation of Cutting Force in AWJ Machining

During its movement through the machined material, the AWJ acts on the material with some force. This force has the same direction as the speed of the AWJ, that is, it is tangent to the path of the AWJ cutting front line, Fig. 1.

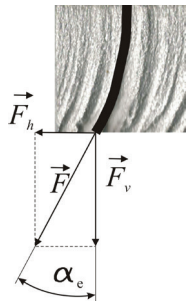

Fig. 1. Cutting force while machining with AWJ

The cutting force with which the AWJ acts on the workpiece can be divided into two components, vertical and horizontal:

$$\vec{F} = \vec{F}_v + \vec{F}_h. \quad (1)$$

In general, the diagram of the change of the vertical component of the cutting force F_v with time has the form as shown in Fig. 2. This diagram shows that the force F_v has its dynamic and static components. Due to the dynamic character of the AWJ machining process, the cutting force has a distinctly dynamic character. During a complete cut, the dynamic character of the cutting force is a consequence of oscillations in the values of the working pressure and the number of abrasive particles that are in contact with the object of processing. Also, a peak in the value of the cutting force can occur due to inclusions in the material of the workpiece. From Fig. 2, it can be seen that the value of the vertical cutting force component F_v increases when the AWJ starts cutting the sample.

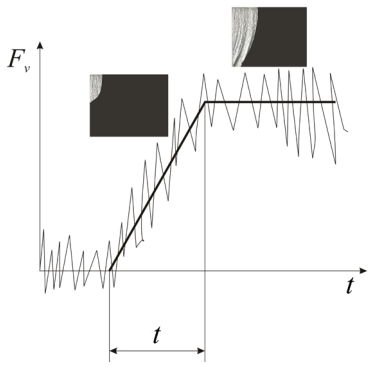

Fig. 2. Diagram of the vertical component of the cutting force, F_v

This value increases until the AWJ begins to cut completely through the entire thickness of the material. After that moment, there is no further increase in the value of the vertical cutting force component.

Abrasive particles in AWJ can be approximated by the cutting edge of a multi-cutting tool moving at a speed v_{awj} through the material being machined. At the same time, the cutting head moves at the traverse speed v_c, Fig. 3.

In a case of conventional cutting, the work W of the mechanical force F done along path L can be calculated in a simplified form as:

$$W = FL, \quad (2)$$

for a constant force along a straight path and when the force has the direction of the path. This work, during the cutting with the AWJ, can be equated with the cutting energy of the water jet, E_{awj}. Thus, the force can be determined by this energy,

$$F = \frac{E_{awj}}{L} = \frac{E_c V}{L}, \quad (3)$$

where E_c is the specific cutting energy of AWJ machining, V is the volume of removed material, and L is the length of the arc of the cutting front line. It is the length over which the cutting force acts (chip length).

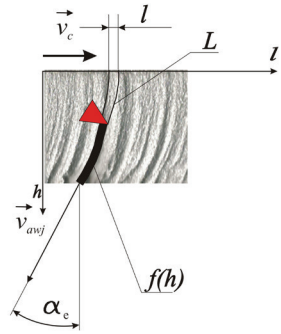

Fig. 3. Approximation of the abrasive water jet machining process

The volume of removed material can be calculated using Eq. (4).

$$V = L\,l\,w_m. \quad (4)$$

The mean width of the cut w_m is the mean value of w_{en} and w_{ex}, the width of cut at the entry of the AWJ into the material being machined and the width of the cut at the exit of the AWJ from the material, respectively:

$$w_m = \frac{w_{en} + w_{ex}}{2}. \quad (5)$$

The path of the cutting head, while the AWJ removes the material along a single striation (cut the forehead through the whole material thickness) is l, according to Fig. 3 it is equal to:

$$l = v_c t, \quad t = \frac{L}{v_{awj}}. \quad (6)$$

According to Eqs. (4) to (6), it follows that the volume of removed material V is:

$$V = L^2 w_m \frac{v_c}{v_{awj}}. \quad (7)$$

By substituting the equations for calculating the volume of removed material into Eq. (3), the equation for calculating the cutting force can be written in the form:

$$F = E_c L w_m \frac{v_c}{v_{awj}}. \quad (8)$$

In Eq. (8), the most influential factor is the traverse speed v_c. The dependence of the cutting force on the traverse speed can be approximately represented as linear. It can be concluded that with an increase in the traverse speed, there is an increase in the value of the cutting force, i.e. the vertical component of the cutting force. The biggest peak in the cutting force occurs when the material of the workpiece is not completely cut, because then the AWJ acts with its entire surface of the machined material.

According to Fig. 1 and Eq. (1), the vertical component of the cutting force, F_v, can be calculated by:

$$F_v = F\cos\alpha_e = E_c L w_m \frac{v_c}{v_{awj}}\cos\alpha_e. \quad (9)$$

where α_e is the angle of the tangent of the cut front line.

2.2 Experimental Setup for Cutting Force Measurement

The phenomenon that when the cutting with an abrasive water jet does not completely cut through the material, there occur extreme values in the cutting force signal (peaks) and pronounced roughness of the obtained cut surface imposes the need for specific research.

Accordingly, the research presented in this paper has focused on the connection between the dynamic character of cutting forces, peaks in the cutting force, and the appearance of irregularities and uncut parts on the machined surface while machining at high traverse speeds. The experimental measurements of the cutting force were carried out for the PTV-3.8/60 abrasive water jet machine with a KMT cutting head. The cutting was done over the water. The cutting force has been measured at traverse speeds around 1000 mm/min (much higher than usual). The maximum value of traverse speed at which a complete cut can be obtained (based on the KMT calculator) is 900 mm/min. Traverse speeds were chosen so to obtain a regular cut and a combination of regular and irregular cuts, but not complete uncut piece. Prior to the force measurement, a set of cuts was made with the same sample at different traverse speeds, from lower to higher, to determine the range of speeds that suits the purpose of the planned research. Thereafter, relevant set of cuts and cutting force measurement were done in the range of traverse speeds of interest. Other parameters of the machining process were constant during AWJ cutting of the samples: the operating pressure was 4130 bar, abrasive mass flow rate 350 g/min, standoff distance x_o was 3 mm and the abrasive was garnet mesh size 80. The water nozzle (orifice) diameter was 0.3 mm and focusing tube diameter was 1.02 mm.

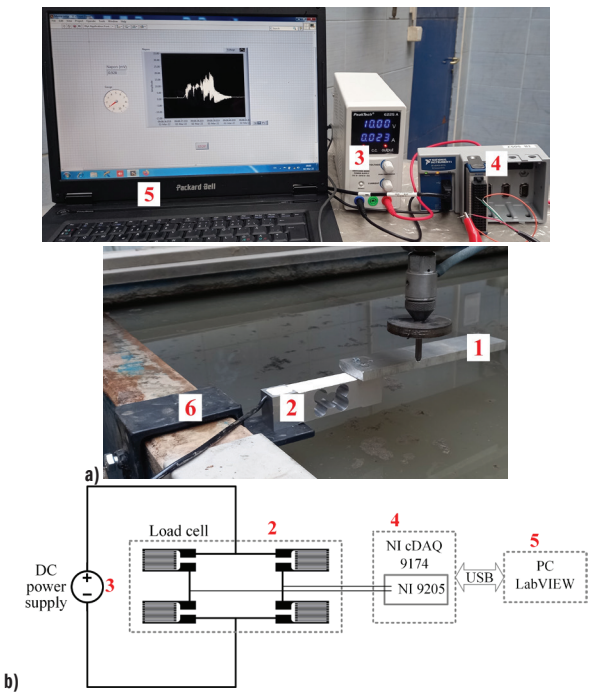

Fig. 4. Experimental setup for cutting force measurement: a) photograph of the components, b) block scheme of connections

The experimental setup for measurement of cutting force is based on a PC. It consists of the following equipment: 1) the test sample, fixedly mounted to 2) the load cell CZL623B (for 10 kg, up to approximately 100 N), 3) the direct current (DC) power supply for the load cell, 4) the data acquisition card NI 9205 (placed in the chassis NI cDAQ 9174) and 5) a PC with LabVIEW software. The load cell is fixed to 6) the steel carrier profiled so it fits well one side of the waterjet cutting machine. Fixed mounting of the carrier to the machine has been made with three large screws. A photograph of the equipment used is shown in Fig. 4a, and a block scheme of the connections is given in Fig. 4b.

The test sample is a 12 mm thick aluminium rod, 50 mm wide and 300 mm long. Aluminium is of ENAW-5754 (AlMg3) quality, the main alloying element is magnesium. Tensile strength of AlMg3 is in the range of 80 MPa to 280 MPa and Brinell Hardness (HB) from 52 to 88. It has been screwed to the load cell at one end by two screws and the other end was free. The material has been selected because of its often used in practice. The dimensions were chosen so to have a significantly long cutting path, and the thickness of the sample so as to obtain irregular cuts at higher speeds.

The load cell contains four strain gauges connected in full bridge (Fig. 4b). Its sensitivity is rated by the manufacturer at 2 mV/V for the mass of 10 kg, or in other terms it is 2mV/kg for 10 V supplied by the DC power supply. Thus, the output voltage would be 10 mV for 10 V of input voltage and 5 kilograms of the load. The data acquisition (DAQ) card NI 9205 is an analogue voltage input module of 16 bits resolution and 250 kS/s maximum sample rate (in samples per second). Its lowest input range is 200 mV. Thus, it is suitable for the measurement of low voltages from the load cell and is fast enough to observe transients. During the measurements, the DAQ card acquired 1200 S/s. This card has been inserted into a chassis NI cDAQ 9174 which provides the power supply for the card and a connection with a PC over the USB cable.

A standard DC laboratory supply of a stable DC voltage was used as the power supply for the load cell. The laptop computer was running LabVIEW 2014. A simple program for acquisition of the voltage generated at the output of the load cell has been created for the planned measurements. The program was set to continuous sample acquisition and writing the data to the computer memory.

Prior the measurements of the force of the abrasive water jet machine, the load cell was calibrated in the laboratory using precision weights and by measurement of the output voltage. The calibration has been performed using the measurement setup presented in Fig. 4b. The test sample 1, load cell 2 and steel carrier 6 were fixedly mounted to the laboratory table (similarly to Fig. 4a). Supplied DC voltage was set to 10 V. Laboratory weights of different masses, from 50 g to total 5000 g (about 49 N), were positioned on the test sample and the output voltage was recorded using the LabVIEW application. The measurement results obtained are graphically presented in Fig. 5, together with the linear fit of these data.

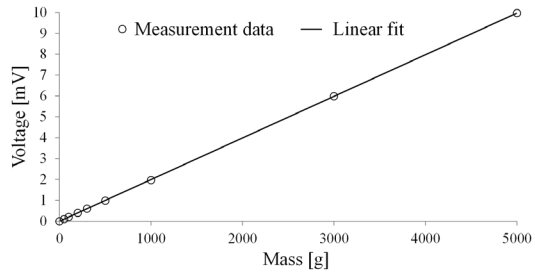

Fig. 5. Measurement data and linear fit obtained during the calibration of load cell

The slope of the linear fit is 2.001 mV/kg, which confirms the rated sensitivity of the load cell given by the manufacturer, which is 2 mV/kg.

The manufacturer also stated the accuracy of the load cell 2 % as 0.02 % of the full scale (10 kg), which is equal to 2 g of the absolute error in the whole measurement range. This corresponds to an absolute error of 4 μV at the maximal load cell output voltage (20 mV). The manufacturer of the DAQ NI 9205 stated the absolute error of 175 μV in the range of ±0.2 V.

The force F has been determined from the measured load cell output voltage u_{LC} as:

$$F = g\frac{u_{LC}}{S_{LC}} = 9.80665\frac{u_{LC}}{S_{LC}}, \tag{10}$$

where S_{LC} is the load cell sensitivity. The combined uncertainty $u_c(F)$ of force F measurement is defined according to the sensitivity coefficients, which are calculated as partial derivatives of F, and the absolute uncertainties of each independent variable, as in [16]:

$$u_c(F) = \sqrt{\left(\frac{\partial F}{\partial u_{LC}}\right)^2 u_{B,u_{LC}}^2 + \left(\frac{\partial F}{\partial S_{LC}}\right)^2 u_{B,S_{LC}}^2}, \tag{11}$$

where $u_X = |\partial F/\partial X| u_{B,X}$, $X \in \{u_{LC}, S_{LC}\}$ and $u_{B,u_{LC}}$, $u_{B,S_{LC}}$ are Type B standard uncertainty calculated by dividing corresponding absolute errors with $\sqrt{3}$, for a rectangular distribution with the confidence level of 95 %. Sensitivity coefficients are calculated for maximal voltage $u_{LC_{max}}$ and previously calculated S_{LC}. All calculated values are given in Table 1.

Table 1. Type B uncertainty for load cell calibration at 49 N (5 kg)

Variable	$u_{LC_{max}}$	S_{LC}
Value	9.968 mV	2 mV/kg
Absolute error	175 μV	0.4 μV/kg
Sensitivity coefficient	4903.3 N/V	−244382 kg/V
Absolute standard uncertainty u_X [N]	0.495	0. 056
Relative uncertainty [%]	1.014	0.115

The combined uncertainty value is 0.499 N and its relative value is 1.02 %. A correction factor k = 2 can be used for calculating the expanded uncertainty. In such a case, the confidence level is around 95 % and expanded uncertainty is 1.00 N or 2.04 %. The calculations need to be repeated to obtain the uncertainty for other values of the force (mass).

It should be noted that the measured values of the force are not the real ones because the cutting force is not developing coaxially to the load cell. However, this issue was not considered significant, as the bending of the steel carrier, load cell or sample was negligible, due to their robustness.

3 RESULTS AND DISCUSSION

The measurements of the cutting force have been performed at higher traverse speed to examine the relation between irregularities in the machined surface and the cutting force applied to the test sample made by the AWJ. Cuts have been performed in the longitudinal direction of the sample. The cuts were 100 mm long. One transversal cut has been made prior to all other cuts at lower speed (600 mm/min) as a trial case. Other cuts have been performed at four traverse speeds, namely: 900 mm/min, 950 mm/min, 1000 mm/min and 1100 mm/min.

A comparison of the forces obtained for 600 mm/min and 900 mm/min is presented in Fig. 6. Both traverse speeds are low enough that the cutting through the material is regular.

The light grey line in Fig. 6 represents the original measured data, whereas the blue and orange lines represent the smoothed measured data (obtained using the built-in function Smooth of OriginLab software). The force has the same level of 5 N before and after the cutting and it increases up to 15 N for the transversal cut and up to 18 N for the longitudinal cut. Thus, both directions can be used for observing the cutting force and the quality of cutting. The longitudinal cutting contains more pronounced oscillations in the force and even significant peaks in the range from 30 N to 40 N. All that is a consequence of the higher traverse speed.

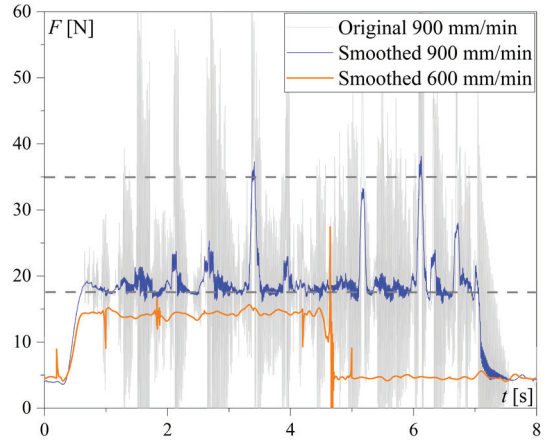

Fig. 6. Comparison of cutting force measured at lower (600 mm/min) and higher (900 mm/min) traverse speeds

Further analysis of the results will be focused on higher traverse speeds. The force profile for each of four cuts made will be discussed in detail. Photographs of the bottom and side view for each cut will be shown along with the force profile and their relation will also be discussed.

A profile of the cutting force for a traverse speed of 900 mm/min is presented in Fig. 7. The grey dashed lines represent the lower (17.5 N) and upper (35 N) cutting force limits chosen so that most of the measured data is within those limits when the cutting is correct. In Fig. 7, below the cutting force signal, there are photographs of the cut surfaces (orange box and black arrows) and a view from the underside of the cut sample (magenta box and black arrow). Green arrows and circles indicate cutting force peaks that are within (or slightly above) the upper and lower limits, which correspond to normal cutting or with irregularities of negligible size. In this case, the bottom view shows no irregularities in the cutting. Small irregularities can be seen in the side view, where the AWJ has created several cavities of small sizes. Their position corresponds to the position of the force peaks.

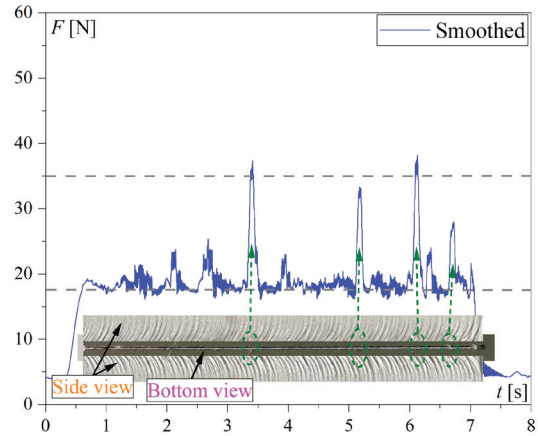

Fig. 7. Profile of cutting force for traverse speed of 900 mm/min, along with photographs of the cut

The profile of the cutting force for the next traverse speed of 950 mm/min is presented in Fig. 8. This slight increase in the traverse speed results in an increase in the number of peaks in the force profile. Still, the cutting is regular, as can be seen from the bottom view, but the number of cavities is evidently larger, and again it corresponds

well to the number of peaks. Also, the size of the cavities is larger than for the lower traverse speed.

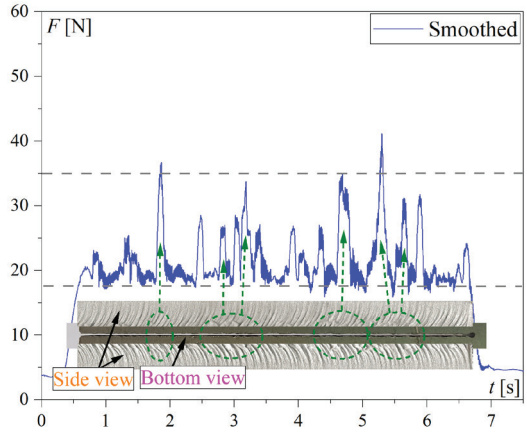

Fig. 8. Profile of cutting force for traverse speed of 950 mm/min, along with photographs of the cut

The profile of the cutting force for the third traverse speed of 1000 mm/min is presented in Fig. 9.

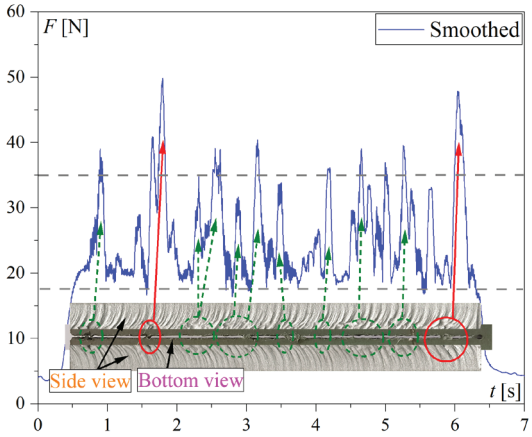

Fig. 9. Profile of cutting force for traverse speed of 1000 mm/min, along with photographs of the cut

The bottom view shows that the cutting is occasionally irregular, as there are several smaller uncut regions and regions with material remaining. Almost the whole cut is covered with cavities, as can be seen in the side view. Many smaller peaks appear in the force profile, as well as two larger peaks (marked with red arrows and circles). These two peaks appear in the places where the material remained uncut. The force reaches almost 50 N in those two cases. The number of smaller peaks above 35 N has increased from 2 in the previous two cases to 8 in this case.

Fig. 10 shows cavities on the machined surface for a traverse speed of 1000 mm/min. Small uncut triangles can also be observed. Cavities are formed when the material is not completely cut, so the AWJ reflects from the uncut material. AWJ, part of whose energy has been spent, turns into solid material, where due to insufficient energy, swirling of the AWJ and creation of cavities occurs. Jerman at al. [17] noticed this phenomenon in their study of the development of the cutting front in AWJ machining. This is due to the jet's redirection at the bottom of the cut and not a reduction in the intensity of the AWJ.

The profile of the cutting force for the last traverse speed of 1100 mm/min is presented in Fig. 11.

In this most extreme case, the cutting is mostly irregular (clearly visible in the bottom view). Some smaller or larger uncut regions exist, as well as regions with contiguous uncut parts. Two individual uncut parts in the left half have produced two individual peaks, while multiple uncut parts have produced multiple peaks (in the right side). The duration of the peak is proportional to the length of the uncut triangle. The force profile is such that the force is significantly higher than the lower limit during the whole cut. Again, force peaks reach 50 N and more for the uncut regions. Furthermore, multiple cavities can be observed in the side view of the region with multiple uncut parts. Some of the cavities are quite large and moved from the surface to the inside of the material (for up to one quarter of the thickness).

Fig. 10. Cavities on machined surface for traverse speed of 1000 mm/min

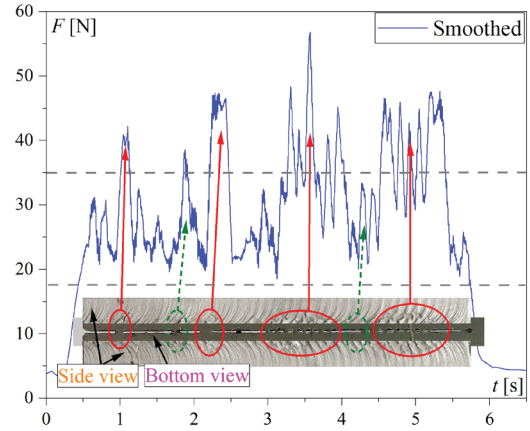

Fig. 11. Profile of a cutting force for traverse speed of 1100 mm/min, along with the photographs of the cut

A summary of the characteristic data related to all four traverse speeds is given in Table 2. It contains the following data: the traverse speed v_c, the cutting time t_c, the number of smaller peaks N_{ps}, the number of larger peaks N_{pl}, the number of uncut parts N_u and the maximum of the vertical force F_{vm} for the whole cut.

Table 2. Characteristic data for four cuts

v_c [mm/min]	t_c [s]	N_{ps}	N_{pl}	N_u	F_{vm} [N]
900	6.66	8	0	0	38.37
950	6.32	15	0	0	41.10
1000	6.00	18	3	2	49.78
1100	5.45	14	12	18	56.84

The results for the number of peaks and cuts and maximal force are related to the smoothed data. They depend slightly on the smoothing parameters, but without any significant changes in the nature of the overall force profile.

Previous research has shown that the cutting force increases with increase of the traverse speed in the range up to 100 mm/min [18], and up to 300 mm/min [19]. Also, in [5], it was shown, using the results of experiments on several different metals, that there is a connection between peaks in the value of the cutting force and uncut parts of the material.

Taking the data for traverse speed and peak of cutting force given in Table 2 and taking into account that the peak of the cutting force amounted to around 15 N for the speed of 600 mm/min (see Fig. 6), a variation of the cutting force with the traverse speed has been presented graphically in Fig. 12. All values of the force are reduced by the force made by the test sample (around 4.5 N), which exists before and after the cutting (Figs. 6 to 11).

The measured data (black dots) have been fitted with a linear function, and the result obtained is presented by a dashed blue line, along with the data. The result in Fig. 12 confirms linear relationship given by Eq. (8), when considering the cutting force peak and the traverse speed. The linear dependence of the cutting force on the cutting depth and feed also exists in conventional cutting machining [20]. When machining with AWJ, cutting depth and feed depend on traverse speed.

This simplified model could be useful for application in the practice. However, such a linear relation should be investigated experimentally also for other materials and parameters of AWJ process. Also, the relationship of the cutting force and other input parameters needs to be investigated to improve overall knowledge about AWJ process and obtain other useful calculation tools. This was out of the scope of this paper and might be a subject of a future research in this field.

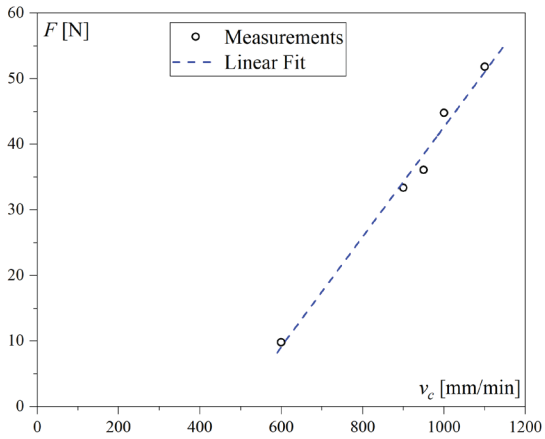

Fig. 12. Variation of cutting force with traverse speed

4 CONCLUSIONS

This paper presents the results obtained by experimental measurement of the vertical component of the cutting force, showing that measuring the vertical component of the cutting force makes it possible to observe a period when the machined material is not completely cut. Also, online measurements of the cutting force can be used for the evaluation of the quality of the machined surface.

The experimental results allow concluding that an increase of the traverse speed, above a certain limit, results in the appearance of irregularities in the cut and in an increase of the vertical component of the cutting force. Even when the cut is regular, such as for speeds of 900 mm/min and 950 mm/min, the maximum values of the vertical component of the cutting force can be more than two times larger than the lower limit. In the case of higher traverse speeds, when irregular cuts appear, the maximum values of the vertical component of the cutting force can be more than three times larger than the lower limit.

Beside the appearance of the uncut parts, smaller or larger cavities are produced in the material during cutting at high traverse speeds. These cavities significantly increase the roughness of the machined surface. Such unwanted side effects would require additional treatment of the machined surface after cutting. It can influence the quality of the final product.

The results of the conducted experiment can also be used for a better understanding of the material cutting process performed with the AWJ. There can be established a relation between the duration of the cutting force peak and the length of the uncut part, as well as their frequency. Also, based on the appearance of peaks in the profile of the vertical component of the cutting force, the beginning of cutting with an unsatisfactory quality of the machined surface can be determined.

In conventional cutting, increasing the auxiliary speed (feed) causes an increase in the cross-sectional area of the chip, and therefore the volume of the removed material, which further leads to an increase in the value of the cutting force. In this paper, machining with abrasive water jet is viewed as a classic cutting process. The abrasive water jet is represented as a cutting tool, while the cross-sectional area of material removed per unit of time is represented as a cross-sectional area of the chip. By applying the formulas valid for conventional cutting procedures, a new model was obtained for the calculation of the cutting force during machining with an abrasive water jet. This model is much simpler than the models presented in previous research by other authors. In AWJ machining, traverse speed is most often varied in practice, while operating pressure and abrasive mass flow rate are less frequently changed. In these conditions, the model presented in the paper shows that there is a linear relation between the traverse speed and cutting force. With the increase of traverse speed, there is an increase in the cross-sectional area of the chip, and therefore the volume of the removed material. This further leads to an increase in the value of the cutting force. Measurements have shown that with an increase in the traverse speed, there is an increase in the value of the cutting force, which confirmed these assumptions. To determine the cutting force for a given material and machining parameters, it is necessary to determine the specific cutting energy, which can be the subject of further research. Also, future research can deal with the influence of the operating pressure and mass flow rate on the values of the cutting force.

AWJ requires a much larger number of input parameters than considered in the conducted research. However, the focus was given to the traverse speed as input parameter and the cutting force as the output parameter to validate the model under specific conditions. It was of a particular importance to investigate if the direct proportionality of the simplified model still remains valid at higher speeds.

To apply the conclusions presented in this paper to the current manufacturing of parts using abrasive water jet technology, it is essential to develop specialized cutting tables. These tables should facilitate online monitoring of cutting force values, which could also be a subject for further research.

REFERENCES

[1] Shin, B.S., Park, K.S., Bahk, Y.K., Park, S.K., Lee, J.H., Go, et al. Rapid manufacturing of SiC moulds with micro-sized holes using abrasive water jet *T Nonferr Metal Soc* 19 S1, 178-182 (2009) **DOI:10.1016/S1003-6326(10)60267-1**

[2] Savrun, E., Taya, M. Surface characterization of SiC whisker/2124 aluminium and Al203 composites machined by abrasive water jet *J of Mater Sci* 23 1453-1458, (1988) **DOI:10.1007/BF01154616**

[3] Omax. About waterjets. *www.omax.com/en/us*, accessed on: 2024-08-09

[4] Hlaváč, L.M., Annoni, M.P.G., Hlaváčová, I.M., Arleo, F., Viganò, F., Štefek, A. Abrasive waterjet (AWJ) forces - Potential indicators of machining quality *Materials* 14 3309 (2021) **DOI:10.3390/ma14123309**

[5] Hlaváč, L.M., Bańkowski, D., Krajcarz, D., Štefek, A., Tyč, M., Młynarczyk, P. Abrasive waterjet (AWJ) forces - Indicator of cutting system malfunction *Materials* 14 683 (2021) **DOI:10.3390/ma14071683**

[6] Pahuja, R., Ramulu, M. Abrasive waterjet process monitoring through acoustic and vibration signals. *Proceedings of 24th International Conference on Water Jetting*, (2018) p. 75-87

[7] Kinik, D., Ganovska, B., Hloch, S., Monka, P., Monkova, K., Hutyrova, Z. On-line monitoring of technological process of material abrasive water jet cutting. *Teh Vjesn* 22 351-357 (2015) **DOI:10.17559/TV-20130904111939**

[8] Karakurt, I., Aydin, G., Aydiner, K. A machinability study of granite using abrasive waterjet cutting technology. *Gazi Univ J Sci* 24, p. 143-151 (2011)

[9] Kovacevic, R., Mohan, R., Zhang, Y.M. Cutting force dynamics as a tool for surface profile monitoring in abrasive waterjet *J Eng Ind-T ASME* 117 340-350 (1995) **DOI:10.1115/1.2804339**

[10] Hassan, A.I., Chen, C., Kovacevic, R. On-line monitoring of depth of cut in AWJ cutting *Int J Mach Tool Manu* 44 595-605 (2004) **DOI:10.1016/j.ijmachtools.2003.12.002**

[11] Kovacevic, R. Monitoring the depth of abrasive waterjet penetration *Int J Mach Tool Manu* 32 725-736 (1992) **DOI:10.1016/0890-6955(92)90026-D**

[12] Orbanić, H., Junkar, M., Bajsić, I., Lebar, A. An instrument for measuring abrasive water jet diameter *Int J Mach Tool Manu* 49 843-849 (2009) **DOI:10.1016/j.ijmachtools.2009.05.008**

[13] Momber, A.W. Energy transfer during the mixing of air and solid particles into a high-speed waterjet: An Impact force study *Exp Therm Fluid Sci* 25 31-41 (2001) **DOI:10.1016/S0894-1777(01)00057-7**

[14] Baralić, J., Nedić, B. The influence of abrasive water jet processing parameters on reaction force. *Proceedings of 12th International Scientific Conference MMA* p. 25-28 (2015)

[15] Hashish, M. A modelling study of metal cutting with abrasive waterjets *J Eng Mater-T ASME* 106 88-100 (1984) **DOI:10.1115/1.3225682**

[16] JCGM 100. *Evaluation of Measurement Data. Guide to the Expression of Uncertainty in Measurement*. Joint Committee for Guides in Metrology (2008)

[17] Jerman, M., Valentinčič, J., Lebar, A., Orbanić, H. The study of abrasive water jet cutting front development using a two-dimensional cellular automata model. *Stroj Vestn-J Mech E* 61 292-302 (2015) **DOI:10.5545/sv-jme.2014.2179**

[18] Grundel, J., Hlaváč, L.M., Petroš, P., Gembalová L. Analysis of several physical phenomena measured on the metallic materials cut by abrasive water jets (AWJ). *Materials* 15 7423 (2022) **DOI:10.3390/ma15217423**

[19] Wala, T., Lis, K. Influence of selected diagnostic parameters on the quality of AWJ cutting surface. *Adv Sci Tech Res J* 16 129-140 (2022) **DOI:10.12913/22998624/144642**

[20] Struzikiewicz, G. Investigation of the titanium alloy turning process with prime a tools under high-pressure cooling conditions. *Stroj Vestn-J Mech E* 70 70-79 (2024) **DOI:10.5545/sv-jme.2023.718**

Acknowledgements This study was supported by the Ministry of Science, Technological Development and Innovation of the Republic of Serbia, and these results are parts of the Grant No. 451-03-66/2024-03/200132 with University of Kragujevac - Faculty of Technical Sciences Čačak, Serbia.

Received 2024-04-02, revised 2024-08-19, accepted 2024-11-05
Original Scientific Paper

Data Availability The data that support the findings of this study are available from the corresponding author upon reasonable request.

Author Contribution Conceptualization, J.B. and B.K.; methodology, J.B., S.P.S. and B.K.; software, B.K. and S.Đ.; validation, J.B., S.P.S., S.Đ. and B.K.; formal analysis, B.K., J.B., S.P.S. and S.Đ.; investigation, J.B. and B.K.; resources, J.B., S.Đ. and S.P.S.; writing – original draft, J.B., B.K. and S.P.S.; writing – review and editing, J.B. and B.K.; visualization, J.B., B.K., S.P.S. and S.Đ.; supervision, J.B. and B.K. All authors have read and agreed to the published version of the manuscript.

Povezava med dinamičnim značajem rezalne sile in obdelano površino pri obdelavi z abrazivnim vodnim curkom

Povzetek V članku so predstavljeni rezultati raziskave o vplivu hitrosti premikanja na rezalne sile in obdelano površino pri obdelavi z abrazivnim vodnim curkom. Rezultati so pokazali, da obstaja pomembna povezava med dinamičnim značajem rezalne sile pri obdelavi z abrazivnim vodnim curkom, natančneje med vrhovi v signalu rezalne sile, ter pojavom nepravilnosti in nerazrezanih delov na obdelani površini. Prav tako je raziskava pokazala, da povečanje hitrosti pomikanja povzroči povečanje srednje vrednosti statične komponente rezalne sile. V eksperimentih je bila izmerjena navpična komponenta rezalne sile za 12 mm debelo palico iz aluminija AlMg3, rezano s hitrostmi premikanja od 900 mm/min do 1100 mm/min. Pri rezanju z večjimi hitrostmi se pojavijo večje nepravilnosti, ki so povezane s pojavom vrhov v izmerjeni rezalni sili.

Ključne besede abrazivni vodni curek, rezalna sila, prečna hitrost, obdelana površina

A Mathematical Model of the Dimensional Chain for a Generation 2 Wheel Hub Unit

Stanisław Adamczak[1] – Marek Gajur[2] – Krzysztof Kuźmicki[2] ✉

1 Kielce University of Technology, Department of Mechatronics and Mechanical Engineering, Poland
2 Fabryka Łożysk Tocznych Kraśnik S.A., Poland

✉ kkuzmicki@flt.krasnik.pl

Abstract *This article overviews wheel hub design solutions and proposes a mathematical model of the dimensional chain and a tolerance formula for calculating axial clearance for a generation 2 wheel hub assembly with ball bearings. The dimensional chain analysis and its synthesis are carried out using three partial interchangeability methods. The possibility of manufacturing the hub bearing using selection compensation was proposed. The considerations made provide an alternative to the current method of process design based on numerous trials and considerable cost.*

Keywords *rolling-element bearings, dimensional chain, tolerance formula, axial clearance, wheel hub unit*

Highlights

- *A mathematical model of the dimensional chain and the tolerance equations for axial clearance was developed.*
- *Axial clearance and its limit deviations were compared to the constructor's values, revealing significant discrepancies.*
- *Calculations for component dimension tolerances show that achieving partial interchangeability in production is not feasible.*
- *Calculated tolerances of independent dimensions using selection compensation into 9 selection groups.*

1 INTRODUCTION

The main objective of this paper is to present an approach to the design of manufacturing processes using a mathematical model of the dimensional chain to achieve the expected axial clearance. In previous practice when designing bearing hubs, designers did not build mathematical models of dimensional chains. Tolerances were selected intuitively based on the knowledge and experience of the designer. They were often suboptimal and economically unjustified. Therefore, work was undertaken to build a mathematical model of the dimensional chain of the axial clearance of a second-generation ball bearing hub assembly, in order to use it to verify the hub design and to plan the optimal manufacturing process. The hypothesis was made that in cases where the tolerance values obtained using the model would be less than the tolerances adopted by the designer, it would be necessary to change the tolerances of the independent dimensions and manufacture the product under interchangeable conditions using a selective compensation approach.

Tolerance design is very important in product development and manufacturing processes. It is particularly important when applying the concept of concurrent engineering (CE). This ensures that manufacturing costs are minimised with maximum product quality [1]. Many articles address the issues of tolerancing the dimensions of independent parts as well as assembling them into assemblies with the indication of problems in building tolerance chain models [2]. Singh et al [3] and [4] characterise various studies and theories on tolerance analysis and synthesis, which can be divided into traditional and advanced ones. Traditional tolerance design approaches do not consider the impact of tolerance on manufacturing cost as opposed to advanced ones. The authors of the theoretical considerations have not supported their application in industry with examples. Tolerance optimisation for products with multidimensional chains was described by Tsung [5] using the example of a ball bearing incorporated into a bicycle bottom bracket using specialised software. Nonetheless, the measurement of components at the manufacturing stage and their association at the assembly stage do not reflect the problems of determining the independent dimensional tolerances themselves.

There are many methods of tolerance analysis in use today, both manual and software-based. The use of computer software is constantly being developed and the results obtained can be used for analysis and optimal design [6] and [7]. In this paper, however, manual methods have been used to determine the dimensional chain model, perform its analysis and synthesise it for the axial clearance of a generation II hub.

Fig. 1. Wheel hub unit with two tapered roller bearings

Bearing hubs have undergone extensive modifications over the years in order to reduce their manufacturing costs and meet market expectations. Decisions made at the design stage help minimize the

DOI: 10.5545/sv-jme.2024.1020

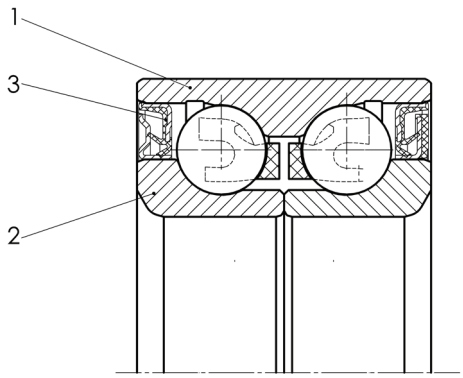

Fig. 2. Generation I wheel hub unit with a double-row angular contact ball bearing; 1 outer ring, 2 inner ring, and 3 seal

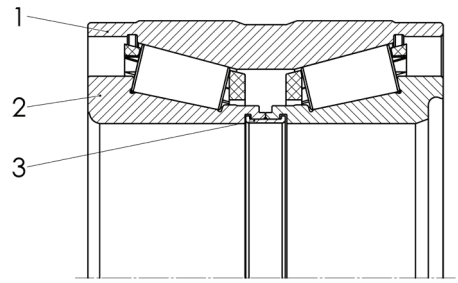

Fig. 3. Generation I wheel hub unit with a double-row tapered roller bearing; 1 outer ring, 2 inner ring and 3 clamping ring

risks of product failure, which may result from errors associated with drawing interpretation, product manufacturing, or its primary or secondary assembly. The major factors responsible for these errors are the designer's insufficient knowledge of the processes involved in the manufacturing of the product and a low level of mechanization or automation of the product assembly [8]. Designers making decisions on tolerance sizes generally rely on intuition and experience. Such an approach, however, may not be correct because if tolerances are too small, the manufacturing costs increase substantially.

Wheel hub units for motor vehicles are precision products where appropriate dimensioning and tolerancing of components are critical aspects of engineering design. The simplest wheel hub unit configuration, depicted in Fig. 1, features a pair of tapered roller bearings in an adjusted face-to-face preload arrangement.

Another design solution is the first-generation wheel hub unit, fitted with a double-row angular contact ball bearing (Fig. 2) or a double-row tapered roller bearing (Fig. 3), lubricated for life with defined and preset clearance.

The second generation unitized or integrated wheel hub unit illustrated in Fig. 4 is a solution in which the bearing housing is replaced by an outer ring with a flange to which the rotating parts of the brake system and the road wheels are attached. It comes in two variants based either on the ball bearing or tapered roller bearing designs [9].

A more technologically advanced solution is the third-generation wheel hub unit with ball or tapered roller bearings (Fig. 5), where the outer flanged ring (1) takes over the function of the housing, and the inner flanged ring (2) allows the attachment of the brake disc and the road wheel. The wheel hub unit design has undergone various modifications to suit specific purposes. For example, the unit shown in Fig. 6 features a torque transmission gear system with an inner flanged ring (2) and a halfshaft gear (3).

When designing wheel hub units, engineers need to determine the tolerance limit for each toleranced dimension. This requires

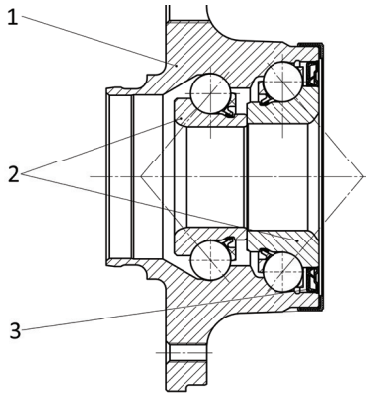

Fig. 4. Generation II wheel hub unit based on the ball bearing design; 1 outer flanged ring, 2 inner rings, and 3 seal

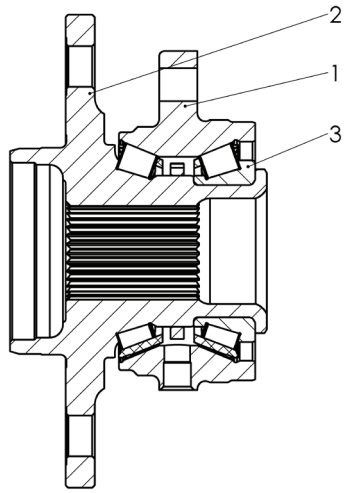

Fig. 5. Generation III wheel hub unit based on the tapered roller bearing design; 1 outer flanged ring, 2 inner flanged ring and 3 standard inner ring

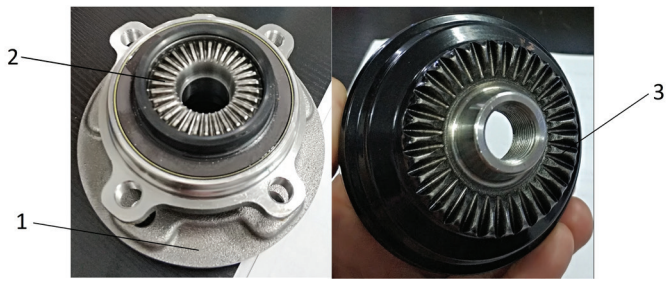

Fig. 6. Generation III wheel hub unit with a torque transmission gear system; 1 outer flanged ring, 2 inner flanged ring with a face gear and 3 halfshaft gear with meshing teeth

robust design knowledge and previous experience. They also analyze all the relevant measurement and simulation data. In some cases, however, tolerances assumed by the designer may not ensure that parts will function correctly [10]. Measurement methods used at the manufacturing stage play an essential role [11] and [12]. These days, geometrical tolerances can also be used to precisely define the product, such as for the design of gears [13]. This methodology, called geometrical product specification (GPS), described by EN ISO 8015:2012 [14] and ISO 492:2014 [15] has supplemented the traditional techniques for determining the geometrical requirements of engineering products. GPS helps specify linear and angular dimensional tolerances, geometrical tolerances, and surface texture tolerances [16] and [17].

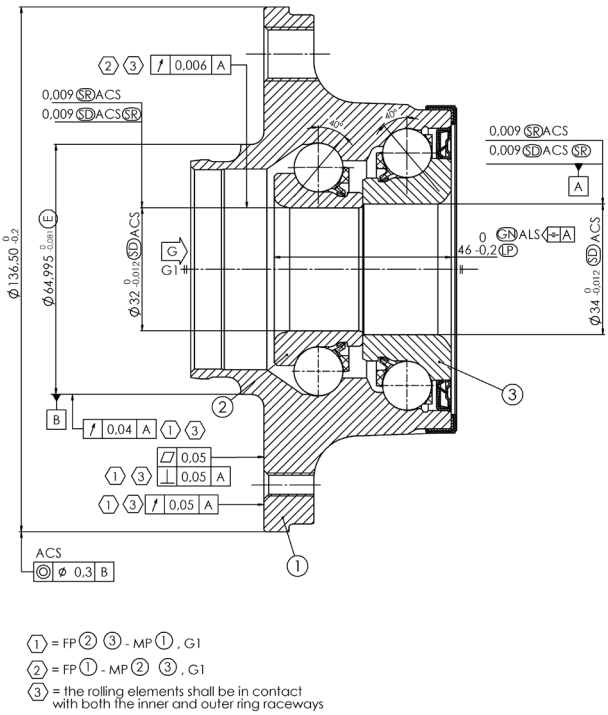

Fig. 7. Generation II wheel hub unit with a double-row angular contact ball bearing

In the study, the GPS dimensioning principles were employed to develop the design of a second generation wheel hub unit incorporating a double-row angular contact bearing (Fig. 7) [18].

2 A MATHEMATICAL MODEL

A mathematical model of the tolerance formula for the axial clearance of the generation 2 wheel hub unite with a double-row angular contact ball bearing is presented. The components of a double-row angular contact bearing, such as the inner rings, the outer ring, and the balls need to be carefully selected to ensure correct axial and radial clearance. In practice, however, for this type of bearing, only the axial clearance is measured under axial load, which is exerted in the axial direction on the outer ring alternately on either face, with the inner rings held stationary.

Assuming zero axial load, we obtained a dimensional chain with 14 components:

- m is axial distance between the raceways of the outer ring,
- n_l axial distance between the raceway of the left inner ring and its narrow face,
- n_p axial distance between the raceway of the right inner ring and its narrow face,
- r_{wl} radius of the left inner ring raceway,
- r_{wp} radius of the right inner ring raceway,
- r_{zl} radius of the left outer ring raceway,
- r_{zp} radius of the right outer ring raceway,
- d_{wl} diameter of the left inner ring raceway,
- d_{wp} diameter of the right inner ring raceway,
- d_{zl} diameter of the left outer ring raceway,
- d_{zp} diameter of the right outer ring raceway,
- α contact angle,
- d_l diameter of the left raceway ball,
- d_p diameter of the right raceway ball.

Thus, the dimensional chain equation for axial clearance is a function [19]:

$$L = f(m, p_l, p_p, r_{wl}, r_{wp}, r_{zl}, r_{zp}, d_{wl}, d_{wp}, d_{zl}, d_{zp}, \alpha, d_l, d_p).$$

Because of the symmetry, the number of dimensions was reduced to half. Thus, the dimensional chain was simplified to an eight-component chain. The function had the form:

$$L = f(m, n, r_w, r_z, d_w, d_z, \alpha, d),$$

where m is axial distance between the raceways of the outer ring, n axial distance between the raceways of the inner rings, r_w radius of the inner ring raceway, r_z radius of the outer ring raceway, d_w diameter of the inner ring raceway, d_z diameter of the outer ring raceway, α contact angle, and d ball diameter. In the study, a simplified design of the wheel hub unit (Fig. 8) was considered.

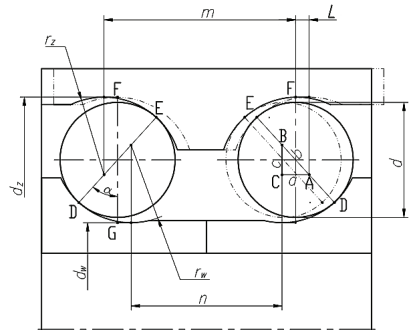

Fig. 8. Simplified design of the wheel hub unit with a double-row angular contact ball bearing

The dimensional chain equation for the axial clearance was written as:

$$m = n + 2a - L. \quad (1)$$

Hence,

$$L = n - m + 2a, \quad (2)$$

$$a = \sqrt{b^2 - c^2}, \quad (3)$$

$$b = r_w + r_z - d, \quad (4)$$

$$c = r_w + r_z - 0.5(dz - dw), \quad (5)$$

$$a^2 = (r_w + r_z - d)^2 - (r_w + r_z - 0.5(d_z - d_w))^2. \quad (6)$$

Let

$$R = r_w + r_z \quad \text{and} \quad S = 0.5(d_z - d_w). \quad (7)$$

After substituting Eq. (7) into Eq. (6), we obtaine

$$a^2 = (R - d)^2 - (R - S)^2, \quad (8)$$

and after the conversion, we had

$$a^2 = (d - S)(d + S - 2R). \quad (9)$$

The equation of the dimensional chain for the axial clearance was thus given as

$$L = n - m + 2\sqrt{(d - S)(d + S - 2R)}. \quad (10)$$

The tolerance formula was derived using the partial interchangeability method. It was assumed that the coefficient of variation for all the components of the dimensional chain was equal to 1. The tolerance formula for this complex chain was determined from Eq. (11):

$$T_L^2 = \sum_{i=1}^{k-1} \left(\frac{\partial L}{\partial A_i} \right)^2 TA_i^2. \quad (11)$$

The partial derivatives were calculated as:

$$\frac{\partial L}{\partial n} = 1, \quad \frac{\partial L}{\partial m} = -1, \quad (12)$$

$$\frac{\partial L}{\partial d} = \frac{2(d - R)}{\sqrt{(d - S)(d + S - 2R)}}, \quad (13)$$

$$\frac{\partial L}{\partial S} = \frac{2(R - S)}{\sqrt{(d - S)(d + S - 2R)}}, \quad (14)$$

$$\frac{\partial L}{\partial R}=\frac{2(S-d)}{\sqrt{(d-S)(d+S-2R)}}. \quad (15)$$

Since

$$\beta=\sqrt{(d-S)(d+S-2R)}, \quad (16)$$

the tolerance equation took the following form:

$$T_L^2=T_n^2+T_m^2+\frac{4}{\beta^2}\left[(d-R)^2T_d^2+(R-S)^2T_S^2+(S-d)^2T_R^2\right], \quad (17)$$

$$T_L=\sqrt{T_n^2+T_m^2+\frac{4}{\beta^2}\left[(d-R)^2T_d^2+(R-S)^2T_S^2+(S-d)^2T_R^2\right]}. \quad (18)$$

3 VALIDATION OF THE MATHEMATICAL MODEL

In this paper, the validation of the mathematical model of the axial clearance dimension chain is reduced to analysis and synthesis to confirm that the equation is mathematically and physically correct and meets the specified functional requirements.

The nominal value of the axial clearance in the analysed wheel hub unit was calculated using Eq. (18), derived under the assumption of partial interchangeability. The assumption was made because there were eight components in the dimensional chain and the designer's past experience in the design and production of similar products indicated such an approach was correct. Table 1 summarizes the nominal values of the dimensions shown in Fig. 8 together with their tolerances.

Table 1. Nominal values and tolerances determined for the dimensions provided in Fig. 8

Dimension	Unit	Nominal value	Tolerance
$n=n_I+n_p$	[mm]	22.772	± 0.020
m	[mm]	23.488	± 0.010
r_z	[mm]	6.730	± 0.025
r_w	[mm]	6.540	± 0.025
d	[mm]	12.700	± 0.00975
α	[°]	40	-
d_z	[mm]	65.878	± 0.02
d_w	[mm]	40.211	± 0.02
L	[mm]	0.015	± 0.010

Due to the complex nature of the eight-component dimensional chain, small tolerances, and measurement difficulties, the tolerance of the contact angle α was assumed to be zero.

3.1 Dimensional Chain Analysis

Eq. (7) was used to calculate the values of R and S with tolerances.

$R=6.54^{\pm0.025}+6.73^{\pm0.025}=13.27^{\pm0.05}$ mm,

$S=0.5(65.878^{\pm0.02}-40.211^{\pm0.02})=12.834^{\pm0.02}$ mm.

The numerical values from Table 1 and the calculated values of R and S from Eq. (7) were substituted into Eq. (10) to get the nominal value of the axial clearance, L = 0.0183 mm

$$L=22.772-23.488+2\times\sqrt{(12.7-12.834)(12.7-12.834-26.54)}=0.0133 \text{ mm}.$$

The method of differential calculus, Eqs. (19) and (20), was employed to calculate the limit deviations.

$$x_2=\sum_{i=1}^{k}\frac{\partial L}{\partial A_i}a_{2i}+\sum_{i=1}^{n}\frac{\partial L}{\partial B_i}b_{1i}, \quad (19)$$

$$x_1=\sum_{i=1}^{k}\frac{\partial L}{\partial A_i}a_{1i}+\sum_{i=1}^{n}\frac{\partial L}{\partial B_i}b_{2i}. \quad (20)$$

Then, the values of the partial derivatives were determined using Eq. (12 to 15) and Eq. (16) in order to calculate β.

$$\beta=\sqrt{(12.7-12.834)(12.7+12.834-26.64)}=0.3672.$$

Thus

$$\frac{\partial L}{\partial d}=\frac{2(12.7-13.27)}{0.3672}=-3.105,\quad \frac{\partial L}{\partial S}=\frac{2(13.27-12.837)}{0.3672}=2.375,$$

$$\frac{\partial L}{\partial R}=\frac{2(12.834-12.7)}{0.3672}=0.73.$$

The upper limit deviation x_2 was:

$x_2=0.02+2.375\times0.02+0.73\times0.05+0.01+(-3.105)\times(-0.00975)$

$=0.144$ mm,

while the lower limit deviation x_1 was:

$x_1=-0.02+2.375\times(-0.02)+0.73\times(-0.05)-0.01$

$+(-3.105)\times0.00975=-0.144$ mm.

The axial clearance determined from the tolerances of the components of the dimensional chain assumed by the designer was:

$L=0.0183^{\pm0.144}$ mm

(with $L=0.015^{\pm0.010}$ mm assumed by the designer).

As can be seen, the calculated axial play was 3.3 µm greater than that assumed by the designer. The calculated tolerance value did not correspond to the nominal value of the axial clearance.

3.2 Synthesis of the Dimension Chain

The tolerances of the component dimensions were calculated for partial interchangeability using the method of equal tolerance, equal tolerance class and equal influence [20]. The experience of bearing manufacturers shows that performing these calculations for total interchangeability gives tolerance results of independent dimensions so small that it is not possible to meet them during technological process execution.

3.2.1 Method of Equal Tolerance

By substituting the numerical data into the tolerance equation; Eq. (18) and assuming $T_n=T_m=T_d=T_S=T_R=T$ the result was obtained:

$$T_L=\sqrt{T_n^2+T_m^2+\frac{4}{\beta^2}\left[(d-R)^2T_d^2+(R-S)^2T_S^2+(S-d)^2T_R^2\right]}$$

$$=\sqrt{T^2+T^2+\frac{4}{\beta^2}\left[(d-R)^2T^2+(R-S)^2T^2+(S-d)^2T^2\right]}$$

$$=T\sqrt{2+\frac{4}{\beta^2}\left[(d-R)^2+(R-S)^2+(S-d)^2\right]}$$

$$=T\sqrt{2+\frac{4}{0.135}[0.325+0.19+0.018]},$$

$$T=\frac{0.02}{4.218}=0.005 \text{ mm}.$$

3.2.2 Method of Equal Tolerance Class for a Complex Chain

Eqs. (21) and (22) were used to calculate tolerances using the equal tolerance class method.

$$k_L^2T_L^2=a^2\sum_{i=1}^{n-1}k_{A_i}^2\left(\frac{\partial L}{\partial A_i}\right)^2\left(\sqrt[3]{A_i}\right)^2, \quad (21)$$

$$T_{A_i}=a\sqrt[3]{A_i}. \quad (22)$$

By substituting the values from Table 1 into Eq. (22), the results were:

$T_n=2.834a$, $T_m=2.862a$, $T_d=2.333a$, $T_S=2.341a$, $T_R=2.368a$.

After substitution into Eq. (21), the following was obtained

$$T_L^2 = a^2(1\times2.834^2+1\times2.862^2+9.641\times2.333^2+5.641\times2.341^2 + 0.533\times2.368^2) = a^2\times102.6, \text{ hence,}$$

$$a = \frac{T_L}{\sqrt{102.6}} = 0.00197 \text{ mm.}$$

So the tolerances of the component dimensions are respectively: T_n=0.006 mm, T_m=0.006 mm, T_d=0.005 mm, T_S=0.005 mm, and T_R=0.005 mm.

3.2.3 Method of Equal Impact

Based on Eq. (23) for the composite chain and assuming that the components of the chain have a normal distribution i.e. k = 1, the result was obtained:

$$k_{A_1}^2\left(\frac{\partial L}{\partial A_1}\right)^2 T_{A_1}^2 = k_{A_2}^2\left(\frac{\partial L}{\partial A_2}\right)^2 T_{A_2}^2 = \ldots = k_{A_n}^2\left(\frac{\partial L}{\partial A_n}\right)^2 T_{A_n}^2 = m^2. \quad (23)$$

hence $T_{A_n} = \sqrt{\frac{m^2}{\left(\frac{\partial L}{\partial A_n}\right)^2}} = \frac{m}{\left|\frac{\partial L}{\partial A_n}\right|}$.

For five dimensions of the chain $T_L^2 = 5\times m^2$,

hence $m = \frac{T_L}{\sqrt{5}} = \frac{0.02}{2.236} = 0.009$ mm.

The tolerances of the individual dimensions are therefore T_n=0.009 mm, T_m=0.009 mm, T_d=0.003 mm, T_S=0.004 mm, and T_R=0.012 mm.

Table 2. Summary of results for three methods of calculating tolerances for partial interchangeability

Tol. specified by constructor		Tol. calculated using the equal tolerance method	Tol. calculated using the equal tolerance class method	Tol. calculated using the equal impact method
T_n [mm]	0.04	0.005	0.006	0.009
T_m [mm]	0.02		0.006	0.009
T_d [mm]	0.0195		0.005	0.003
T_S [mm]	0.04		0.005	0.004
T_R [mm]	0.10		0.005	0.012

Table 2 summarises the results for the three methods mentioned above and the values adopted by the designer. No calculations have been made for the minimum cost method because the cost functions of making the rings as a function of changes in the dimension chain values are not known.

3.3 Partial Interchangeability for Axial Clearance with Selective Compensation

For small tolerances of the dependent dimension, it often turns out that the tolerances of the independent dimensions determined under the assumption of partial interchangeability are very small. Meeting them results in a significant increase in manufacturing costs or is even impossible. In turn, their enlargement generates an unacceptable number of defects. In such cases, the most economical solution is to make the individual parts within the tolerances achievable under the given production conditions. The tolerance of the dependent dimension will then be bigger than the tolerance assumed by the designer, and additional work must be done during assembly to achieve the resulting dimension within the assumed limits. This kind of interchangeability, in which additional operations are needed to obtain the correct product, is called conditional interchangeability. One of its types is the selection of parts with the right dimensions - selection compensation. It involves measuring all the parts to be made and dividing them into several dimensional groups and associating them appropriately together with the rolling elements during assembly [21] In the case of selection interchangeability, dividing all the parts from a given lot into m selection groups allows their production tolerance to be increased m times. We can therefore write that the actual closure dimension tolerance T_L' is equal to the product of the number of selection groups m and the closure dimension tolerance in a given selection group T_L [22].

$$T_L' = m\times T_L. \quad (24)$$

For dimension chains with multiple dimensions, they should be divided into two chains I and II, trying to obtain an equal sum of the tolerances of their component dimensions using Eq. (25).

chain I chain II

$$\sum_{i=1}^{p}\left|\frac{\partial L}{\partial A_i}\right|T_{A_i} = \sum_{i=p+1}^{m}\left|\frac{\partial L}{\partial A_i}\right|T_{A_i}, \quad (25)$$

where p is the number of component dimensions of one of the two chains obtained from splitting the chain under consideration, and m the number of independent dimensions of the chain under consideration.

In the case of the wheel hub unit under consideration for the axial clearance tolerance equation this looks like the following:

$$\frac{\partial L}{\partial n}T_n + \frac{\partial L}{\partial S}T_S = \frac{\partial L}{\partial m}T_m + \frac{\partial L}{\partial d}T_d + \frac{\partial L}{\partial R}T_R.$$

The equality of parts I and II of the chains could not be achieved, as the following calculation illustrates.

$1\times0.04+2.375\times0.04 \approx 1\times0.02+3.105\times0.0195+0.73\times0.1,$

$0.135 \text{ mm} \neq 0.154 \text{ mm}.$

Actual tolerance of the closing dimension T_L'=0.135+0.154= 0.289 mm, and the desired tolerance is T_L=0.020 mm.

In order to meet the condition that the tolerance in a selection group should not be greater than the tolerance of the closing dimension using Eq. (24), the number of selection groups was calculated, which should be no less than 15 [22]:

- executive deviations: x_2'=0.144 mm and x_1'=–0.144 mm,
- desired deviations: x_2 = 0.01 mm and x_1 = –0.01 mm.

For the coordinates of the centre of the area of variation the following condition must be met:

$$M_L' = M_L, \quad (26)$$

where M_L' is coordinate of the centre of the performance tolerance variation area, and M_L coordinate of the centre variation area of the tolerance desired. Using the formulas:

$$M_L = 0.5(x_1+x_2) \text{ and } M_L' = \sum_{i=1}^{m}\left(\frac{\partial L}{\partial A_i}\right)M_{A_i}, \quad (27)$$

where x_1, x_2 are desired deviations, and M_{A_i} are coordinates of the centres of the area of variation of the component dimensions before selection M_L=0.015 mm, and M_L'= 0 mm.

A zero value was obtained due to symmetrically distributed deviations for each component dimension. In the present case, the condition of equality of the coordinates of the centres of the areas of variation $M_L'=M_L$ is not satisfied. The fulfilment of the conditions of equality of the coordinates of the area of variation Eq. (26) and equality of tolerance Eq. (25) gives confidence in the constancy of the resultant dimensions in each selection group [22]. In order to meet this requirement, the dimensional deviations of some component cells were changed and recalculated. New deviation values for the ball diameter d were adopted on the basis of experience and deviation calculations were carried out for R and S. Table 3 summarises the previous and new tolerance values.

$$M_L' = 0.5\sum_{i=1}^{m}\left(\frac{\partial L}{\partial A_i}\right)\left(x_{1i}+x_{2i}\right)$$

$$= 0.50\times\left(-3.105\times\left(-0.005\right)+0.73\times\left(x_{1R}+x_{2R}\right)\right)=0.015 \text{ mm},$$

and $T_R=0.08=x_{2R}-x_{1R}$, we get $x_{1R}=-0.03$ mm and $x_{2R}=0.05$ mm.

Table 3. Previous and new tolerance values

Dimension	Nominal value	Design tolerance	New tolerance
r_z [mm]	6.730	± 0.025	+0.025, –0.015
r_w [mm]	6.540	± 0.025	+0.025, –0.015
$R = r_w+r_z$ [mm]	13.270	± 0.050	+0.050, –0.030
d [mm]	12.700	± 0.0097	+0.001, –0.006
d_z [mm]	65.878	± 0.020	± 0.013
d_w	40.211	± 0.020	± 0.013
$S = 0.5(d_z–d_w)$ [mm]	12.834	± 0.020	± 0.0125

After this change, equal values of the coordinates of the centres of the tolerance variation areas were obtained. Rechecking the condition of equality of tolerance of the two parts of the split dimensional chain.

$1\times0.04+2.375\times0.04\approx1\times0.02+3.105\times0.007+0.73\times0.08$,

$0.135\neq0.1$.

The condition of equality of tolerance is not fulfilled, which means that the axial clearance will not reach the value between 0.05 and 0.025 mm. To avoid this, the tolerance of dimension S was changed without changing the equality of values of the centres of the tolerance variation areas of part I of the chain. For this purpose, the necessary tolerance for S was calculated.

The tolerance of Part I is equal to $1\times0.04+2.375\times T_S' = 0.1$ so $T_S' = 0.025$. Then S will be $12.834^{\pm0.0125}$ mm.

Calculation of actual tolerance for new tolerances on independent dimensions $T_L' = 1\times0.04+1\times0.02+2.375\times0.0125+3.105\times0.007+0.73\times0.08 = 0.17$ mm. For an actual axial clearance tolerance of 0.17 mm, the number of selection groups will be 9.

4 DISCUSSION

Wheel hub units have numerous benefits and as such they are replacing traditional wheel bearings in motor vehicles. To design them, engineers now commonly apply GPS principles since these help them better reflect their intentions and prevent drawing interpretation errors. The mathematical model proposed in this article was used to determine the amount axial clearance and the optimal tolerances of toleranced dimensions for a generation 2 wheel hub unit with a dual-row angular contact ball bearing. In this case the axial clearance determined using the dimensional chain equation was 3.3 µm greater than the value assumed by the designer. The tolerance values obtained with the model were validated by comparing them with the values assumed by the designer for this product. These are significantly smaller than the tolerances adopted by the designer. This indicates that it is necessary to change the tolerances of the component dimensions and manufacture the product under interchangeability conditions using the selective compensation approach. In the case under consideration, the division of the independent dimensions into nine selection groups allows components to be manufactured with tolerances that are achievable, economically justified and assembly guaranteed to meet the designer's requirements.

5 CONCLUSIONS

The proposed solution of using a mathematical dimensional chain model in the design of a second-generation bearing hub is an alternative to the frequently used product and process design method based on designer experience, numerous tests and at considerable cost. Its use will reduce the time and cost associated with designing a bearing hub and putting it into production. The proposed solution will still be documented and validated in series production of bearing hubs which is planned in the near future.

REFERENCES

[1] Prasad, B. *Concurrent Engineering Fundamentals*, Vol I: Integrated Product and Process Organization (1996) Prentice Hall PTR, Upper Saddle River

[2] Trabelsi, A., Delchambre, A. Assessment on tolerance representation and tolerance analysis in assemblies. *Concurr Eng Res Appl* 8, (2000) **DOI:10.1106/HN8W-XEJD-TGMD-VAFD**

[3] Singh, P.K., Jain, P.K., Jain, S.C. Important issues in tolerance design of mechanical assemblies. Part 1: tolerance analysis. *Proc Inst Mech Eng Pt B J Eng Manufact* 223 (2009) **DOI:10.1243/09544054JEM1304A**

[4] Singh, P.K., Jain, P.K., Jain, S.C. Important issues in tolerance design of mechanical assemblies. Part 2: Tolerance analysis. *Proc Inst Mech Eng B J Eng Manuf* 223 (2009) **DOI:10.1243/09544054JEM1304B**

[5] Tsung, C.-K. Optimizing the tolerance for the products with multi-dimensional chains via simulated annealing. *Symm* 13, 1780 (2021) **DOI:10.3390/sym13101780**

[6] Ramnath, S., Haghighi, P., Chitale, A., Davidson, J., Shah, J. Comparative study of tolerance analysis methods applied to a complex assembly, *Proc CIRP* 75, p. 208-213 (2018) **DOI:10.1016/j.procir.2018.04.073**

[7] Haghighi, P., Ramnath, S., Chitale, A., Davidson, J., Shah, J. Automated tolerance analysis of mechanical assemblies from a CAD model with PMI. *Comput-Aided Des Applic* 17, 2, 249-273 (2020) **DOI:10.14733/CADAPS.2020.249-273**

[8] Gawlik, E., Gil, S. The concept of a system for evaluating the technological performance of machine parts and machine assemblies. *Sci J Rzeszów U Tech: Mech* 279 239-249 (2011)

[9] Maciejczyk. A., Zdziennicki. Z. Bearing of vehicle wheel hubs. *Autobusy. Technique, Exploitation, Transport Systems,* no. 3 (2013)

[10] Hofmann, R., Gröger, S. Closed loop geometrical tolerance engineering with measuring data for reverse information processing. *Proc CIRP* 84 p. 311-315, (2019) **DOI:10.1016/j.procir.2019.04.242**

[11] Adamczak S. Geometric measurements of surfaces. Shape outlines, waviness and roughness. *WNT* (2008)

[12] Adamczak, S. Geometrical metrology of technological surfaces. *WNT* (2023) p. 355-356, 384-388

[13] Malakova, S., Sivak, S. GPS application in the design of gearboxes. *Acta Mech Auto* 16, 4 (2022) **DOI:10.2478/ama-2022-0037**

[14] EN ISO 8015:2012 Geometrical product specifications (GPS). *Fundamentals. Concepts, principles and rules*. *International Organization for Standardization* (2012) Geneva

[15] ISO 492:2014 Rolling bearings-Radial bearings-Dimensional and geometrical tolerances. *International Organization for Standardization* (2014) Geneva

[16] Białas, S., Humienny, Z., Kiszka, K. Metrology with fundamentals of product geometry specification (GPS). Publishing House of the Warsaw University of Technology (2021) Warsaw

[17] Humienny, Z. Product geometry specification language - mysterious and unknown or every engineer's second mother tongue? *Mech* 7 (2020) **DOI:10.17814/mechanik.2020.7.14**

[18] Adamczak, S., Gajur, M., Kuzmicki, K. Use of geometrical product specifications in the structural design of second generation bearing hub unit. *Trans Res Proc*, 74, p. 486-492 (2023) **DOI:10.1016/j.trpro.2023.11.172**

[19] Sukiennik, E., Arendarski, J. Issues of selection group tolerance selection in the completion of double row angular contact ball bearings. *Probl Tech Qual Roll Bear* (1985) 176-178

[20] Meller, E., Preihs, J. *Exercises in Tolerance Analysis in Machine Technology* Ed. I, p. 69-72 (2006) Gdansk

[21] Jezierski, J., Kowalik, M., Siemiątkowski, Z., Warowny, R. Tolerance analysis in machine design and technology. *Coll Tasks. WNT,* 343-349 (2010) Warsaw

[22] Jezierski, J. Analysis of tolerances and inaccuracies of measurements in mechanical engineering. *WNT* (1994)

Received 2024-04-13, revised 2024-09-12, accepted 2024-10-03
Original Scientific Paper.

Data availability *Data supporting the proposed solution will be available from authors K Kuźmicki and M Gajur.*

Author contribution *S Adamczak contributed to conceptualization, supervision, writing – review & editing; M Gajur performed formal analysis, validation, writing – review & editing; K Kuźmicki provided formal analysis, funding acquisition, project administration, resources, validation, visualization, writing – original draft, writing – review & editing*

Matematični model dimenzijske verige za enoto kolesnega pesta 2. generacije

POVZETEK *Članek predstavlja pregled konstrukcijskih rešitev pesta kolesa ter predlaga matematični model dimenzijske verige in enačbo za izračun tolerance za izračun osne zračnosti za sklop pesta kolesa 2. generacije s krogličnimi ležaji. Analiza dimenzijske verige in njena sinteza sta izvedeni z uporabo treh metod delne zamenljivosti. Predlagana je bila možnost izdelave ležaja pesta z uporabo izbirne kompenzacije. Opravljeni razmisleki predstavljajo alternativo sedanji metodi načrtovanja procesa, ki temelji na številnih poskusih in precejšnjih stroških.*

Ključne besede *kotalni ležaji, dimenzijska veriga, tolerančna formula, osna zračnost, enota kolesnega pesta*

Numerical and Experimental Investigation of Aspect Ratio Effect on Aerodynamic Performance of NACA 4415 Airfoil Section at Low Reynolds Number

Hatice Cansu Ayaz Ümütlü[1] ✉ – Zeki Kıral[2] – Ziya Haktan Karadeniz[3]

1 Dokuz Eylul University, The Graduate School of Natural and Applied Sciences, Turkey
2 Dokuz Eylul University, Faculty of Engineering, Turkey
3 Izmir Institute of Technology, Department of Energy Systems Engineering, Turkey

✉ cansu.ayaz@deu.edu.tr

Abstract *In this study, the effect of aspect ratio on the aerodynamic coefficients is investigated for a NACA 4415 airfoil profile. Four different aspect ratios which are 3, 5, 7, and 9 are evaluated with the computational fluid dynamics (CFD) simulations and the experiments. The CFD studies are performed using a three-dimensional (3D) computational domain and by using the k–ω shear stress transport (SST) turbulence model for turbulence calculations. The measurements of the aerodynamic forces are carried out in open jet type wind tunnel using a three-component balance. CFD and experimental studies are performed at angles of attack from 0° to 25° and Reynolds number 85·10³. The results show that as the aspect ratio increases, separation points move towards the leading edge of the airfoil and the stall angle reduces. Furthermore, it is observed that the lift coefficients increase with the increasing aspect ratio. The results obtained indicate that there is a harmony between the experimental data and the CFD solutions.*

Keywords *airfoil, wind tunnel, aspect ratio effect, aerodynamic coefficients, three-component balance, low Reynolds number*

Highlights:

- *The research investigates the aspect ratio effect on NACA 4415 airfoil at low Reynolds number.*
- *Four different aspect ratios are investigated both experimentally and numerically.*
- *Experiments and numerical studies show that with increasing aspect ratio, the coefficients of lift increase.*
- *The research demonstrates that with increasing aspect ratio, the stall angle reduces.*

1 INTRODUCTION

Airfoils are important components of many scientific and technological fields, including wind energy, aerospace, defense, transportation, jet engines, unmanned aerial vehicles (UAVs), mixing of fluid products, etc. [1] to [3]. There are many studies in the literature on the design and analysis of airfoil structures due to their frequency of use and importance in different industrial application areas. In aerodynamics, Reynolds numbers below 500·10³ are typically considered to be in the low Reynolds number range. Generally, high Reynolds number studies are conducted and there is limited research in literature related to low Reynolds numbers. Winslow et al. [4] studied aerodynamic characteristics and separation characteristics at Reynolds numbers from 10·10⁴ to 10·10⁵. Akbiyik et al. [5] studied the aerodynamic performance of a NACA 0015 airfoil at a Reynolds number of 48·10³ under different configurations of plasma actuator electrodes. Bartl et al. [6] investigated the lift, drag and surface pressure of an airfoil at low to moderate Reynolds numbers ranging from 50·10³ to 600·10³. Traub and Coffman [7] studied the leading and trailing edge flaps at Reynolds numbers of 40·10³, 60·10³, and 80·10³. Their results showed that the flaps affect the aerodynamic characteristics positively. Xia et al. [8] briefed the flow structures of airfoils at low Reynolds numbers. They examined the laminar separation bubbles and their effects. Murayama et al. [9] studied the aerodynamic performances of the low Reynolds numbers airfoil to observe the effect of the robustness, and they used a flexible flap, a bird-inspired wing, in their experimental study. Ayaz Ümütlü et al. [10] experimentally revealed that the maximum lift and stall angle at low Reynolds number condition are lower in comparison with the high Reynolds number region. Stutz et al. [11] investigated vertical gust and airfoil interaction at Reynolds numbers 12·10³ and 54.4·10³. Somashekar and Immanuel Selwynraj [12] examined the effect of rain on the aerodynamic characteristics of an airfoil operating at a Reynolds number of 200·10³.

It is important to define the flow characteristic of the airfoil in order to improve the aerodynamic performance. The aspect ratio (AR) has a substantial impact on the aerodynamic behavior of the airfoil. In literature, there are studies considering the different aspects of the aspect ratio effects. Ananda et al. [13] studied on flat-plate wings with the aspect ratio range of 2 to 5 at low Reynolds numbers. They found that from the wind tunnel tests the Oswald's efficiency factors exhibited considerable sensitivity in aspect ratio changes. As the aspect ratio increased, it was observed that Oswald's efficiency factor declined. Lee et al. [14] numerically studied aspect ratio effects on a revolving wing. They used a rectangular wing and considered the Rossby number while conducting the study. The aspect ratio ranges of their study are 1 to 10. Awasthi et al. [15] experimentally studied the flow structure of the airfoil with the aspect ratio of 0.5. They presented that in an airfoil with such a low AR, the interactions of already existing complex flow structures are present even in the mid-span of the airfoil. Zanforlin and Deluca [16] studied the effects of the tip losses on the aspect ratio of the vertical axis wind turbines. They investigated the AR interval of 0.25 to 3. They performed three dimensional CFD analysis. They assessed high AR with low tip losses or low AR with higher losses airfoil to achieve the maximum power output. They identified the optimal aspect ratio that gives the highest

DOI: 10.5545/sv-jme.2024.1155

power. Lee and Han [17] studied NACA 0012 airfoil with the aspect ratios of 3, 4, 5, and 6 at high angle of attack (AoA). They measured lift and drag by load cells. Ayaz Ümütlü et al. [18] experimentally studied on NACA 4415 airfoil which has an aspect ratio of 9 and proposed a new approach for stall detection.

The NACA 4415 airfoil profile is a type of cambered airfoil that can be used in vertical-axis wind turbines (VAWTs). However, a few experimental studies are using NACA 4415 airfoil at low Reynolds number conditions. We aimed to fulfill this gap in the literature by investigating the NACA 4415 airfoil experimentally at Reynolds number $85 \cdot 10^3$. Asr et al. [19] studied the start-up characteristics of H-Darrieus vertical-axis wind turbines using NACA airfoils. They utilized Ansys Fluent to conduct transient CFD analysis to investigate this behavior. Parker et al. [20] studied the effect of chord-to-diameter ratio on the wake of VAWTs. They investigated three different D/c ratios which are 3, 6, and 9 and they used NACA 0022 symmetrical airfoil in their experiments. Zhong et al. [21] studied the dynamic stall control using a leading-edge rod on the Darrieus vertical-axis wind turbine. They used NACA 4-digit symmetrical airfoil profiles in their study. Song et al. [22] studied on aerodynamic characteristics of the Darrieus vertical-axis wind turbine and they investigated varying thickness (12 %, 15 %, 18 %, and 21 %) of the airfoil using CFD simulations.

There are two important research which show the effects of the Reynolds number and the aspect ratio. Miley [23] published a catalog on the Reynolds number effect over the various airfoil profiles at different test conditions. It is seen from Fig. 1 that as the Reynolds number increases, the lift coefficient also increases. However, the aspect ratio is not detailly presented in Miley's study. Moreover, Ostowari and Naik [24] studied on the aspect ratio effect of the NACA 4415 airfoil at Reynolds number of $250 \cdot 10^3$ for the aspect ratios of 6, 9, 12, and infinite span. Compared to Ostowari and Naik's [24] study, a lower Reynolds number is used in this paper while the aspect ratios are 3, 5, 7, and 9. The results of this paper are evaluated in the light of these two important studies in the literature. Fig. 1 shows some of the results of Miley's [23], and Ostowari and Naik's [24] studies. The main contribution of this paper is the investigation of the aspect ratio interval of the NACA 4415 airfoil under the low Reynolds number condition to cover the gaps that remained in the studies mentioned above.

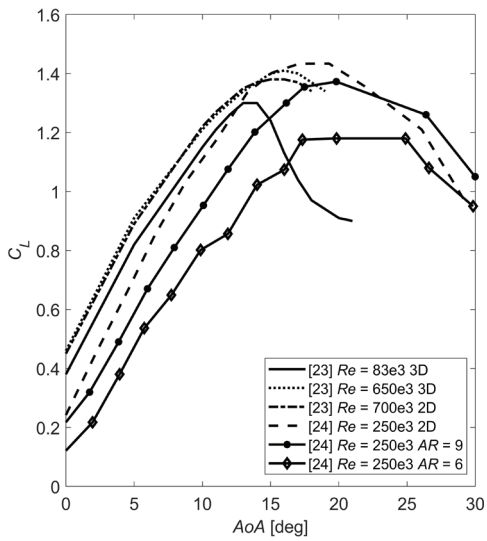

Fig. 1. The results of the studies of Miley [23], and Ostowari and Naik [24]

There are many studies on airfoils, but the number of studies considering the aspect ratio of the airfoil at low Reynolds number are limited. In the present study, NACA 4415 airfoil is selected as a model, and wind tunnel tests are conducted for four different aspect ratios of 3, 5, 7, and 9 at low Reynolds number conditions. Furthermore, the flow analyses are performed to compare the results. The objective of this paper is to determine the aspect ratio effect on the lift and drag coefficients of NACA 4415 airfoil section. In addition, since it is difficult to study at low Reynolds numbers, we aimed to fill the experimental study gap in the literature with this study by examining the aspect ratio at $85 \cdot 10^3$ Reynolds number. For obtaining the lift and drag coefficients, a three-component balance system is utilized in the experiments.

This paper is structured as follows: The methods and materials section explains the numerical and experimental procedures. In the results and discussions section, the results of the simulations and experiments are given and discussed in detail. The conclusion section summarizes the key outcomes of the study.

2 METHODS AND MATERIALS

The numerical simulations and experiments were conducted to study the aerodynamic characteristics of the NACA 4415 airfoil which had a chord length of 105 mm, and the corresponding Reynolds number was $85 \cdot 10^3$. During the studies, the effect of the aspect ratio on the coefficients of lift and drag was investigated. The aspect ratio is the ratio of the airfoil span and the chord length. The investigated aspect ratios within the scope of this study were 3, 5, 7, and 9. The aspect ratio is defined as;

$$AR = \frac{b^2}{S} = \frac{b}{c}, \tag{1}$$

where AR, b, c, and S indicate the aspect ratio, span, chord length, and the planform area of the airfoil, respectively. The Reynolds number is expressed as;

$$Re = \frac{\rho v c}{\mu}, \tag{2}$$

where Re, ρ, v, μ indicate the Reynolds number, density of the air, free stream velocity, and the dynamic viscosity, respectively. The formulae used for the calculation of the lift and drag coefficients are given as;

$$C_L = \frac{2F_L}{\rho v^2 S}, \tag{3}$$

$$C_D = \frac{2F_D}{\rho v^2 S}, \tag{4}$$

where F_L is lift force and F_D is drag force. C_L and C_D are the coefficients of lift and drag, respectively.

2.1 Numerical Procedure

2.1.1 Model Definition

The numerical results of this study were obtained for a NACA 4415 airfoil profile. Boundary conditions had been set as velocity inlet, pressure outlet, and the wall along the airfoil and along the sides of the computational domain except for the right side. The symmetry was applied to the right side of the domain to decrease the number of elements created and accordingly the computational time.

2.1.2 Mesh Independence Study

Both hexahedral - tetrahedral and hexahedral - polyhedral meshes were created to observe the effect of meshes on the simulation time. Fig. 2 provides mesh details of the computational domain. The computational domain was divided into two parts to generate more successful mesh grids. The mesh quality in the near-field area

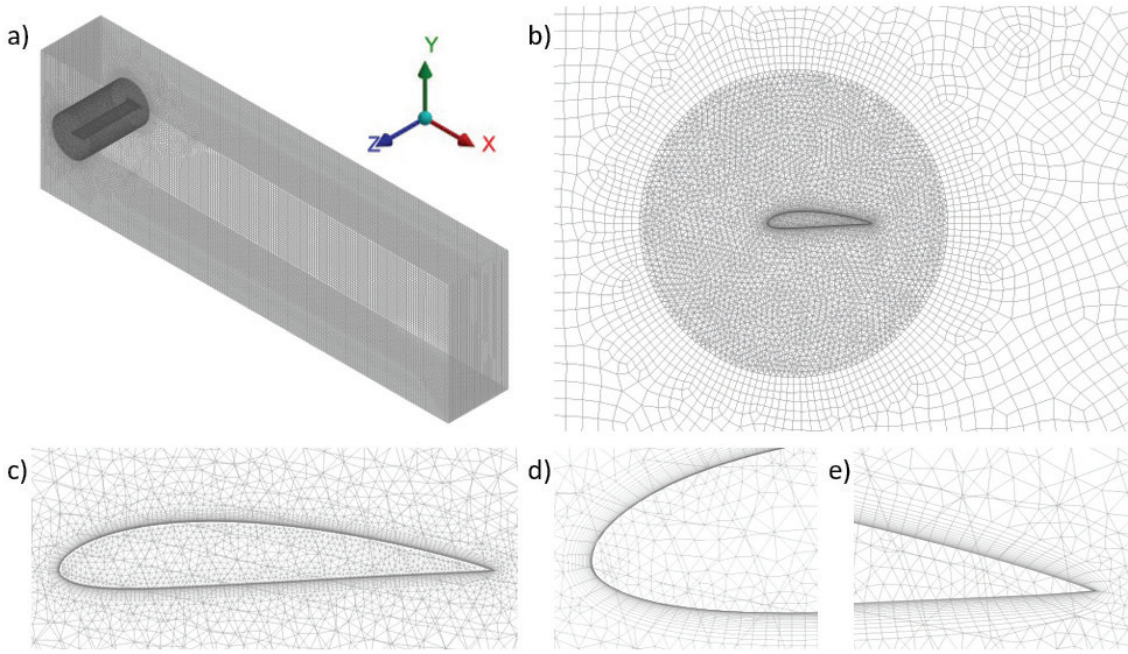

Fig. 2. Mesh details; a) computational domain; magnified mesh view around, b) the near-field, c) the airfoil; magnified view of the inflation layers around, d) the leading edge, and e) the trailing edge

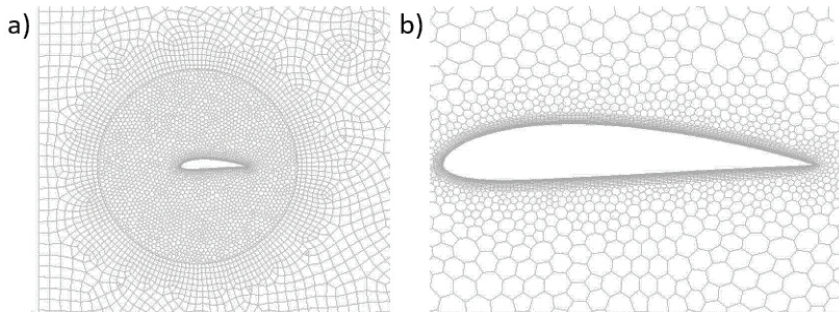

Fig. 3. a) Polyhedral mesh in the near-field area, and b) magnified view of the polyhedral mesh around the airfoil

around the airfoil was improved using the body sizing and face sizing method. The sizing option of the overall mesh was proximity and curvature. Inflation layer with 20 layers and a growth rate of 1.2 was employed along the airfoil wall to provide the y+ < 5 requirement. y+ values were around 1 for all analyses performed in this study. The mesh statistics show that the number of nodes was 1730042 and the orthogonal quality was 0.88.

The simulations were run using ANSYS® Fluent on a computer with Intel Core i7- 6700HQ, 2.6 GHz CPU and 16 GB RAM. To reduce the convergence time and complete the analysis in a shorter time, polyhedral meshes were used in the flow analysis. It means that converting the tetrahedral mesh to the polyhedral mesh affects the computational expense positively. Table 1 summarizes the relation between the simulation time and the applied meshes and Fig. 3 shows the polyhedral mesh details.

Table 1. The effect of tetrahedral and polyhedral meshes on convergence time at grid level = 4 at 0° AoA for AR = 9

	Hexahedral & Tetrahedral	Hexahedral & Polyhedral
Average time per iteration [s]	9.778	4.813
Total convergence time [s]	12799	2411

Table 2. Mesh independence study at 0° AoA for AR = 9

grid #	max face size [m]	max size [m]	body & face sizing [m]	# of nodes	orthogonal quality	y^+	C_L/C_D	average time per iteration [s]
1	3e-2	5e-2	1.5e-2	637048	0.83	1.05357	10.11	2.372
2	1.8e-2	2e-2	1e-2	1089297	0.86	1.05652	10.15	3.125
3	1.8e-2	2e-2	8e-3	1268383	0.87	1.05936	10.21	3.550
4	1.8e-2	2e-2	6e-3	1730042	0.88	1.05980	10.32	4.813
5	1.5e-2	1.8e-2	6e-3	2115060	0.89	1.06013	10.32	5.684
6	1.2e-2	1.5e-2	6e-3	2807537	0.90	1.06237	10.32	7.244

Table 2 presents the results of the mesh independence study. Mesh quality affects both computational accuracy and computational time. The optimum element number is the point where the results are accurate with the fewest elements. 4th grid was chosen for the simulation not to increase the number of nodes and the computational time. Fig. 4 shows the relation between the grid level and C_L/C_D.

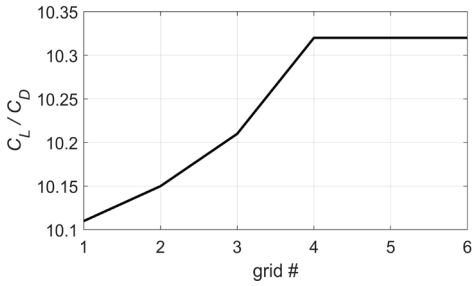

Fig. 4. Grid # and C_L/C_D relation

2.1.3 Simulation Setup

As a turbulence model, k–ω SST with a standard set of coefficients was selected. The SIMPLE scheme was used to handle the pressure-velocity coupling. Second-order upwind discretization scheme was applied for all RANS equations due to its balance of accuracy and computational efficiency. The residual convergence level of the simulations was 10^{-7}. The governing equations of the k–ω SST turbulence model are given by:

$$\frac{\partial(\rho k)}{\partial t}+\frac{\partial(\rho U_j k)}{\partial x_j}=P_k-C_\mu\rho k\omega+\frac{\partial}{\partial x_j}\left[\left(\mu+\frac{\mu_t}{\sigma_k}\right)\frac{\partial k}{\partial x_j}\right], \quad (5)$$

$$\frac{\partial(\rho\omega)}{\partial t}+\frac{\partial(\rho U_j\omega)}{\partial x_j}=C_{\omega1}\frac{\omega}{k}P_k-C_{\omega2}\rho\omega^2+\rho(1-F_1)CD+\frac{\partial}{\partial x_j}\left[\left(\mu+\frac{\mu_t}{\sigma_\omega}\right)\frac{\partial\omega}{\partial x_j}\right], \quad (6)$$

where k, ω, μ_t, σ_k, σ_ω, CD, F_1, $C_{\omega1}$ and $C_{\omega2}$ represent the turbulence kinetic energy, specific dissipation rate, turbulent viscosity, turbulent Prandtl numbers for k and ω, cross-diffusion term, blending function, and model coefficients, respectively. Simulation parameters are presented in Table 3.

Table 3. Simulation parameters

Turbulence model	k–ω SST with a standard set of coefficients
Solver	Pressure based SIMPLE scheme
Discretization	Second-order upwind scheme
Residual convergence level	10^{-7}

2.2 Experimental Setup

At the İzmir Kâtip Çelebi University, Turkey, a wind tunnel was employed to conduct experiments. The airfoil's mounting frame was constructed from 30 mm × 30 mm aluminum profiles, as depicted in Fig. 5. The wind tunnel features an open-square jet section with dimensions of 1000 mm × 1000 mm and has a maximum freestream velocity of 12 m/s. The three-component balance system provided structural support to the airfoil, which was attached via a shaft at its quarter chord, and had a protractor on it that allows to set the airfoil's attack angle. A series of force measurements were conducted using the three-component balance for the investigation of the airfoil's aerodynamic performance. Before the measurements, the wind-off load was subtracted to calibrate the measurement system. The resulting force values were read from the display unit, and the force values were evaluated using the calibration table which was generated before the measurements.

NACA 4415 airfoil was modeled using a CAD program, and the airfoil model was fabricated by a three - dimensional (3D) printer using PLA material. The software's printing settings were configured with the following specifications: layer height at 0.2 mm, wall thickness at 1.5 mm, wall line count at 3, and infill density at 15 %. Also, a tri-hexagon infill pattern was used as an internal structure of the airfoil. Fig. 6 shows the 3D printed airfoil model.

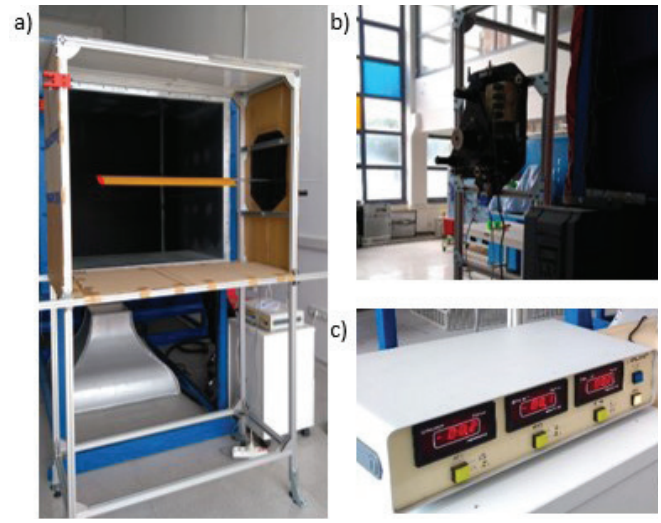

Fig. 5. Experimental setup; a) low-speed wind tunnel, b) three-component balance, and c) display unit

3 RESULTS AND DISCUSSIONS

The numerical simulation results are utilized to support the interpretation of the experimental part of this study. To interpret the results, the velocity vectors and the vortices around the airfoil are investigated. To investigate the separation characteristics of the airfoil, the vector representation of the flow is given in Fig. 7. Red arrows in the figure show the separation points. As the aspect ratio and angle of attack increase, it can be seen that the separation points move towards the leading edge of the airfoil. For low aspect ratios flow remains largely attached to the airfoil at low angles of attack. However, separation is stronger for high aspect ratio airfoils compared to low aspect ratios. In other words, it has been observed numerically that stall occurs at smaller angles of attack as the aspect ratio increases. The performed experiments are compatible with the data obtained as a result of numerical analysis.

Flow rolls around the tip of the airfoil from bottom to top, and it is called tip vortex. Lambda2 vortex criterion is a detection method of the vortices from a 3D flow. The method is used to identify and analyze regions of rotational motion and they are visualized using ANSYS® Fluent. Fig. 8 depicts the iso-surface plots of the Lambda2 criterion and tip vortices can be seen at the tip of the airfoil for all AoA and the aspect ratios. It appears that the tip vortices do not change with increasing AoA. However, the spanwise vortices form through the airfoil, and they grow with the increasing AoA. At low AoA, the spanwise vortices are weaker and more evenly distributed across the span of the airfoil. As AoA increases, the strength of the spanwise vortices increases. At higher AoA, while vortex structures grow larger, the flow remains more organized for lower aspect ratio airfoils than higher AR airfoils.

Fig. 6. 3D printed airfoil model; a) top-view, and b) side-view

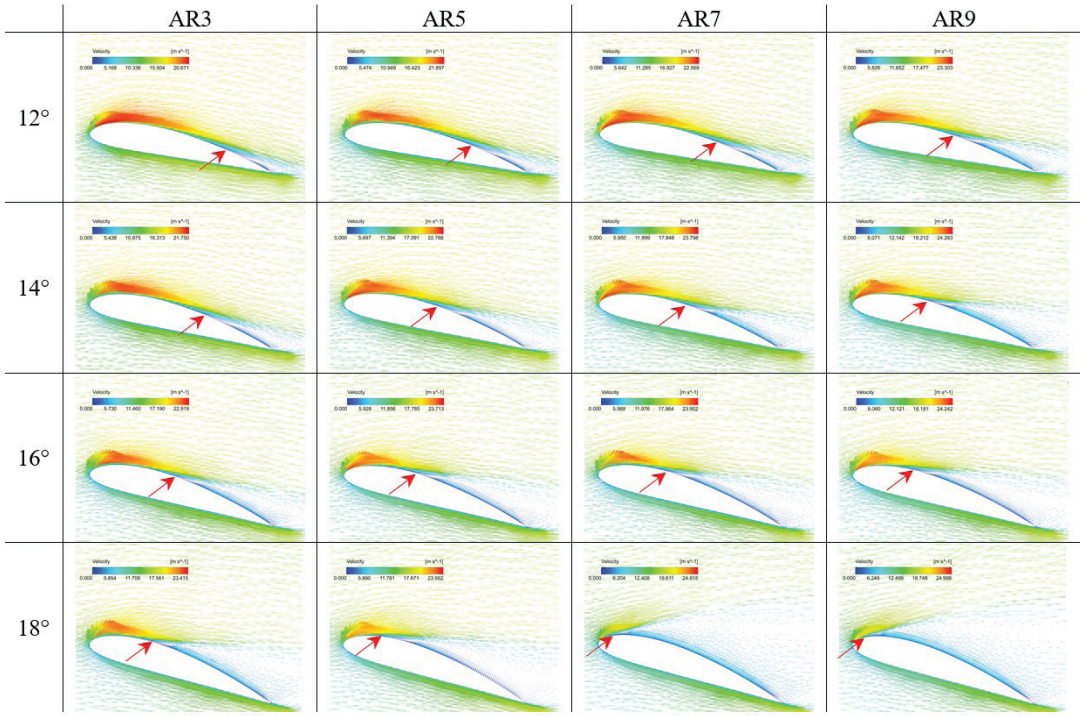

Fig. 7. Separation characteristics of airfoils with different aspect ratios at Re = 85·10³ (red arrows represent separation)

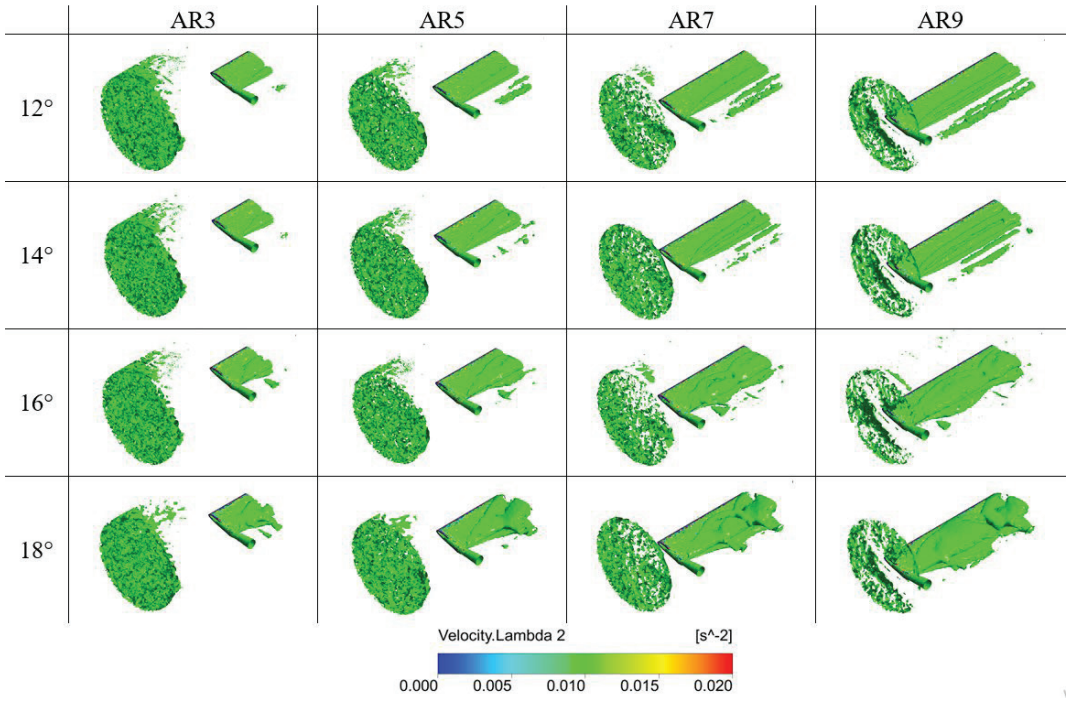

Fig. 8. Iso-surface plots of Lambda2 criterion

The aerodynamic coefficients' relation with the AoA is given in Fig. 9, and the stall angles have been examined in detail concerning AR and AoA relations. The results are obtained for the different aspect ratios of the airfoil, and the aspect ratio effect is observed on the NACA 4415 airfoil with chord length of 105 mm. The findings of the present study are consistent with the results of Miley [23], and

Ostowari and Naik [24] studies given in the introduction part. As compared to Ostowari and Naik [24] study, the presented experiments are conducted at a lower Reynolds number condition, and thus, the maximum lift coefficients are lower than their study as expected. Also, Miley [23] shows that when the Reynolds number is lower, the stall happens at lower angles of attack.

Firstly, the outcomes of the experiments are presented. The maximum lift coefficient for aspect ratio of 3 is 0.864 and the corresponding angle of attack is 18°. The maximum lift happens at 17° of angle of attack for aspect ratio of 5 and the value of the lift coefficient is 0.965. For aspect ratio 7, the maximum lift occurs at 15° of angle of attack and it is 1.068. The maximum lift coefficient is 1.164 for aspect ratio 9 and the corresponding angle of attack is 13°.

Secondly, the results of the numerical studies are shared. The maximum lift coefficient is 1 for the aspect ratio of 3 and it occurs at 18° of angle of attack. For aspect ratio 5, the maximum lift happens at 16° of angle of attack and the value of the lift coefficient is 1.05. The maximum lift coefficient for the aspect ratio of 7 is 1.09 and the maximum lift occurs at 15° of angle of attack. Aspect ratio of 9 has a maximum lift coefficient of 1.19 at 13° of angle of attack.

The maximum lift coefficient difference between the experimental and numerical results gets closer as the aspect ratio increases from 3 to 9. In airfoils with low aspect ratios, three-dimensional characteristics like flow separation and tip vortices are significant. Higher aspect ratios reduce these three-dimensional effects, resulting in more two-dimensional flow and improved agreement between numerical and experimental data. The percentage difference rates are 15.74 %, 8.81 %, 2.83 %, and 2.23 % for aspect ratios of 3, 5, 7, and 9, respectively. The results of the numerical studies and the experiments show similar tendencies. Although there are differences in the maximum lift values, stall angles are coherent. The results of the experimental and numerical studies are presented in Table 4.

Table 4. Comparative data of the experimental and the numerical studies

	max C_L (experimental)	max C_L (numerical)	% Difference	Corresponding *AoA*
AR3	0.864	1	15.74	18°
AR5	0.965	1.05	8.81	16° to 17°
AR7	1.068	1.09	2.83	15°
AR9	1.164	1.19	2.23	13°

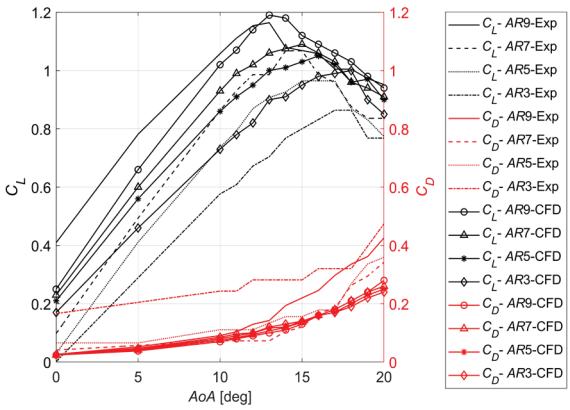

Fig. 9. Comparison of the experiment and CFD results

As the numerical and experimental results of the drag coefficients are compared, they are in harmony in certain AoAs except for the aspect ratio of 3. The experimental results are higher than the numerical result of aspect ratio of 3 for all angle of attacks. For aspect ratio 5, the difference between the experimental and numerical results is observed after 17° of angle of attack and the situation is the same for the aspect ratio of 7. The difference begins at 13° of angle of attack for aspect ratio of 9. The numerical results of the drag coefficients are very close to each other and they are sorted from aspect ratio of 9 as the smallest and 3 as the highest and after 16° the sequence turns the opposite.

4 CONCLUSIONS

Experimental measurements and flow analysis were performed to observe the influence of the various aspect ratios on the aerodynamic characteristic of the NACA 4415 airfoil profile for low Reynolds number. A low-speed, open section wind tunnel was used during the experiments. Also, a three-component balance system was utilized to measure the forces on the airfoil for different angles of attack. The lift and drag coefficients were calculated using obtained forces. ANSYS® Fluent software was used for comparing the results of the 3D flow analysis with the findings of the experiments.

The results of the experiments and the numerical studies show that with the increasing *AR*, the lift coefficients increase. Furthermore, the angles of attack in which the maximum lift is obtained, decrease with the increasing AR of the airfoil. Namely, the stall angle which is a critical parameter in airfoil design for aerodynamic systems decreases. During the flow analysis with the increasing AR, the drag coefficients decrease until AoA of 16°, while the drag coefficients increase with the increasing *AR* after this AoA. In conclusion, there is compatibility between the experimental and the numerical results in terms of the aerodynamic coefficients of the airfoil.

Further studies are planned to examine the effect of aspect ratio on airfoils at higher angles of attack and low Reynolds numbers.

REFERENCES

[1] Mohammed, A., Lemu, H.G., Sirahbizu, B. Determining optimum rotary blade design for wind-powered water-pumping systems for local selected sites. *Strojn vestn-J Mech E* 67 214-22 (2021) **DOI:10.5545/sv-jme.2021.7104**

[2] Ganesan, T., Jayarajan, N. Aerodynamic analysis of mathematically modelled propeller for small UAV using CFD in different temperature conditions. *Strojn vestn-J Mech E* 69 444-454 (2023) **DOI:10.5545/sv-jme.2023.601**

[3] Kılavuz, F., Kiral, B.G. Design optimization of mechanical valves in dishwashers based on the minimization of pressure losses. *Strojn vestn-J Mech E* 70194-208 (2024) **DOI:10.5545/sv-jme.2023.768**

[4] Winslow, J., Otsuka, H., Govindarajan, B., Chopra, I. Basic understanding of airfoil characteristics at low reynolds numbers (104-105). J Aircraft 55 1050-1061 (2018) **DOI:10.2514/1.C034415**

[5] Akbıyık, H., Yavuz, H., Akansu, Y.E. A study on the plasma actuator electrode geometry configurations for improvement of the aerodynamic performance of an airfoil. Strojn vestn-J Mech E 64 719-725 (2018) **DOI:10.5545/sv-jme.2017.5041**

[6] Bartl, J., Sagmo, K.F., Bracchi, T., Sætran, L. Performance of the NREL S826 airfoil at low to moderate Reynolds numbers-A reference experiment for CFD models. *Eur J Mech B-Fluid*75 180-192 (2019) **DOI:10.1016/j.euromechflu.2018.10.002**

[7] Traub, L.W., Coffman, C. Efficient low-reynolds-number airfoils. *J Aircraft* 56, 1987-2003 (2019) **DOI:10.2514/1.C035515**

[8] Xia, T., Dong, H., Yang, L., Liu, S., Jin, Z. Investigation on flow structure and aerodynamic characteristics over an airfoil at low Reynolds number-A review. *AIP Adv* 11 (2021) **DOI:10.1063/5.0044717**

[9] Murayama, Y., Nakata, T., Liu, H. Flexible flaps inspired by avian feathers can enhance aerodynamic robustness in low Reynolds number airfoils. *Front Bioeng Biotech* 9 612182 (2021) **DOI:10.3389/fbioe.2021.612182**

[10] Ayaz Ümütlü, H.C., Kıral, Z., Karadeniz, Z.H. A Preliminary experimental study on the effect of Reynolds number on the lift and drag of a NACA-4415 airfoil. *6th International Students Science Congress Proceedings Book*. 1-5 (2022) **DOI:10.52460/issc.2022.047**

[11] Stutz, C., Hrynuk, J., Bohl, D. Investigation of static wings interacting with vertical gusts of indefinite length at low Reynolds numbers. *Exp Fluids* 63 82 (2022) **DOI:10.1007/s00348-022-03432-7**

[12] Somashekar, V., Immanuel Selwynraj, A. Aerodynamic study of low Reynolds number airfoil and mini-unmanned aerial vehicle in simulated rain environment. *Aircr Eng Aerosp Tec* 94 1748-1758 (2022) **DOI:10.1108/AEAT-12-2021-0379**
[13] Ananda, G.K., Sukumar, P.P., Selig, M.S. Measured aerodynamic characteristics of wings at low Reynolds numbers. *Aerosp Sci Technol* 42 392-406 (2015) **DOI:10.1016/j.ast.2014.11.016**
[14] Lee, Y.J., Lua, K.B., Lim, T.T. Aspect ratio effects on revolving wings with Rossby number consideration. *Bioinspir Biomim* 11 56013 (2016) **DOI:10.1088/1748-3190/11/5/056013**
[15] Awasthi, M., Moreau, D.J., Doolan, C.J. Flow structure of a low aspect ratio wall-mounted airfoil operating in a low Reynolds number flow. *Exp Therm Fluid Sci* 99 94-116 (2018) **DOI:10.1016/j.expthermflusci.2018.07.019**
[16] Zanforlin, S., Deluca, S. Effects of the Reynolds number and the tip losses on the optimal aspect ratio of straight-bladed vertical axis wind turbines. *Energy* 148 179-195 (2018) **DOI:10.1016/j.energy.2018.01.132**
[17] Lee, S.H., Han, Y.O. Experimental investigation of high-angle-of-attack aerodynamics of low-aspect-ratio rectangular wings configured with NACA0012 airfoil section. *Internat J Aeronaut Space* 21 303-314 (2020) **DOI:10.1007/s42405-019-00215-z**
[18] Ayaz Ümütlü, H.C., Kiral, Z., Karadeniz, Z.H. Experimental investigation of NACA 4415 airfoil using vibration data for stall detection. *Aircr Eng Aerosp Tec* 95 1551-1559 (2023) **DOI:10.1108/AEAT-03-2023-0077**
[19] Asr, M.T., Nezhad, E.Z., Mustapha, F., Wiriadidjaja, S. Study on start-up characteristics of H-Darrieus vertical axis wind turbines comprising NACA 4-digit series blade airfoils. *Energy* 112 528-537 (2016) **DOI:10.1016/j.energy.2016.06.059**
[20] Parker, C.M., Araya, D.B., Leftwich, M.C. Effect of chord-to-diameter ratio on vertical-axis wind turbine wake development. *Exp Fluids* 58 186 (2017) **DOI:10.1007/s00348-017-2451-6**
[21] Zhong, J., Li, J., Guo, P., Wang, Y. Dynamic stall control on a vertical axis wind turbine aerofoil using leading-edge rod. *Energy* 174 246-260 (2019) **DOI:10.1016/j.energy.2019.02.176**
[22] Song, C., Wu, G., Zhu, W., Zhang, X. Study on aerodynamic characteristics of darrieus vertical axis wind turbines with different airfoil maximum thicknesses through computational fluid dynamics. *Arab J Sci Eng* 45 689-698 (2020) **DOI:10.1007/s13369-019-04127-8**
[23] Miley, S.J. *Catalog of low-Reynolds-number airfoil data for wind-turbine applications* (1982) **DOI:10.2172/5044823**
[24] Ostowari, C., Naik, D. Post stall studies of untwisted varying aspect ratio blades with an NACA 4415 airfoil section-Part I. *Wind Eng* 8 176-194 (1984)

Received 2024-09-02, revised 2024-12-05, accepted 2025-01-06
Original Scientific Paper.

Conflict of Interest *The authors declare that there is no conflict of interest.*

Data Availability *The data that support the findings of this study are available from the corresponding author upon reasonable request.*

Author contribution *Ayaz Ümütlü HC, Kıral Z, and Karadeniz ZH conceived the experiment. Ayaz Ümütlü HC operated the experiment and analyzed the data. The first draft of the manuscript was written by Ayaz Ümütlü HC. Kıral Z and Karadeniz ZH reviewed and edited the manuscript, and provided guidance.*

Numerična in eksperimentalna raziskava vpliva vitkosti krila na aerodinamične lastnosti profila NACA 4415 pri nizkem Reynoldsovem številu

Povzetek *V tej študiji je raziskan vpliv vitkosti krila na aerodinamične koeficiente profila krila NACA 4415. S simulacijami računalniške dinamike tekočin (CFD) in eksperimenti so obravnavane štiri različne vrednosti vitkosti kril, in sicer 3, 5, 7 in 9. CFD analize so izvedene s tridimenzionalno (3D) računsko domeno, za izračun turbulence pa se uporablja model k-ω za prenos strižne napetosti (SST). Meritve aerodinamičnih sil so bile opravljene v vetrovniku z odprtim tokom z uporabo tri-komponentnega merilnika sil. CFD analize in eksperimentalne meritve so bile izvedene pri naklonskih kotih od 0° do 25° in Reynoldsovem številu 85·10^3. Rezultati kažejo, da se s povečevanjem vitkosti krila ločilne točke pomikajo proti sprednjemu robu krila in da se kritični vpadni kot zmanjšuje. Poleg tega je opaziti, da se koeficient vzgona povečuje z naraščajočo vitkostjo krila. Dobljeni rezultati kažejo, da obstaja skladnost med eksperimentalnimi meritvami in rezultati CFD analiz.*

Ključne besede *aerodinamični profil, vetrovnik, vitkost krila, aerodinamični koeficienti, tri-komponentni merilnik sil, nizko Reynoldsovo število*

Integration of Phase Change Material and Heat Exchanger for Enhanced Solar Desalination – A Comparative Performance Investigation

Jothilingam Manickam[1] ✉ – Balakrishnan Nanjappan[1] – Nithyanandam Chandrasekaran[2]

1 Gnanamani College of Technology, India
2 Madha Institute of Engineering and Technology, India

✉ jothilingamm@gmail.com

Abstract *The performance and comparative analysis of several solar desalination systems using various configurations and materials are examined in this study. The study evaluates how these systems perform by measuring their overall productivity, temperature differentials, and thermal efficiency. A thorough assessment across a variety of characteristics was made possible by the consistent environmental conditions of the experiments. When phase change materials (PCM) were used as an energy storage medium, the overall amount of heat loss was significantly reduced. Studies comparing different solar stills revealed clear benefits, especially when using heat exchangers. Improved evaporative heat transfer coefficients, higher temperature differentials (ΔT), more usable heat absorption by the distilled water, and increased daily output were all seen in solar stills equipped with heat exchangers. The modified solar still with PCM and a heat exchanger had the best thermal efficiency, reaching 56 %, according to the results. The key objective of the research was to minimize heat losses and maximize freshwater yield. This thorough assessment and comparative study of several solar desalination systems offers insightful information for improving the productivity and efficiency of solar-powered water distillation technologies under a range of environmental circumstances.*

Keywords *solar desalination, phase change materials, efficiency enhancement comparative analysis*

Highlights:

- *PCMs reduced heat loss and improved thermal efficiency in solar desalination systems.*
- *Solar stills with heat exchangers showed higher output and better heat transfer.*
- *Heat exchanger integration maximized freshwater yield and minimized heat loss.*

1 INTRODUCTION

Energy conservation is vital for sustainability, especially in countries like India where resources are precious. Solar energy is renewable, it is essential to this endeavour. Solar stills demonstrate this importance by efficiently harnessing solar energy to purify water, offering a sustainable solution to address water scarcity while reducing dependence on conventional energy sources. Solar desalination is a method of separating clean water from seawater using solar energy, which is still an economical way to provide clean water. There are two categories of solar-assisted desalination systems: passive solar stills (conventional) and active solar stills (modified). Conventional solar stills consist a steel basin or black-painted copper that receives solar radiation and contains saline or seawater. In order to create a greenhouse effect and retain solar energy, the basin is encased in a trapezoidal wooden box with a glass cover at an angle of 10° to the horizontal. The glass wool insulation is packed between the basin and the wooden box to minimize heat loss. The air above the water surface gets saturated with water vapour equivalent to the water temperature because of the phase equilibrium between seawater and the air space. The surface temperature of the saline water increases when solar energy reaches it and leading to an increase in the water vapour's saturated pressure near the water surface as well as in line with the elevated temperature [1] to [3].

The partial pressure of water vapour at the glass surface lowers because of the temperature differential between the water and the inner surface of the glass cover, where the inner surface is cooler than the water surface. Condensation forms on the inside of the glass as a result of the water vapour moving from the water's surface to the glass's surface due to this difference in partial pressures. The rate of condensation inside the glass cover is directly influenced by the pace at which water vapour evaporates from the water's surface. The still per square meter aperture's average annual performance is usually restricted to 2.5 to 3 litres per day, even in areas with higher sun intensity. Traditional solar stills are popular because of their simple construction, economical running and maintenance costs, and usefulness in isolated locations without access to power. However, the limited production of these stills serves as a catalyst for academics to investigate and develop novel techniques targeted at enhancing their efficiency [4] and [5].

In the study of a solar still in Sultanpur, India, it was observed that reducing basin water depth increases yield due to quicker attainment of steady-state and early onset of evaporation. Additionally, increased wind speed positively influences yield by accelerating condensation, with minimal impact on basin mass temperature [6]. Soliman et al. [7] experimented a solar still with an integrated heat exchanger that was coupled to a solar collector in an experiment. It was discovered that a connected solar still can produce 2.75 times as much as a solitary solar still. It is estimated that the suggested still will operate at a total efficiency of 6.45 kg/m^2 half a day. A double slope active solar still experiment was conducted by Muhammadi et al. [8]. Next, the suggested heat exchanger's performance is contrasted with that of traditional stills, including serpentine and parallel channel heat exchangers. A heat exchanger with a unique design achieved the

 DOI: 10.5545/sv-jme.2024.949

greatest efficiency of 39.4 %. Use of the NDHE results in a 34.1 % and 30.4 % increase in distillate production when compared to parallel channel and serpentine heat exchangers, respectively.

Fathy et al. [9] conducted an experiment using a parabolic trough collector and a dual slope solar still. It has been noted that a solar still equipped with parabolic trough collector (PTC) has a temperature that is higher than a standard solar still. Compared to a normal solar still, which produces roughly 28.1 % less fresh water, a solar still using PTC produces more. In an experiment, a solar still with an evacuated tube collector and thermoelectric module was used by Shafii et al. [10]. The study found that the use of forced convection improved the system's water yield and hourly efficiency, which peaked at 1.11 l/m^2 and 68 %, respectively. When the fan was removed from the system, the efficiency and water yield were reported to be 60 % and 0.97 l/m^2, respectively.

Divagar and Sundararaj [11] conducted an experiment using a solar distiller and a copper heat exchanger. A comparison was made between the energy efficiency of the modified and conventional solar stills. The modified still was found to have an energy efficiency of 28 %, while the conventional still had an energy efficiency of 17 %. A modified still's higher energy efficiency is 5.5 %, while a conventional still is 1.1 %. According to research by Nafey et al. [12], black rubber used as a storage medium within a single sloping solar still increases productivity by more than 20 % at the condition of 60 l/m^2 brine volume and 15° of a glass cover, respectively. Nafey et al. [13] investigated the effects of using a floating perforated black plate on two experiment still units, each measuring 0.25 m^2. Studies show that exposure to sunlight increases production by 15 % at 3 cm brine depth and 40 % at 6 cm brine depth.

According to research by Akash et al. [14], employing various absorbing materials, such as black rubber mats, enhanced daily water productivity by 37 %, 45 %, and 60 % when combined with black ink and black dye. El-Sebaii et al. [15] explored methods to reduce the time required for the water in the basin of a solar still featuring a baffle-hung absorber to heat up. The addition of the baffle absorber results in a 20 % increase in productivity compared to a conventional solar still without baffles. Bassam and Rababah [16] conducted research using sponge cubes of varying sizes submerged in a basin. In comparison, a similar still without sponge cubes, increased by 18 % to 273 %. Rahim [17] suggested a novel way to store additional heat energy in a horizontal solar still throughout the day in order to forward the research. By segmenting the horizontal still into discrete zones for heat storage and evaporation, this technique stores more than 42 % of the overall energy during the night-time.

As explained in Tamini [18] research, functioning under various conditions with and without a reflector and black box still significantly increased productivity. According to research by Badran [19], the output of a still might rise by up to 51 % when coupled enhancers like sprinklers and asphalt basin liners were applied to the still. Using absorbent materials like cotton & jute fabric, sponge sheet, and natural rock. Murugavel et al. [20] conducted research, in comparison with other materials, cotton fabric yields higher productivity. According to research by Tripathi and Tiwari [21], the storage effect causes a greater yield to be produced during the off-peak hours when compared to higher water depths. Many researchers have tried in vain to speed up the rate at which water evaporates and to maximize the quantity of solar radiation that strikes the still in order to improve system efficiency and use the least amount of still surface. This study introduces a novel approach by integrating phase change material (PCM) to reduce heat loss in solar desalination systems. Through extensive experimentation and comparison, the study extends the boundaries of solar desalination technology to identify the most efficient configuration.

2 EXPERIMENTAL

2.1 Setup

In this experiment, there are two solar stills installed at Vellore, Tamil Nadu, India. It is fixed to see how well this function in actual operating environments. The basin liner made up of galvanized iron sheet and the basin surface are painted with black paint to absorb maximum amount of solar radiation incident on them. It was intended the 4mm-thick glass condenser surfaces to be as heated- absorbing, as light-reflective, as solar-letting as feasible, and as resistant to heat loss as possible. For this reason, the surfaces were angled at a 10° angle. There is a wood used to frame the glass coverings and silicon rubber to seal them in order to keep everything together. Because it permitted expansion and contraction between the different materials, this seal was extremely crucial. The specifications for the glass cover included absorption of heat, low solar reflectance, maximum solar penetration, and exceptional heat retention in the basin. In order to assess how well these stills worked, it was handled carefully to document every detail of the experiment, including the temperatures and the amount of water we generated.

In the setup, condensed distillate that collects on the interior surfaces of the glass covers is collected in the setup utilizing a galvanized iron (GI) sheet collecting trough inside the solar still. This trough efficiently directs the condensate into a designated collecting flask. To accurately measure the water depth, a steel rule is securely fastened along the inside wall of the setup. Furthermore, thermocol and wood layers are used as insulation on the sides and bottom to reduce heat loss. Table 1 contains comprehensive technical details about the solar still, and Fig. 2 shows the experimental setup.

Table 1. Technical specification of the solar still

Specification	Dimension
Basin liner	0.5 m^2
Glass area	0.508 m^2
Glass thickness	4 mm
Number of glass sheets	1
Slope of glass	14º
Thermocol thickness	25 mm
Thermal conductivity of thermocol	0.015 W/(mK)
Wood thickness	12.5 mm
Thermal conductivity of wood	0.055 W/(mK)

Fig. 1 showcases various pictorial views of the absorbing materials used in the setup, highlighting their specific placements and configurations. Moreover, Fig. 3 presents a snapshot providing a visual depiction of the experimental arrangement, offering an insight into the overall setup and components in use.

The trials were carried out in May of 2022 in order to record normal conditions characteristic of that season. Three separate days were used for these trials in Vellore, India. The material used to store energy was wax, which kept in copper tubes. This PCM released heat when it wasn't in the sun and absorbed it during the day. Every experiment ran for twenty-four hours, starting at nine in the morning local time. During each experiment, a consistent water depth of 1 cm was kept. Before beginning the next experiment with a new absorbing material, the apparatus had to sit idle for at least one day in order to guarantee uniformity and establish a steady-state condition while switching between different absorbing materials.

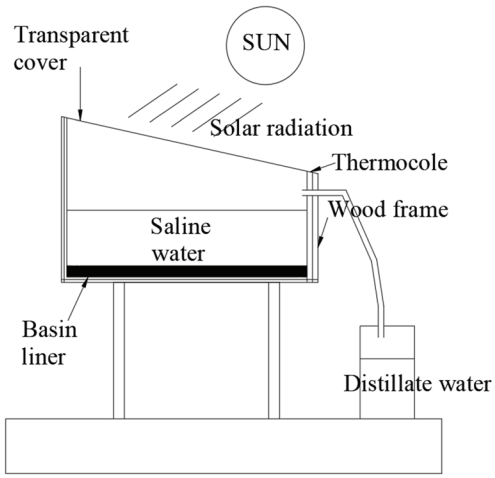

Fig. 1. Schematic diagram of experimental setup

This interval of inactivity continued from the end of the preceding trial until the current absorbing material experiment started. Keeping the water depth and inclinations constant, the following dynamic parameters were measured hourly over the course of a day: air velocity, solar radiation, distillate output, and many temperature measurements for the basin, back wall, side wall, water, glass, moist air, and ambient temperatures. K-type thermocouple combined with a digital indicator with a resolution of 0.1 °C were used to measure the water, basin, glass, and vapour temperatures. A pyranometer was utilised to measure solar radiation, and a digital anemometer was employed to monitor wind velocity. 30 mm steel rule is fixed in the inside wall of solar still to measure water depth. And the readings are shown in Tables 2 and 3.

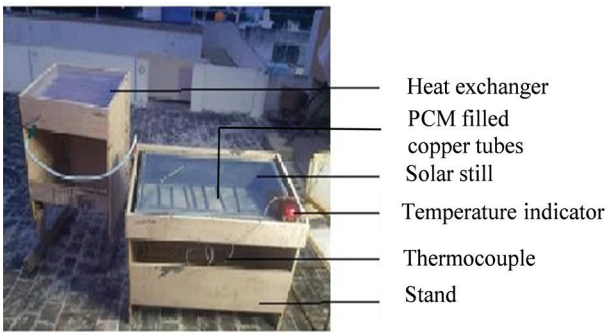

Fig. 2. Experimental setup

3 THERMAL ANALYSIS OF SOLAR STILL

The performance thermal analysis is achieved through an energy balance of the still. The energy transfer mechanisms for various components of the still, which significantly influence the output, are illustrated in Fig. 3.

To simplify the analysis, the following assumptions are considered:

- The water level in the basin remains constant throughout.
- Condensation at the glass trough occurs in a film-like manner.
- Negligible difference exists in the heat capacity among the absorbing material, insulating material, and the glass cover.
- No vapour leakage transpires within the still.
- The insulator's heat capacity, both at the bottom and sides of the still, is assumed to be negligible.

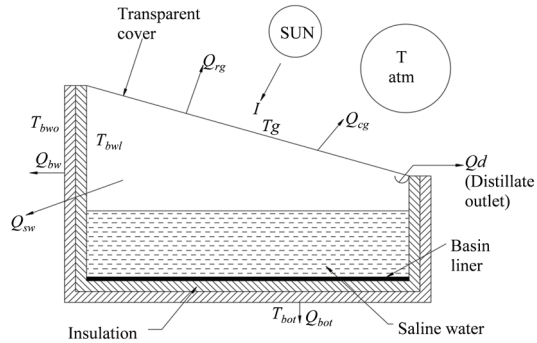

Fig. 3. Various components of conventional single slope solar still

By formulating an energy equation for a solar still and referencing Fig. 1, the still's collecting efficiency can be determined.

$$I \cdot a_g = \dot{Q}_d + \dot{Q}_{rg} + \dot{Q}_{cg} + \dot{Q}_{bw} + \dot{Q}_{sw} + \dot{Q}_{bot}, \quad (1)$$

where I is the hourly incident solar radiation, a_g is exposed glass surface area, $\dot{Q}_d$ is the heat flow rate needed for water distillation, $\dot{Q}_{rg}$ is the thermal radiation heat loss from the glass to the ambient $\dot{Q}_{cg}$ is the convective heat transfer from the glass to the ambient, $\dot{Q}_{bw}$ is the heat loss through the rear wall from inside to outside, $\dot{Q}_{sw}$ is the heat loss through the sidewall from inside to outside and $\dot{Q}_{bot}$ is the rate of heat transfer from the basin liner to the atmosphere through the bottom wall.

The Eq. (2) for $\dot{Q}_d$ is

$$\dot{Q}_d = \dot{m}_w \cdot h_{fg}, \quad (2)$$

where $\dot{m}_w$ is the mass flow rate of distilled water output, and h_{fg} enthalpy of vaporization of water (h_{fg} = 2382 kJ/kg). The convection from the glass to ambient is defined as

$$\dot{Q}_{cg} = h_{cg} \cdot a_g \cdot (T_g - T_a), \quad (3)$$

where h_{cg} is the convection coefficient amidst the glass and ambient surroundings, a_g is area of glass, T_g is temperature of glass and T_a is the temperature of ambient. Convection coefficient is primarily reliant on velocity of the wind, given by the empirical expression

$$h_{cg} = 5.7 + 3.8\ V, \quad (4)$$

where V is the wind velocity.

The thermal radiation from glass to the ambient surroundings equals to

$$\dot{Q}_{rg} = \varepsilon_g \cdot a_g \cdot \sigma \cdot (T_g^4 - T_s^4), \quad (5)$$

where ε_g is the emissive coefficient of the glass material, σ Stefan Boltzmann constant (5.67×10^{-8} W/(m^2·K^4)), a_g is exposed glass surface area, and T_s is a temperature of the sky, which is lower than the surrounding air.

$\dot{Q}_{bw}$ is heat transfer through the rear wall from inside to outside

$$\dot{Q}_{bw} = a_{bw} \cdot U \cdot (T_{bwi} - T_a), \quad (6)$$

where a_{bw} is the area of back wall, and U is overall heat transfer coefficient.

Heat transfer through the side wall from inside to outside is equal to

$$\dot{Q}_{sw} = a_{sw} \cdot U \cdot (T_{swi} - T_a), \quad (7)$$

where a_{sw} is side wall area.

$\dot{Q}_{bot}$ is the rate of heat transfer from basin liner to atmosphere through bottom wall, and expressed by conduction equation of composite wall, defined as

$$\dot{Q}_{bot} = a_b \cdot U \cdot (T_b - T_a). \quad (8)$$

Finally, the thermal efficiency η is

$$\eta = \dot{Q}_d / \Sigma \dot{Q} \cdot 100. \quad (9)$$

4 RESULTS AND DISCUSSIONS

Without using any absorbing material, readings in a range of temperatures across a range of time periods have been tabulated. Through the use of an anemometer, the wind velocity was measured. K-type thermocouples were used in conjunction with a digital temperature gauge to record the water, basin, glass, and vapour temperatures.

4.1 Comparison of Energy Distribution Percentages

The energy balance equation yields heat loss, which derived from Eqs. (2) to (8). Because the modified solar still with PCM is more productive at producing fresh water than the basic solar still with PCM, it is clear that the energy consumption for freshwater conversion ($\dot{Q}_d$) is much higher in the modified sun still. As a result, less distilled water is produced during times when there is no sunshine.

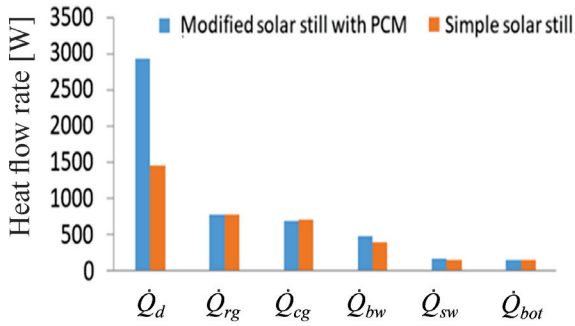

Fig. 4. Comparison of percentage of energy distribution

Furthermore, a combination of radiation and convection factors causes the main source of energy dissipation from the still to happen at the glass surface. On the other hand, due to the extensive insulation, heat losses through the side wall, back wall, and basin liner are negligible. The addition of PCM to the basin liner's bottom as an energy storage material improves its insulating performance. As a result, when considering the other aspects of energy distribution, the heat loss at the bottom wall for the modified and simple solar stills is 139.6 W and 137.8 W, respectively. When compared to the basic solar still with PCM, the improved performance of the modified solar stills with PCM shows a 49.02 % improvement. Fig. 4 shows comparison of percentage of energy distribution.

4.2 Comparison of ΔT (Temperature difference) for Modified and Simple Solar Stills Equipped with PCM

One important component affecting a solar still's production is its ΔT. A higher ΔT indicates a higher level of productivity from the solar still. Fig. 5 shows the temperature differences between the water and glass for several solar still types.

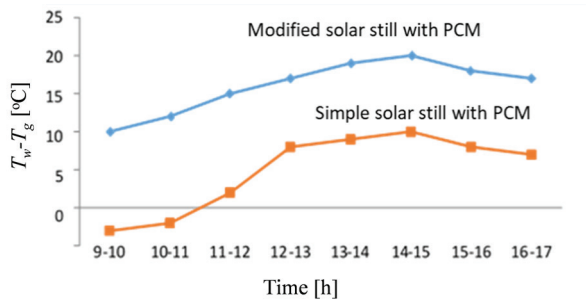

Fig. 5. Comparison of ΔT of modified and simple solar still having PCM

Table 2. Simple solar still with PCM

Sample number	Time	I [W/m²]	T_{bi} [°C]	T_{si} [°C]	T_b [°C]	T_w [°C]	T_g [°C]	T_a [°C]	Mass [l/m²]	Wind velocity [m/s]
1	09-10	490	33	32	31	27	30	24.7	0.00	0.04
2	10-11	607	35	33	33	33	35	28.3	0.09	1.1
3	11-12	715	46	45	43	50	48	31	0.25	0.07
4	12-13	895	51	50	48	60	52	33	0.33	0.06
5	13-14	845	64	64	60	75	69	36	0.45	0.05
6	14-15	790	69	67	65	80	72	33	0.5	0.07
7	15-16	680	65	65	63	77	69	29	0.3	1.2
8	16-17	510	59	58	55	70	63	27	0.25	0.03
	17-09								0.90	
Total									3.07	

Table 3. Modified solar still with PCM

Sample number	Time	I [W/m²]	T_{bi} [°C]	T_{si} [°C]	T_b [°C]	T_w [°C]	T_g [°C]	T_a [°C]	Mass [l/m²]	Wind velocity [m/s]
1	09-10	495	43	40	35	45	35	25	0.09	0.05
2	10-11	603	47	45	37	50	38	29	0.18	1.2
3	11-12	720	53	51	45	63	48	32	0.53	0.08
4	12-13	889	59	60	48	72	55	35	0.65	0.06
5	13-14	853	69	63	59	87	68	36	0.88	0.07
6	14-15	793	71	69	63	89	69	34	1.01	0.08
7	15-16	685	65	64	60	85	67	31	0.57	1.3
8	16-17	520	61	60	58	80	63	29	0.5	0.02
	17-09								1.82	
Total									6.23	

A considerably larger temperature differential between the water and the glass is seen in the modified sun still with a phase change material (PCM) and a heat exchanger than in the standard solar still with PCM. By allowing the water to be heated before it enters the still, this improvement significantly improves the performance of the modified solar still. Furthermore, it is clear that the ΔT for the basic solar still varies, rising in the afternoon and falling somewhat in the morning. Due to increased heat transfer between the water and glass, both sun stills show a very high ΔT around the 13-hour mark.

4.3 Comparison of Water Mass Productivity Among Different Solar Stills

The use of storage materials plays a key role in storing more energy in the form of sensible and latent heat. This results in a lower temperature rise of the water surface, thereby delaying the occurrence of maximum hourly yield. Significantly, a notable output is seen the next day, which increases production as heat trapped in stills with storage materials is released from 5 pm to 9 am.

The hourly productivity comparison of different solar stills is shown in Fig. 6. The addition of energy storage materials and a heat exchanger significantly increases the modified solar still's daily output. This improvement is ascribed to a greater ΔT and the distilled water absorption of usable heat ($\dot{Q}_d$). As a result, the improved solar still's performance improvement hits 49.27 %, outperforming the basic solar still with PCM.

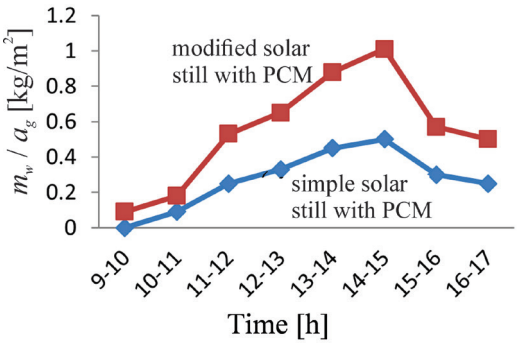

Fig. 6. Comparison of hourly productivity for various still

4.4 Comparative Efficiency Analysis of Various Solar Stills

The efficiency comparison of several types of solar stills is shown in Fig. 8. With a 56.75 % efficiency rating, the adapted solar still showed the best performance among them. When compared to the basic solar still, the upgraded solar still's average performance increase was a staggering 71.01 %. The significant enhancement can be ascribed to the elevated ΔT and the distilled water's absorption of usable heat ($\dot{Q}_d$). Fig. 7 shows Comparison of efficiency of different solar still.

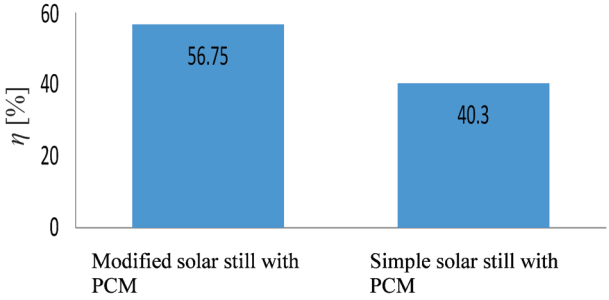

Fig. 7. Comparison of efficiency of different solar still

The combination of a heat exchanger and PCM in the solar still helps to increase the ΔT and $\dot{Q}_d$ while decreasing total heat loss, which results in increased yield. The total efficiency of the system is improved as a result of this all-encompassing approach.

5 CONCLUSIONS

The study of the solar desalination system is based on the thermal efficiency, determined by Eqs. (1) and (9). The experimental trials were carried out, covering a thorough investigation of several factors such as the temperatures of the basin water, the glass cover, the hourly yield, the back and side internal wall temperatures, and the bottom surface temperatures. The trials were conducted under the same climate to provide a comprehensive and equitable analysis for comparison reasons. Notably, in all cases, the energy consumption for the manufacture of distilled water ($\dot{Q}_d$) peaks around three o'clock. The use of PCM as a storage material successfully lowers heat loss overall. When compared to the basic solar still, the improved solar still has a greater thermal efficiency.

Throughout the trials, it was observed that heat losses through the bottom ($\dot{Q}_{bot}$) and side walls ($\dot{Q}_{sw}$) to the surrounding air remained constant, gradually increasing over time. The utilization of energy-storing materials facilitated significant heat release during periods of reduced solar intensity, thereby sustaining production levels during late afternoon and night-time. Among the designs evaluated, the solar still equipped with a heat exchanger demonstrated superior performance, attributed to its higher daily output (m_w), elevated ΔT, enhanced evaporative heat transfer coefficient, and increased absorption of usable heat by distilled water ($\dot{Q}_d$). Consequently, overall heat losses were reduced, leading to an enhanced efficiency of 56 %. In summary, the integration of a heat exchanger with the solar still emerges as the most effective approach for freshwater production, offering optimal efficiency and performance.

NOMENCLATURES

I	hourly incident solar radiation, [W/m²]
$\dot{Q}_d$	heat flow rate for water distillation, [W]
$\dot{m}_w$	mass flow rate of distilled water output, [kg/s]
h_{fg}	enthalpy of vaporization of water, [kJ/kg]
$\dot{Q}_{cg}$	convection heat transfer from the glass to ambient, [W]
h_{cg}	convection heat transfer coefficient, [W/(m^{2}K)]
a_g	exposed glass surface area, [m²]
T_g	temperature of the glass, [°C]
T_a	ambient temperature, [°C]
V	wind velocity, [m/s]
$\dot{Q}_{rg}$	thermal radiation from glass to ambient, [W]
ε_g	emissivity of the glass, [-]
σ	Stefan-Boltzmann constant, [W/(m²K⁴)]
T_s	sky temperature, [°C]
$\dot{Q}_{bw}$	heat transfer through the rear wall, [W]
a_{bw}	rear wall area, [m²]
U	overall heat transfer coefficient, [W/(m²K)]
T_{bwi}	inside temperature of the rear wall, [°C]
$\dot{Q}_{sw}$	heat transfer through the side wall, [W]
a_{sw}	side wall area, [m²]
T_{swi}	inside temperature of the side wall, [°C]
$\dot{Q}_{bot}$	heat transfer through the bottom wall, [W]
a_b	bottom wall area, [m²]
T_b	basin liner temperature, [°C]
η	thermal efficiency, [%]

7 REFERENCES

[1] Chauhan, V.K., Shukla, S.K., Tirkey, J.V., Rathore, P.K.S. A comprehensive review of direct solar desalination techniques and its advancements. *J Clean Prod* 284, 124719 (2021) **DOI:10.1016/j.jclepro.2020.124719**

[2] Mohammed, A.H., Shmroukh, A.N., Ghazaly, N.M., Kabeel, A.E. Active solar still with solar concentrating systems, Review. *J Therm Anal Calorim* 148, 8777-8792 (2023) **DOI:10.1007/s10973-023-12285-z**

[3] Ayoub, G.M., Malaeb, L. Economic feasibility of a solar still desalination system with enhanced productivity. *Desalination* 335 27-32 (2014) **DOI:10.1016/j.desal.2013.12.010**

[4] Saiful, S.A.M., Shams, S., Prasad, D.M.R., Ratnayake, U. Enhancing the performance of solar stills for desalination of the sea water. *IOP C Ser Earth Env* 646 012005 (2021) **DOI:10.1088/1755-1315/646/1/012005**

[5] Chandrashekara, M., Yadav, A. Water desalination system using solar heat: A review. *Ren Sust Energy Rev* 67 1308-1330 (2017) **DOI:10.1016/j.rser.2016.08.058**

[6] Patel, R.V., Yadav, A., Winczek, J. Experimental investigation and mathematical modelling of heat transfer coefficient in double slope solar still. *Stroj Vestn-J Mech E* 67 369-379 (2021) **DOI:10.5545/sv-jme.2021.7156**

[7] Soliman, H.M., Elgohary, H.M., Abo Elmagd, M.A., Chowdhury, S.P. Brackish water desalination using solar still with built-in heat exchanger coupled to solar collector. *2018 IEEE PES/IAS PowerAfrica* 799-802 (2018) **DOI:10.1109/PowerAfrica.2018.8521114**

[8] Mohammadi, K., Taghvaei, H., Rad, E.G. Experimental investigation of a double slope active solar still: Effect of a new heat exchanger design performance. *Appl Therm Eng* 180 4019-4033 (2020) **DOI:10.1016/j.applthermaleng.2020.115875**

[9] Fathy, M., Hassan, H., Ahmed, M.S. Experimental study on the effect of coupling parabolic trough collector with double slope solar still on its performance. *Sol Energy* 163 54-61 (2018) **DOI:10.1016/j.solener.2018.01.043**

[10] Shafii, M.B., Shahmohamadi, M., Faegh, M., Sadrhosseini, H. Examination of a novel solar still equipped with evacuated tube collectors and thermoelectric modules. *Desalination* 382 21-27 (2016) **DOI:10.1016/j.desal.2015.12.019**

[11] Dhivagar, R., Sundararaj, S. Thermodynamic and water analysis on augmentation of a solar still with copper tube heat exchanger in coarse aggregate. *J Therm Anal Calorim* 136 89-99 (2019) **DOI:10.1007/s10973-018-7746-1**

[12] Nafey, A.S., Abdelkader, M., Abdelmotalip, A., Mabrouk, A.A. Solar still productivity enhancement. *Energ Convers Manage* 42 1401-1408 (2001) **DOI:10.1016/S0196-8904(00)00107-2**

[13] Nafey, A.S., Abdelkader, M., Abdelmotalip, A. Mabrouk, A.A. Enhancement of solar still productivity using floating perforated black plate. *Energ Convers Manage* 43 937-946 (2002) **DOI:10.1016/S0196-8904(01)00079-6**

[14] Akash, B.A., Mohsen, M.S., Osta, O., Elayan, Y. Experimental evaluation of a single-basin solar still using different absorbing materials *Renew Energ* 14 307-310 (1998) **DOI:10.1016/S0960-1481(98)00082-2**

[15] El-Sebaii, A.A., Aboul-Enein, S., El-Bialy, E. Single basin solar still with baffle suspended absorber. *Energ Convers Manage* 41 661-675 (2000) **DOI:10.1016/S0196-8904(99)00141-7**

[16] Bassam, A/K A.H., Rababa'h, H.M. Experimental study of a solar still with sponge cubes in basin. *Energ Convers Manage* 44 1411-1418 (2003) **DOI:10.1016/S0196-8904(02)00162-0**

[17] Rahim, N.H.A. New method to store heat energy in horizontal solar desalination still. *Renew Energ* 28 419-433 (2003) **DOI:10.1016/S0960-1481(02)00030-7**

[18] Tamini, A. Performance of a solar still with reflectors and black dye. *Sol Wind Techn* 4 443-446 (1987) **DOI:10.1016/0741-983X(87)90019-1**

[19] Badran, O.O. Experimental study of the enhancement parameters on a single slope solar still productivity. *Desalination* 209 136-143 (2007) **DOI:10.1016/j.desal.2007.04.022**

[20] Murugavel, K.K., Chockalingam, K.K., Srithar, K. An experimental study on single basin double slope simulation solar still with thin layer of water in the basin. *Desalination* 220 687-693 (2008) **DOI:10.1016/j.desal.2007.01.063**

[21] Tripathi, R., Tiwari, G.N. Effect of water depth on internal heat and mass transfer for active solar distillation. *Desalination* 173 187-200 (2005) **DOI:10.1016/j.desal.2004.08.032**

Received 2024-02-07, revised 2024-08-30, accepted 2024-12-30, *Original Scientific Paper.*

Data Availability *The data supporting the findings of this study are available from the corresponding author upon reasonable request.*

Author Contribution *Jothilingam Manickam conducted the experiments, analyzed the data, and drafted the manuscript. Nithyanandam Chandrasekaran reviewed the manuscript and provided further corrections, Balakrishnan Nanjappan supervised the final work and approved the manuscript for submission.*

Uporaba fazno spremenljivih materialov in prenosnika toplote za izboljšano solarno razsoljevanje - Primerjalna raziskava učinkovitosti

Povzetek *V tej študiji sta preučena delovanje in primerjalna analiza več solarnih sistemov za razsoljevanje z uporabo različnih konfiguracij in materialov. Študija obravnava delovanje teh sistemov z merjenjem njihovega splošnega delovanja, temperaturnih razlik, zmogljivosti shranjevanja energije in toplotne učinkovitosti. Temeljito oceno različnih značilnosti so omogočili dosledni okoljski pogoji poskusov. Pri uporabi fazno spremenljivih materialov (PCM) kot medija za shranjevanje energije se je skupna količina toplotnih izgub znatno zmanjšala. Študije, v katerih so primerjali različne sončne peči, so pokazale očitne prednosti, zlasti pri uporabi prenosnikov toplote. Izboljšani koeficienti izhlapevanja, večje temperaturne razlike (ΔT), večja absorpcija uporabne toplote v destilirani vodi in večja dnevna proizvodnja so bili opaženi pri sončnih pečeh, opremljenih s prenosniki toplote. Glede na rezultate je imel spremenjeni solarni destilator s PCM in prenosnikom toplote najboljšo toplotno učinkovitost, ki je dosegla 56 %. Ključni cilj raziskave je bil čim bolj zmanjšati toplotne izgube in povečati donos sladke vode. Ta zasnova se je izkazala za najuspešnejšo metodo za pridobivanje sladke vode. Ta temeljita ocena in primerjalna študija več solarnih sistemov za razsoljevanje vode ponuja pomembne informacije za izboljšanje produktivnosti in učinkovitosti tehnologij za destilacijo vode na sončni pogon v različnih okoljskih okoliščinah.*

Ključne besede *solarno razsoljevanje, fazno spremenljivi materiali, primerjalna analiza povečanja učinkovitosti*

List of reviewers who reviewed manuscripts in 2024

Haslina Abdullah, Malaysia
Boris Aberšek, Slovenia
Claudio Aguilar Ramírez, Columbia
Raheem Al-Sabur, Iraq
Mustafa Altin, Turkey
R. Amrutha, India
Atthaphon Ariyarit, Thailand
Gokhan Aydin, Turkey
Khairul Azwan, Malaysia

Erkan Bahçe, Turkey
Jani Barle, Croatia
Marian Bartoszuk, Poland
Boštjan Batagelj, Slovenia
Samo Beguš, Slovenia
Mostefa Bendouba, France
Anton Bergant, Slovenia
Cristina Biris, Romania
Mirko Blagojević, Serbia
Sergii Boichenko, Ukraine
Andrej Bombač, Slovenia
sampath Boopathi, India
Jarosław Brodny, Poland
Damjan Bujak, Hungary

Caterina Capponi, Italy
Alexandru Catalin Filip, Romania
Bin Chen, Sweden
Weimin Chen, China
Bin Chen, Sweden
Gang Cheng, China
Peilin Cheng, China
Gang Cheng, China
Xiang Cheng, China
Peilin Cheng, China
Filippo Cianetti, Italy

Martin Česnik, Slovenia

Zigang Deng, China
Milena Djukanović, Monte Negro
Changbin Dong, China
Xiaozhen Du, China
Jérémie Dumas, France

Radomir Đokić, Serbia

V. Elanangai, India
Tahsin Engin, Turkey
Grzegorz Filo, Poland
Frederico Miguel Freire Rodrigues, Portugal
Hongxun Fu, China

Tamilselvan Ganesan, India
Ning-Hua Gao, China
Rok Gašperšič, Slovenia
François Gautier, France
Samira Gholizadeh, South Africa

Iztok Golobič, Slovenia
Miroslav Gombár, Slovak Republic
Damir Grguraš, Slovenia
Veronika Groma, Hungary
Alec Groysman, Israel

Meysam Haghshenas, USA
Miroslav Halilovič, Slovenia
Zhao Han, China
Boštjan Harl, Slovenia
Libor M Hlavac, Czech Republic
Richárd Horváth, Hungary
Zhili Hu, China
Wei Huang, China
Heyuan Huang, China

Soichi Ibaraki, Japan
Abbas Fadhil Ibrahim, Iraq
Špiro Ivošević, Monte Negro

Adam Jacso, Hungary
Andrej Jeromen, Slovenia
Matija Jezeršek, Slovenia

Christos Kalligeros, Greece
Deepa Kareepadath Santhosh, Slovenia
A. Karpagaraj, India
Meysam Keshavarz, UK
Jernej Klemenc, Slovenia
Pino Koc, Slovenia
Nenad M. Kolarević, Serbia
Jarosław Korpysa, Poland
Nataša Kovač, Monte Negro
Dominik Kozjek, Slovenia
Simon Krasna, Slovenia
Robert Kunc, Slovenia
Janez Kušar, Slovenia

Andrej Lebar, Slovenia
Job Angel Ledezma Pérez, Bolivia
Hirpa Lemu, Norway
Zsófia Lendek, Romania
Bo Li, China
Mingxiang Ling, China
P. F. Liu, China
Chao Liu, China
Yingwen Liu, China
Chao Liu, China
Zhan Liu, China
Shiguang Liu, China
Xu Lixin, China
Gorazd Lojen, Slovenia
Edgar López, Mexico

Pradeepkumar Madhesan, India
Marin Marin, Romania
Ab Rahman Marlinda, Malaysia

Vincent Maurel, France
Giovanni Meneghetti, Italy
Longhui Meng, China
Rafael Mihalič, Slovenia
Ava Mohammed, Iraq
Nikolaj Mole, Slovenia
Mohammad Naeim Moradi, Iran
Swarnajay Mukherjee, USA
Matthieu Museau, France
Teguh Muttaqie, Indonesia

Syamak Hossein Nedjad, Iran
Trung-Thanh Nguyen, Vietnam

Murčo Obučina, BIH
Domen Ocepek, Slovenia
Ivan Okorn, Slovenia
Simon Oman, Slovenia
S. Omprakasam, India
Alen Oseli, Slovenia
Eneja Osterman, Slovenia
Sabri Ozturk, Turkey

Srinivasa P. Pai, India
Massimiliano Palmieri, Italy
M. Pannone, Italy
Jorge Parrondo, Spain
Martin Petkovšek, Slovenia
Andrea Petroselli, Italy
Truong Phung, Australia
Damian Pietrusiak, Poland
Bojan Podgornik, Slovenia
Marko Polajnar, Slovenia
Milton Luiz Polli, Brasil
Vladimir Popovic, Serbia
Primož Potočnik, Slovenia
Radu-Emil Precup, Romania
Erhan Pulat, Turkey
Franci Pušavec, Slovenia

S. Rajkumar, Canada
Jose Billerman Robles-Ocampo, Mexico
Dragan Rodic, Serbia
Manuel Javier Rosel Solis, Mexico

Aleksandr Sakhnevych, Italy
Rafael Sanchez Crespo , UK
Mehmet Sari, Turkey
Adriana Savin, Romania
Dieter Schuöcker, Austria
Dhaval B. Shah, India
Ambuj Sharma, India
Chi-bing Shen, China
S. Siddharth, India
Vilmos Simon, Hungary
P. Sivasankaran, India
Lidija Slemenik Perše, Slovenia

Emil Smyk, Poland
Tushar Sonar, India
Marco Sortino, Italy
Janani Srree Murallidharan, India
Luka Sterle, Slovenia
Florian Stöckl, Germany
Grzegorz Struzikiewicz, Poland
Szabolcs Szavaj, Hungary
Dariusz Szpica, Poland

Božidar Šarler, Slovenia
Domen Šeruga, Slovenia
Gašper Škulj, Slovenia

Slobodan Tabaković, Serbia
Hasan Tabanli, Turkey
Yavuz Selim Taspinar, Turkey
S. Thillikkani, India
Arris S. Tijsseling, The Nederlands
Roman Trochimczuk, Poland
Enrico Troiani, Italy

Miran Ulbin, Slovenia
Mesut Uyaner, Turkey
Cuneyt Uysal, Turkey
Erdem Uzunsoy, Turkey

Farhad Vahidinia, Iran
Joško Valentinčič, Slovenia
Wim Van Helden, Austria
V. Volgin, Russia
Arkady Voloshin, USA
Rok Vrabič, Slovenia
Damir Vrančić, Slovenia
Nikola Vukašinović, Slovenia

Xuesheng Wang, China
Shunli Wang, China
Xuesheng Wang, China

Wanghui Xu, China

Judy P. Yang, Taiwan
Shuai Yang, China
Shengqiang Yang, China
Yuze Ye, China

Andriy Zahorulko, Ukraine
Habib Hamed Zargari, Iran
Yi Zhang, Belgium
Yanhu Zhang, China
Xue-Lian Zheng, China
Tiegang Zheng, China
Changtai Zhou, China
Ma Ziyong, China
Samo Zupan, Slovenia

Sebastjan Žagar, Slovenia
Uroš Župerl, Slovenia
Urban Žvar Baškovič, Slovenia

The Editorial would like to thank all the reviewers in participating in reviewing process.
We appreciate the time and effort and greatly value the assistance as a manuscript reviewer for Strojniški vestnik – Journal of Mechanical Engineering.

ICAMPP 2025

International conference on **Additive Manufacturing and Post-Processing**

7. - 9. 9. 2025 - Portorož, Slovenia

This conference will deliver discussions about the **challenges**, **opportunities**, and **state-of-the-art** on **additive manufacturing technologies** and **post-processing.**

Academic and industry participants invited to join!

Supported by the Horizon EU project

SEAMAC
STRENGTHENING THE EXCELLENCE OF ADDITIVE MANUFACTURING CAPABILITIES

Funded by the European Union

- Plenary lectures
- Distinguished invited lectures
- Technical sessions
- Panel discussions
- Networking sessions

NO REGISTARTION FEE!
Number of participants limited to 100!

JOIN NOW

www.icampp.si

ICAMPP 2025

TU BERGAKADEMIE FREIBERG · TUBAF Die Ressourcenuniversität. Seit 1765.

UNIVERSITY OF LJUBLJANA | FS Faculty of Mechanical Engineering

TECHNION Israel Institute of Technology

Contents

9 770039 248001
ISSN 0039-2480

https://www.sv-jme.eu/